Microscopic and Macroscopic Properties of AOT/Iso-octane/Water Sheared Lyotropic Lamellar Phases

Yann Auffret

Ecole Doctorale de Mécanique Energétique
Université Joseph Fourier de Grenoble, France
Department of Chemical and Biomolecular Engineering
The University of Melbourne, Australia

Microscopic and Macroscopic Properties of AOT/Iso-octane/Water Sheared Lyotropic Lamellar Phases

Yann AUFFRET

Submitted in total fulfillment of the requirements of the degree of Doctor of Philosophy under a Cotutelle arrangement with

The University of Melbourne

and

The University Joseph Fourier

Defended the 16^{th} of December 2008
In front of the Board of Examiners constituted by:

Mr. C. ROCHAS	**Chairman**
Mr. J-P. DECRUPPE	
Mr. G.G. WARR	**Reviewers**
Ms. V. TIRTAATMADJA	
Ms. N. EL KISSI	
Mr. D.E. DUNSTAN	
Mr. D.C. ROUX	**Examiners**

Abstract

Surfactant molecules such as AOT have amphiphilic properties which result in the formation of molecular aggregates when mixed with polar and apolar solvent such as water and iso-octane respectively. These aggregates can adopt various structures depending on the relative concentrations of the constituents in the ternary mixture. For AOT/Iso-octane/Water molecular systems, X-ray scattering experiments show that the favored structures at rest range from simple isotropic reversed micelles at high iso-octane concentration to complex hexagonal and lamellar anisotropic lyotropic liquid crystal phases when the iso-octane content is decreased. Depending on the water content, the latter lamellar phase exhibits various degrees of topological defects. In the following piece of research we investigate the rheological properties of such microscopically heterogeneous materials.

When sheared, these materials show an extremely rich rheological behavior depending on the defects density. Indeed, whereas the defect free lamellar samples show newtonian flow properties, the emergence of topological defects leads to increasingly time and shear history dependent viscoelastic properties.

A preliminary study of the rheological properties of the considered material using transient strain and stress controlled rheometry shows a complex and unusually long transient regime. Given that the level of strain experienced by the material is high enough, both used techniques show that a steady state is finally reached after a rheopectic transition (*ie.* an increase of the viscosity upon application of either a constant shear rate or shear stress).

The structural properties of the material are then investigated at the microscopic and nanoscopic scales by means of flow-birefringence patterns analysis, wide angle x-ray scattering and freeze fracture electron microscopy. The results of the latter two experimental techniques show a transition at the nanoscopic scale from interconnected lamellar structures at rest to lamellar vesicles once the steady state is reached. This transition at the nanoscopic scale is shown to come along with a rearrangement of the topological defects at the microscopic scale by means of flow-birefringence patterns analysis. Moreover, both of these transitions occur after a given critical strain corresponding to the end of the rheopectic transition observed at the macroscopic level.

At last, the viscoelastic properties of the shear-induced phase are investigated after a creep flow based procedure allowing to control the shear-history of the material. These measurements indicate that the material behaves as soft jammed systems with controlled yielding and aging properties.

Résumé

Les molécules tensioactives telles que celles d'AOT ont des propriétés amphiphiles qui conduisent à la formation d'aggrégats moléculaires lorsqu'elles sont mélangées à des solvants polaires et apolaires comme l'eau et l'iso-octane. La taille et la forme des aggrégats formés dependent des concentrations relatives de chacun des constituants du mélange ternaire. Pour le système AOT/eau/iso-octane considéré dans cette étude, des expériences de diffusion de rayon X ont ainsi montré que la formation de micelles inverses est favorisée dans les mélanges riches en iso-octane tandis que les phases mésomorphes cristallines de type hexagonale ou lamellaire sont favorisées lorsque la quantité d'iso-octane du mélange diminue. En fonction de la quantité d'eau du mélange, ces dernières présentent différentes concentrations de défauts topologiques. Dans les travaux présentés dans ce manuscrit nous étudions les propriétés d'écoulement de ces matériaux hétérogènes à l'échelle micro-, et macroscopiques.

Lorsqu'ils sont cisaillés, les cristaux liquides lyotropes présentent des propriétés d'écoulement variées allant du comportement newtonien à des comportements viscoélastiques non-linéaires dépendant du temps et de 'l'histoire' de l'échantillon considéré.

Nos travaux liminaires en rhéométrie transitoire controllée soit en vitesse soit en contrainte montrent un régime d'écoulement transitoire complexe et inhabituellement long dépendant de la déformation subit par l'échantillon. Dans les deux cas un régime d'écoulement permanent est atteint après une transition rhéopectique (ie. une augmentation de la viscosité à cisaillement constant).

Les propriétés structurelles du matériaux sont etudiées au moyen de techniques de visualisation de textures biréfringentes, de diffusion des rayons X aux grands angles et de microscopie électronique en transmission. Les deux dernières techniques montrent à l'echelle nanoscopique une transformation sous cisaillement des structures initiallement lamellaires planes en vésicules lamellaires de type 'oignons'. Cette transition à l'échelle nanoscopique s'accompagne d'une réorganisation des défauts topologiques à l'echelle microscopique mise en évidence lors de l'observation des textures biréfringentes. Nous montrons que ces transitions aux échelles nanoscopiques et microscopiques sont à l'origine de la transition rhéopectique observée en rhéométrie.

Enfin, les propriétés viscoélastiques, de seuil d'écoulement et de viellissement de la phase vésiculaire induite sous cisaillement sont déterminées à l'aide d'une procédure expérimentale permettant de controler l'histoire de l'échantillon.

Declaration

This is to certify that:

(i) the thesis comprises only my original work towards the PhD except where indicated,

(ii) due acknowledgement has been made in the text to all other material used,

(iii) the thesis is less than 100,000 words in length, exclusive of table, maps, bibliographies, appendices and footnotes.

Yann AUFFRET

Publications

During the course of this project, a number of public presentations have been made which are based on the work presented in this thesis. They are listed here for reference.

- Y. Auffret, D.C. Roux, N. El Kissi, F. Caton, D.E. Roux, I. Pignot-Paintrand, Y. Nishiyama and C. Rochas.
  Ecoulement et non écoulement d'une phase lamellaire chargée et multi-connectée.
  42^{eme} *colloque du Groupe Français de Rhéologie* (Palaiseau 2008), oral presentation.

- Y. Auffret, D.C. Roux, D.E. Dunstan, N. El Kissi and F. Caton.
  Yielding and aging in sheared lyotropic phases of interconnected bilayers.
  The XVth International Congress on Rheology, AIP Proceedings,(2008), 1036-1039.

- Y. Auffret, D.C. Roux, D.E. Dunstan, N. El Kissi and F. Caton.
  Yielding and aging in sheared lyotropic phases of interconnected bilayers.
  XVth International Congress on Rheology, (Monterey 2008), oral presentation.

- Y. Auffret, D.C. Roux, N. El Kissi, F. Caton, I. Pignot-Paintrand and D.E. Dunstan.
  Aging and Yielding in Dense AOT/Iso-octane/Water Emulsions.
  Accepted for publication in European Physical Journal E (2009)

- Y. Auffret, D.C. Roux, N. El Kissi, D.E Dunstan and I. Pignot-Paintrand.
  Stress and strain controlled rheometry on a concentrated lyotropic lamellar phase of AOT/water/Iso-octane.
  Published online (December 2008

- Y. Auffret, D.C. Roux, N. El Kissi and D.E. Dunstan.
  Shear Induced Structures in an Ordered Phase of the ternary surfactant System AOT/Iso-octane/Water.
  European Colloids and Interface Science Conference (Geneva 2007), poster session.

Acknowledgments

As this work has been carried out in two laboratories in France and in Australia, I have many people to thank in both places. I already apologize to anyone I may forget in this page.

First, I would like to thank Prof. Gregory.G. Warr from the University of Sydney in Australia and Prof. Jean-Paul Decruppe from the 'Université Paul Verlaine à Metz' in France for their thorough reviews of this manuscript. I believe their comments have strongly enhanced the quality of this piece of work.

I would also like to thank Mr. Cyrille Rochas and Ms. Viyada Tirtaatmadja for having kindly accepted to take part to the board of examiners. I especially thank Mr. Cyrille Rochas for the beam time on the D2AM beamline at the European Synchrotron Radiation Facility and his kind and efficient support for the SAXS experiments.

Of course, I express my full gratitude to my Advisors, Nadia El Kissi, David Dunstan and Denis Roux. Their constant supports and excellent pieces of advice for the past three years have made this work not only interesting and exciting but pleasant as well. I especially thank Denis Roux who has initiated the collaboration between the 'Laboratoire de Rhéologie' in France and the Particulate Fluids Processing Centre in Australia. Working in David Dunstan's research group in Melbourne for one year and half has been one of the most thrilling experiences I had. I therefore thank them for the great opportunity they offered me.

I also thank the different people I have worked with. Especially, Isabelle Paintrand from the 'CERMAV' in Grenoble and Annie Rivoire from the 'CTμ' in Lyon for the Freeze Fracture Transmission Electron Microscopy. I thank François Caton and hélène Galliard from the 'Laboratoire de Rhéologie' for fruitful discussions on the complex rheological properties of my samples. Of course, none of these findings would have been possible without the laboratory technicians and the administrative staff of both laboratories.

I would finally like to thank my family, Cheevanuch and my friends for their support and the good times spent together. A special thanks to Adriel and Andrew my housemates in Australia for their knowledge of Melbourne's nightlife and to Herve and Julie, my housemates in France, for their support while writing this manuscript. I do believe that they have contributed to the quality of this work by giving me numerous opportunities to explain what weres my findings in a friendly environment.

Contents

List of Figures

General Introduction

Lyotropic molecular systems are complex fluids within which surfactant molecules self-assemble into complex molecular aggregates. In ternary lyotropic systems, the hydrophilic part or polar head of the surfactant molecules are oriented toward a polar solvent, while their hydrophobic part or apolar tails are swollen in an apolar solvent. Their spontaneous assembling results from a competition between steric and hydrophobic interactions as well as in the case of ionic surfactants coulomb interactions. As a consequence, the favored structures in quiescent lyotropic systems are those minimizing the free energy of its constituents molecules. Accordingly, lyotropic sytems show a wide variety of mesophases with various local structures (hexagonal, lamellar, sponge, cubic, micellar...) depending on the nature of the surfactant molecules, the chosen polar or apolar solvents and their relative concentrations in the mixture.

Because of their potential applications in various fields such as oil recovery, personal care products, detergents or paints, lyotropic systems have been extensively studied in the last decades. Depending on the favored structures and the volume fraction they occupied in the mixtures, lyotropic systems can exhibit various degree of spontaneous ordering on length scales ranging from the *Ångström* (molecular scale) to the *millimeter* (rheology, birefringent textures,...). These multi-scale orderings confer them complex rheological properties resulting from possible shear induced structural transition.

In this piece of research we investigate the shear induced formation of isotropic lamellar vesicles in initially anisotropic lamellar phases of interconnected and charged bilayers. The lyotropic systems considered here are ternary mixtures

of AOT (sodium bis[2-ethylhexil]sulfosuccinate), iso-octane (2-2-4 trimethylpentane) and water. The lamellar phases formed in these systems extend on a relatively wide concentration range given that the Iso-octane to AOT concentration ratio remains sufficiently low and that sufficient amount of water are considered. Depending on the water content of the mixture the lamellar phase evolve from almost stacked bilayers free of any permanent topological defect to lamellar phases with permanent disclinations and dislocations at the mesoscopic scale.

The understanding of the phenomena leading to such shear-induced structural transitions requires time resolved experiments allowing to characterize the material properties at all involved length scales, nanoscopic, microscopic and macroscopic. This is done after different experimental techniques, namely wide angle x-ray scattering under shear, freeze fracture electron microscopy, flow birefringence texture analysis and shear rheometry. Besides the shear-induced mesophase present complex viscoelastic properties. These are characterized after an especially designed creep-flow based measurement procedure which allows a full control of the different parameters involved.

This manuscript is divided into two parts untitled '*Theoretical Background and Experimental Setup*' and '*Results and Discussions*'. These are organized in chapters as follows.

In the first chapter, we first give an overview of the intermolecular forces involved in the self-assembling process of surfactant molecules. Then we introduce basic model accounting for the wide variety of structures encountered in lyotropic systems. At last the AOT/Iso-octane/water phase diagram is described with a focus on the lamellar mesophases subsequently investigated.

The second chapter first introduces basic notions in rheology. In a second section usual non-newtonian effect encountered in lyotropic systems are introduced and discussed, notably the notion of yield stress and thixotropy. In the

last section of the chapter we will focus on a complete description of the experimental devices used in shear rheometry together with the experimental procedure followed, namely transient strain and stress controlled rheometry and inertial coupling in creep flow.

In the third and last chapter of the first part, we briefly introduce the theoretical backgrounds on light propagation in birefringent materials and x-ray scattering prior to describe the experimental setups used to probe the investigated material at the microscopic and nanoscopic scales. These description is completed by the experimental protocol followed to prepare the freeze fracture replica observed in transmission electron microscopy.

The second part of the manuscript starts with a short chapter introducing some relevant results of the literature on shear induced structural transition in lamellar lyotropic mesophases.

In the fifth chapter we will introduce and discuss the results of a preliminary studies on the transient rheological behaviour of the studied ternary mixtures. we will focus on the different parameter one has to control to define reliable measurements procedure at the macroscopic scale. Notably an effect of the sample confinement on its apparent rheological properties will be shown and discussed.

The sixth chapter will focus on the characterization of the material structures at nanoscopic and microscopic scales. The result of our flow birefringence texture observations and wide angle x-ray scattering experiments will be presented and discussed. The correlation between the sample structural evolution and its transient rheological behaviour will be explicitly shown in this chapter.

At last, the aging and yielding properties of the shear-induced mesophase will be investigate in the seventh and last chapter of the manuscript. The different parameters controlling these properties will be identified and their effects discussed on the basis of creep-flow based measurements and freeze fracture electron microscopy.

Introduction Générale

Les systèmes moléculaires lyotropes sont des fluides complexes au sein desquels des molecules tensioactives s'auto-associent pour former des aggrégats moléculaires complexes. Dans les systèmes lyotropes ternaires la partie hydrophile ou tête polaire des molécules tensioactives pointe vers un solvent polaire tandis que leurs parties hydrophobes ou queues apolaires baignent dans un solvent apolaire. La formation spontanée d'aggrégats moléculaires resulte d'une compétition entre les interactions stériques et hydrophobes et également, dans le cas des tensioactifs ioniques, les interactions de Coulomb. Ainsi, les structures favorisées au repos dans les systèmes lyotropes sont celles pour lesquelles l'énergie libre des molécules constituant le système est minimisée. En conséquence, les systèmes lyotropes présentent une grande variété de structures locales (hexagonale, lamellaire, éponge, cubique, micellaire,...) dépendant de la nature du tensioactif, des solvents polaires et apolaires utilisés et de leurs concentrations relatives dans le mélange.

Du fait de leurs nombreuses applications potentielles dans différents domaines de l'industrie, récupération de pétrole, produits d'hygiène personnelle, détergeants, peintures, etc..., les systèmes lyotropes ont fait l'objet de nombreuses études durant les dernières décennies. En fonction de la nature des aggrégats formés par les molécules de tensioactif et du volume qu'ils occupent dans les mélanges, les systèmes lyotropes peuvent présenter différent degrés d'organisation spontanée à des échelles de longueurs allant de l'Angström (echelle moléculaire) au millimètre (rhéologie, textures,...). Ces organisations structurelles multi-échelles s'accompagnent bien souvent de propriétés d'écoulement complexes résultant de possibles transitions de structures sous cisaillement.

Dans ce travail de recherche nous nous intéressons à la formation induites sous cisaillment de vesicules lamellaires isotropes dans les phases initiallement lamellaires anisotropes de bicouches chargées et interconnectées. Les systèmes

lyotropes considérés dans cette étude sont des mélanges ternaires d'AOT (sodium bis[2 ethylhexil]sulfosuccinate), d'Iso-octane (2-2-4 trimethylpentane) et d'Eau. Les phases lamellaires formées par ces systèmes s'étendent sur une plage de concentrations relativement larges correspondant aux faibles valeurs du rapport de concentrations en Iso-octane et AOT, et aux teneurs en eau suffisantes. En fonction de la quantité d'eau présente dans le mélange les phases lamellaires considérées ici évoluent de bicouches parfaitement alignées et exemptes de tout défauts topologiques à des bicouches interconnectés présentant des défauts topologiques permanents à l'échelle mésoscopique.

La compréhension du phénomène conduisant à de telles transitions structurelles induites sous cisaillement nécessite des expériences résolues en temps permettant de sonder les propriétés du matériaux à toutes les échelles mises en jeu: nanoscopique, microscopique et macroscopique. Pour ce faire nous avons utilisé les différentes techniques expérimentales suivantes: Diffusion de Rayon X aux Grand Angles sous cisaillement, Microscopie Electronique en Transmission de cryofractures, analyse de textures de birefringence sous écoulement et rhéométrie de cisaillement. De plus les phases induites sous cisaillement considérées dans cette étude présentent des propriétés viscoélastiques complexes. Celle-ci sont caractérisées à l'aide d'une procédure basée sur des mesures de fluages successives permettant une maîtrise complète des différents paramètres influant sur leur comportement.

Part I

Theoretical Background and Experimental Setup

Chapter 1

Self-Assembling Molecular Systems

Contents

Résumé du Chapitre 1

Dans ce premier chapitre nous introduisons les notions de bases nécessaires à la compréhension des phénomèmenes d'auto-association des molécules tensioactives.

Nous présentons dans un premier temps les différents types d'interactions intermoléculaires mises en jeu dans ces phénomènes: les interactions de Coulomb, de Van Der Waals et hydrophobes.

Les phénomènes d'auto-association des molécules tensioactives dîtes amphiphiles, ie. à la fois hydrophile et hydrophobe, sont alors abordées du point vue thermodynamique puis géométrique. Ceci permet d'introduire les différents paramètres controllant la taille et la forme des aggrégats moléculaires formés.

La troisème partie du chapitre est consacré à la présentation du système ternaire lyotrope AOT/Iso-octane/Eau qui a été considéré dans cette étude. Après avoir introduit le diagramme de phase ternaire, nous nous concentrons sur une description des phases de cristaux liquides lyotropes rencontrées dans cette étude, notamment des phase lamellaires.

1.1 Introduction

In condensed phases as complex fluids, the arrangement of atoms, molecules or groups of molecules, either it is ordered or disordered is governed by intermolecular forces. The various origins of intermolecular forces make them difficult to classify, however as Israelachvili [1], one can roughly distinguish between three categories;

(i) Forces which arise from quantum effects and result in covalent bonding of atoms in molecules as well as in excluded volumes interactions. These forces are those governing most chemical reactions.

(ii) Forces which are purely electrostatic in nature and arise from the Coulomb forces between charges. These are the force governing the solvation of ionic particles.

(iii) Polarization forces which involve interaction between dipole moments either they are permanent or induced by the movement of nearby charges.These forces are those holding molecules together in most liquids.

The effects of each of these forces compete or combine in condensed material and lead to astonishingly various arrangements of the atoms and the molecules compounding them. These various arrangements confer them with not less various macroscopic properties.

It would be illusory to pretend to a complete presentation of the 'intermolecular forces matter' in this PhD thesis. However as the self-assembling properties of the molecular system investigated in this project are directly ensuing from these forces it is also not conceivable not to begin this manuscript with at least a rough presentation of the intermolecular forces involved. This short presentation is followed by a presentation of amphiphilic molecules and their aggregation properties in different solvents. A third section will present the various structures encountered in self-assembling molecular systems while the last section of this chapter consists in the presentation of the phase properties of the AOT/Iso-octane/Water

system investigated in this project.

1.2 Intermolecular Forces

As mentioned above, the following section is restricted to a succinct presentation of the intermolecular forces involved in self-assembling molecular systems. Those looking for a more complete and thorough presentation of intermolecular interactions are referred to the book of J.N. Israelachvili [1]. Intermolecular interactions are commonly described using a potential function $W(r)$ related to the force F between two molecules separated by a distance r by equation 1.1

$$F = -\frac{dW}{dr} \tag{1.1}$$

In this manuscript, molecules compounded of covalently bonded atoms will be regarded as indivisible entities. As a consequence, the first category of forces mentioned above which control the formation of covalent bonding and the places occupied by the atoms in a molecule and therefore its chemical and physical properties will not be treated here. Instead we will consider the long range intermolecular forces which control all phenomena occurring in materials in which no chemical reaction are involved. In other terms, we will focus this presentation on the physical phenomena giving rise to physical binding of molecules, by far the most important in self-assembling molecular systems while the forces involved in the formation of chemical binding will be left out.

1.2.1 Coulomb Interactions

Coulomb forces are those exerted between charged atoms or ions on each others. Let us consider two isolated charges Q_1 and Q_2 at a distance r of each other in a medium characterized by a dielectric constant ϵ. The potential function or free energy $W(r)$ associated with the Coulomb interaction between these two charges is given by the relation 1.2. In the right term of the latter, Q_1 and Q_2

are expressed in terms of the elementary charges ($e = 1.602.10^{-19}C$) multiplied by their ionic valencies z which correspond to the number of elementary charges of a given ions multiply by its sign.

$$W(r) = \frac{Q_1 Q_2}{4\pi\epsilon_0\epsilon r} = \frac{z_1 z_2 e^2}{4\pi\epsilon_0\epsilon r} \tag{1.2}$$

Following equation 1.1, it comes that the force F given by relation 1.3 exerted by charges on each other decays as the inverse-square distance separating them making it very long ranged.

$$F = -\frac{dW(r)}{dr} = \frac{Q_1 Q_2}{4\pi\epsilon_0\epsilon r^2} \tag{1.3}$$

Anticipating on the following section, we define here the electric field E expressed in $V.m^{-1}$ induced by a charge Q_1 at a distance r as:

$$E_1 = \frac{Q_1}{4\pi\epsilon_0\epsilon r^2} \tag{1.4}$$

so that the force F exerted by Q_1 on a charge Q_2 at distance r is given by relation 1.5.

$$F = Q_2 E_1 \tag{1.5}$$

The very long range of Coulomb interactions is in apparent contradiction with the fact that the volume of an ionic medium does not affect its properties. However, since a positive ion always comes along with a negative counterpart in a medium whether it is a solution or an ionic crystal, the electric field induced by the presence of its charge is screened so that it only affects nearby atoms and molecules and the apparent contradiction mentioned above is raised.

Considering the expression 1.2 of the Coulomb interactions, one can roughly understand why ionic crystals are more soluble in solvent with high dielectric constant than in solvent with low dielectric constant. Indeed, the Coulomb inter-

action between charges in a medium is inversely proportional to its dielectric constant. As a consequence, the Coulomb interaction holding two opposite charges together is weaker in solvent with high dielectric constant such as water ($\epsilon = 78$) with the result that their dissociation is all the more eased.

Coulomb interactions between two charged entities are the most energetic forces involved in a ionic solution. However, the presence of counterions usually reduces their effects so that the effect of other intermolecular forces become predominant. Such intermolecular forces and their effects are described in the following sections.

1.2.2 Van Der Waals Interactions

Whereas Coulomb interactions dominate in ionic solution, in most liquids, Van der Waals forces are the ones which hold non-ionic molecules together. These latter arise from the polar properties of molecules whether these are permanent as in water molecules or fluctuating as in alkanes molecules. Although they carry no net charge, polar molecules possess an electric dipole which arises from the ability of some atoms to attract electrons of neighboring atoms as illustrated for a water molecule in Fig.1.1. This results in the formation of a dipole moment $\mathbf{u} \equiv \mathbf{r}q$ in which $\mathbf{r}$ is the distance vector between the induced charges $+q$ and $-q$. Dipole moment are measured in units of Debye D ($1D = 3.336.10^{-30} C.m$).

As an ion creates an electric field, a dipole moment creates an electric field which can affect neighboring molecules whether they are polar molecules or not. Interactions between two permanent dipoles $\mathbf{u}_1$ and $\mathbf{u}_2$ tend either to pull them apart or closer depending on their relative orientation given by $\mathbf{u}_1 \cdot \mathbf{u}_2$. In a liquid where polar molecules can rotate freely, dipoles constantly reorient themselves with respect to their neighbors so that the attractive dipolar interactions are maximized while the repulsive ones are minimized. The resulting net attractive forces are referred to as Keesom or orientation forces. Since the electric field cre-

ated by a permanent dipole only affect its closest neighbors, no overall permanent molecular orientation emerges and the liquid remains isotropic.

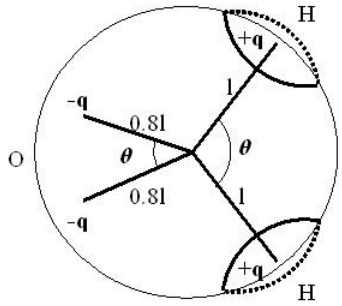

Figure 1.1: ST2 model of the tetrahedral charge distribution in water molecule; q=0.24e, l=0.1nm, θ = 109. The electrons of the two hydrogen atoms are attracted toward the oxygen atom resulting in the emergence of a polar moment. Reproduced from [1]

Although they do not have permanent dipoles, apolar molecules have fluctuating ones resulting from the motion of their electronic clouds. Since dipoles interact with each other through their electric field, a correlation exists between their fluctuating orientations and magnitudes which give rise to attractive forces known as London forces. The latter being at the origin of the dispersion of light by a medium, they are also often referred to as dispersion forces. Any given electric field $\mathbf{E}$ either it is created by a permanent dipole, a fluctuating dipole or even a light wave interacts with the electronic cloud of a molecule to create an induced dipole moment $\mathbf{u}_{ind} = \alpha_0\mathbf{E}$ in which α_0 is the polarizability of the molecule expressed in $C^2.m^2.J^{-1}$. Whereas Dispersion forces referred to the forces induced by fluctuating electric fields and are present in all liquids, the last remaining interactions to take into account while treating Van Der Waals Forces are those involving permanent dipole and fluctuating ones known as induction or Debye interactions. Indeed, in the same way a fluctuating electric field induces a dipole moment in a molecule, a permanent dipole also induce a dipole moment in a apolar molecules.

The interaction potential of Van Der Waals interaction between two molecules separated by a distance r is then given by relation 1.6. In the latter, the first, second and third terms correspond to the Debye, the Keesom and the London interaction energy respectively. h is the Planck's constant ($6.626.10^{-34} J.s$), k_B the Boltzmann's constant ($1.38.10^{-23} J.K^{-1}$), ϵ_0 the permittivity of free space ($8.854.10^{-12} C^2.J^{-1}.m^{-1}$) and ν_i the electronic ionization frequency (s^{-1}) of the molecule i.

$$W(r) = -\frac{1}{(4\pi\epsilon_0)^2 r^6}\left[\left(u_1^2\alpha_{02} + u_2^2\alpha_{01}\right) + \frac{u_1^2 u_2^2}{3k_B T} + \frac{3\alpha_{01}\alpha_{02}h\nu_1\nu_2}{2\left(\nu_1 + \nu_2\right)}\right] \tag{1.6}$$

In most liquids, London interactions are stronger than the two others. However a noticeable exception is water for which Keesom interactions dominates. These unusual properties of water molecule are one amongst others which will be discussed in the following section.

Although it gives a good approximation of the phenomena involved in non ionic liquid, the Van Der Waals interaction potential given by relation 1.6 lacks the consideration of multiple absorption frequency of atoms and molecules and does not suit anymore when interactions of molecules in a solvent are considered. A more complete theory of Van der Waals forces taking the previous shortcomings into account have been successfully developed by McLachlan. However, since the purpose of this section is to introduce some basic concept concerning intermolecular forces, I will not develop further and refer to the book of J.N. Israelachvili [1] instead.

1.2.3 Hydrogen Bonding and Hydrophobic Interactions

The last types of interactions to consider to complete the presentation of the intermolecular interactions involved in self-assembling molecular systems are closely related. These are hydrogen bonding and hydrophobic interactions.

Although not as energetic as covalent bonds ($\approx 500 kJ.mol^{-1}$), with bonding

energies of roughly $30kJ.mol^{-1}$ hydrogen bonds are still stronger than Van Der Waals interaction ($\approx 1kJ.mol{-}1$). As indicated by their name, hydrogen bonding involves hydrogen atoms and electronegative ones as Oxygen, Nitrogen, Chlorine and Fluorine atoms. The small size of hydrogen atoms and their tendency to be easily positively charged when covalently binded to an electronegative atom as depicted in Fig.1.1 for a water molecule result in the emergence of strong interactions with other neighboring electronegatives atoms. Because they can occur between atoms of different molecules as between atoms of a same molecules, hydrogen bonding are an important factor in the set-up of macromolecular structures.

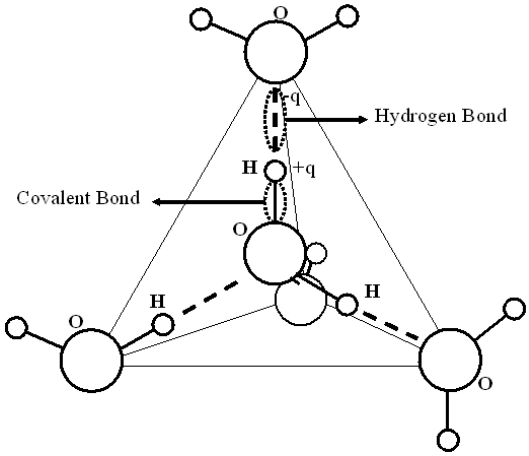

Figure 1.2: 3D Structures of ice; Each oxygen atom are involved in four linear hydrogen bonds with four water molecules forming a tetrahedral structure. reproduced from [1]

Since a water molecule can be involved in the formation of four hydrogen bonds, the latter have a prominent role and account for many of the unusual properties of water. The favored conformation of water molecules in the solid state is depicted in Fig.1.2. This tetrahedral structures tends to remain in liquid water for which molecules constantly reorient themselves in respect to their neighbors so that the tetrahedral structure of Fig.1.2 is favored. On the other hand, thermal agitation prevent the development of these structures over long

distances.

The well-known hydrophobic properties of hydrocarbons and other nonpolar molecules is closely related to the propensity of water molecules to favor structures in which all four charges depicted in Fig.1.1 are participating to hydrogen bonds. The presence of molecules unable to form hydrogen bonds as are most nonpolar molecules and hydrocarbons forces the surrounding water molecules to reorganize themselves so that none or at least a minimum of their charges point toward the included molecules. Since it implies a more ordered arrangement of the surrounding water molecules, the solvation of non hydrogen bonding molecules is entropically very unfavorable. As a consequence, mixtures of hydrocarbon and water eventually separate into two distinct phases. This allows to minimize the interface between both liquids and therefore the associated energy.

From the three interactions presented above, hydrophobicity, hydrogen bonding and Coulomb interactions are those at the origin of the phenomena of self-assembly of surfactant molecules introduced in the following sections. Surfactant molecules are compounded of a polar head or hydrophilic part covalently bonded to one or several hydrocarbon tails or hydrophobic parts as depicted in Fig.1.3 for the surfactant molecules AOT (Docusate Sodium Salt), SDS (Sodium Dodecyl Sulfate) and CTAB (Cetyltrimethylammonium Bromide).

1.3 Molecular Aggregation of Surfactant

As just mentioned, because they have ambivalent properties, surfactant molecules form structures when in presence of a polar solvent or an apolar one or both. The process leading to the formation of molecular aggregates is governed and therefore well described by the laws of chemical thermodynamics. The shape and size of these aggregates are governed not only by the number of surfactant molecules involved in the structure, but also by the relative volumes occupied by the hydrophilic and hydrophobic parts of the surfactant molecules [1–5]. The

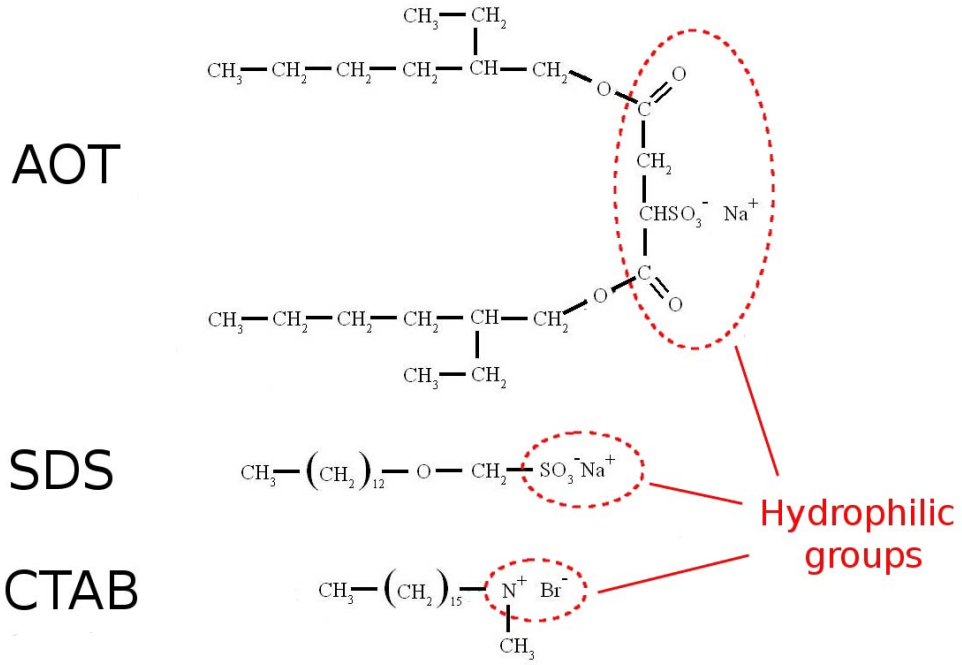

Figure 1.3: developed formula of AOT, SDS and CTAB molecules

latter depending on solution conditions (temperature, nature of the solvents, ionic strength and so on), numerous shapes and size of aggregates can be favored depending which one is the most energetically favorable.

1.3.1 Thermodynamic Approach

Origin of the Self-Assembling Process

At the thermodynamic equilibrium, the chemical potential μ_n of a surfactant molecule involved in the formation of an aggregate of n molecules is the same for all values of n, including $n = 1$ corresponding to isolated molecules or monomer. This previous statement results in equation 1.7 where μ_n^0 is the standard chemical potential for formation of an aggregate of n molecules and X_n the molar fraction

of surfactant in aggregates containing n molecules.

$$\forall n \quad \mu_n = \mu_n^0 + \frac{kT}{n} ln\left(\frac{X_n}{n}\right) \tag{1.7}$$

Using equation 1.7, one can express the molar fraction of surfactant in aggregates of n molecules X_n as a function of the molar fraction of isolated molecules X_1 as in relation1.8.

$$X_n = n\left[X_1 exp\left(\frac{\mu_1^0 - \mu_n^0}{k_B T}\right)\right]^n \tag{1.8}$$

Since X_n and X_1 are molar fractions, their values can not exceed unity. As a consequence, the occurrence of molecular aggregations requires that the variations of the chemical potential μ_n^0 with n present a minimum. Indeed, considering a constant value of μ_n^0 for all n, equation 1.8 simplifies into equation 1.9 so that the molar fraction of surfactant in aggregate of n molecules is inevitably lower than the molar fraction of isolated molecules. Considering increasing values of μ_n^0 with n, the occurrence of large aggregates becomes even less probable.

$$X_n = n\,(X_1)^n \tag{1.9}$$

Let us note n_0 the value of n minimizing μ_n^0 and define X_1^* as follows:

$$X_1^* = exp\left(\frac{-(\mu_1^0 - \mu_{n0}^0)}{k_B T}\right) \tag{1.10}$$

Using equations 1.9 and 1.10, one can express the molar fraction in aggregates of n_0 molecules as a function of the concentration in isolated molecules and X_1^*: $X_{n_0} = n_0\,(X_1/X_1^*)^{n_0}$. As mentioned above, since it is a molar fraction X_{n_0} can't exceed unity. This implies that the concentration in isolated molecules can't exceed X_1^*. As a consequence, as long as the molar fraction in surfactant remains lower than X_1^* most of the molecules are isolated in the solvent. Once X_1 approaches X_1^* the concentration in isolated molecules reaches a plateau value

referred to as Critical Micelle Concentration (CMC) so that any added molecules will preferably take part in the formation of aggregates of n_0 molecules. This phenomena is well-illustrated in Fig.1.4 in which are displayed the evolution of concentrations in isolated molecules and aggregates as a function of the total surfactant concentration.

The existence of an aggregation number n_0 minimizing the chemical po-

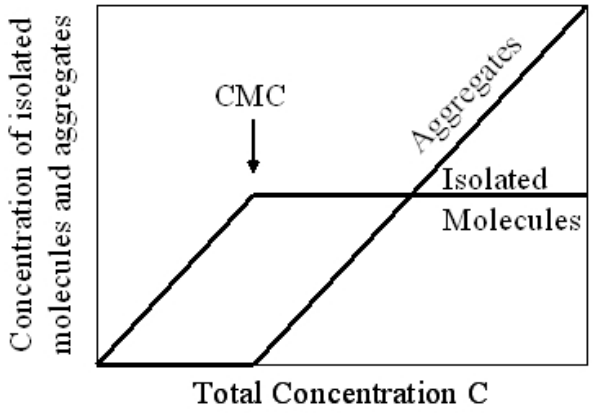

Figure 1.4: Illustration of the evolution of concentration in isolated surfactant molecules and aggregates or Micelles as a function of the total surfactant concentration

tential is related to the molecular structure of the surfactant and its geometrical properties in solution [2, 6]. As mentioned above, the latter are influenced by different parameters as electrolyte concentrations of the polar solvent which influence the surface occupied by the polar head or the length of the hydrocarbons chain of the apolar solvent which control the volume occupied by the hydrophobic tails of the surfactant molecules. As a consequence, the relation between these geometrical parameters and the free energy μ_n^0 of a surfactant molecule involved in the formation of an aggregate of n molecules remains to be defined.

Free Energy of one Aggregated Molecule

The free energy of a surfactant monomer μ_1^0 contains a term, $\acute{g_s}$, accounting for hydrophobic interactions and possibly a term accounting for electrostatic interactions.

Within an aggregate of n surfactant molecules, the free energy, μ_n^0, of one of the molecules involved in its formation has two components. The first, g_s, is a bulk contribution and depend on the temperature as well as on the length of the carbon chain, l_s [2]. Both g_s and $\acute{g_s}$ are non measurable quantities, nonetheless $g_s - \acute{g_s}$ accounts for the energy necessary for a surfactant molecule within an aggregate to solubilize.

The second component of μ_n^0 is a surface contribution. It originated from hydrophobic attractions, surface tensions as well as electrostatic repulsions.

The above hydrophobic attractions are opposed to the hydrophilic forces originating from steric and electrostatic repulsions. Thereby, the polar head area a_s of a surfactant molecule in contact with the polar solvent depend on these opposite attractive and repulsive forces. As a consequence, the free surface energy is minimized for an optimal distance between neighboring amphiphilic molecules.

The shape and the size adopted by the molecular aggregates in a given ternary surfactant system result from a balance between attracting and repulsive interactions. The attracting interactions can be represented for a given hydrocarbon/water interface in the form of a free surface energy, $\gamma \approx 20\,to\,50\,mJ/m^2$ [6]. On the other hand, repulsive interactions contain steric and electrostatic contributions. These are not easily formalised. However, a repulsive contribution varying as the inverse of the polar head area leads to realistic evaluations of the size of the micelles and of the critical micelle concentration [2]. Such a variation is equivalent to what one could expect considering a charged double layer of thickness D and dielectric constant ϵ. Thence one can give *eq.*1.11 as an expression of

μ_n^0 [6].

$$\mu_n^0 = \gamma a_s + \frac{2\pi e^2 D}{\epsilon a_s} + g_s \tag{1.11}$$

Defining the optimal polar head area, a_0 as follows [6]:

$$a_0 = \sqrt{\frac{2\pi e^2 D}{\epsilon \gamma}} \tag{1.12}$$

*eq.*1.11 becomes:

$$\mu_n^0 = \gamma \left(a_s + \frac{a_0^2}{a_s} \right) + g_s = 2\gamma a_0 + \frac{\gamma}{a_s} \left(a_s - a_0 \right)^2 + g_s \tag{1.13}$$

*Eq.*1.13 is only valid for plan self-assembled structures. In the case of curved surfaces a correction of the surface tension γ is necessary. For spherical structures the correction factor on γ is $(1 - \frac{\delta}{R})$ where δ is the radius of one molecule and R the radius of the structures. Besides, it does not take into account any of the interactions between self-assembled molecular structures which can affect their spacial conformation and order. However this thermodynamic approach of the self-assembly process underline the predominant role of the geometrical properties of surfactant molecules in the determination of their favored aggregated structural conformation.

1.3.2 Geometrical Considerations and Consequences

As mentioned in the previous section, amphiphilic molecules start to self-assemble into structures as soon as the total concentration in active molecules oversteps the critical micellar concentration. The shape and the size of the structures assumed by amphiphilic molecules are those minimizing their free energy. However this simple statement circumvents the complexity of the thermodynamic approach since the free energy is itself a function of various parameters [7]. These are the shape of the surfactant molecules, their size, the ionic strength of the polar solvent, the length of the hydrocarbon chains in the apolar solvent, the temperature

as well as the relative concentrations in surfactant and solvents [1, 6]. Consequently, the phase diagram of a given ternary self-assembly systems is usually very rich and therefore hard to predict at first glance [7–10].

Various experimental techniques such as light [11–13], neutrons [14–16] and X-ray scattering [17–19], Nuclear Magnetic Resonance (NMR) [20, 21] as well as Scanning Electron and Optical Microscopy [8, 21, 22] have allowed to characterize the structural properties of ternary self-assembling systems. Thereby, in a given system, surfactant molecules can favor the formation of structures ranging from spherical and cylindrical micelles to ordered lamellar, cubic and hexagonal lyotropic mesophases depending on the parameters mentioned above.

These extensive experimental studies and others have led to the emergence of the *geometrical model* [3, 4, 7, 17, 18, 23] as an adequate and relatively simple description of the structural properties of self-assembling systems. Let us first consider the dilute regime for which the structures formed in ternary systems are not affected by interactions between neighboring structures.

Geometrical Surfactant Parameter and Favored Structures

The geometrical model aims at predicting the shape and size of the structures assumed by amphiphilic molecules as a function of their geometrical characteristics. As shown in Fig.1.5, these are: the polar head area, a_s, the length of their hydrocarbon chains, l_s, and the volume they occupy, v_s.

In the geometrical model, the polar head area is assumed to be optimal, that is $a_s = a_0$. Besides all interactions between polar solvent and surfactant, apolar solvent and surfactant and between surfactant molecules are summarized in a single parameter p_s given in *eq.*1.14

$$p_s = \frac{v_s}{a_0 l_s} \tag{1.14}$$

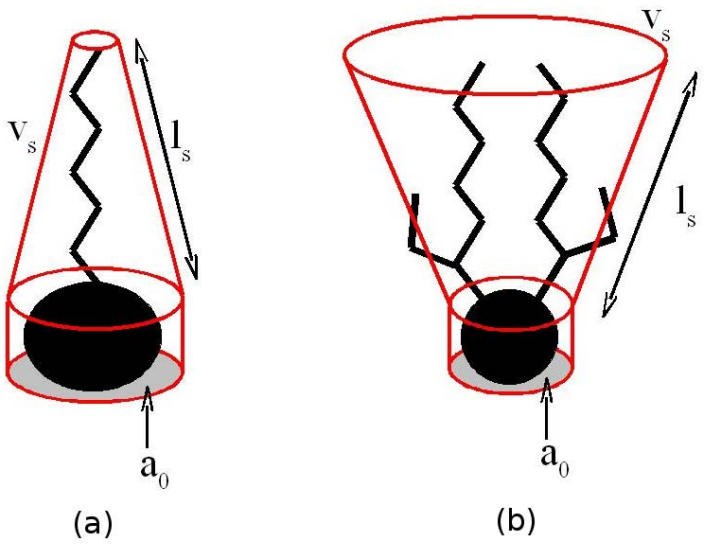

Figure 1.5: Geometrical model of surfactant molecules with different characteristics. (a) 'SDS-like' molecule, (b) 'AOT-like' molecule

The volume v_s and the length, l_s are determined empirically as a function of x, the number of carbon atoms in the hydrocarbon chain, with *eq.*1.15 and *eq.*1.16 respectively [2].

$$v_s \approx (27.4 + 26.9x)\, 10^{-3} nm^3 \tag{1.15}$$

$$l_s \approx (0.15 + 0.1265x)\, nm \tag{1.16}$$

If the length of the hydrocarbon chains constituting the apolar solvent are longer than the hydrocarbon chains of the surfactant molecules as it is the case for iso-octane and AOT, the condition of non-penetration applies [6]. Thence, the volume v_s and the length ,l_s, of the hydrocarbon chain do not vary.

On the other hand, the optimal polar head area depends on the number of water molecules interacting with a given surfactant molecule [1, 6, 24] and possibly on the ionic strength of the polar solvent. Without addition of any counterions, this number is directly related to the relative concentrations in water on one hand and in surfactant on the other hand. For AOT molecules the following empirical

equation applies:

$$a_0 = 0.596 - 0.468exp\left(-0.401\sqrt{w_0}\right) \tag{1.17}$$

with $w_0 = \dfrac{[H_20]}{[AOT]}$, the ratio between water and AOT concentrations.

Thence, variations of the geometrical parameter p_s bring valuable information concerning the structures favored by amphiphilic molecules in a ternary system [1, 6]. Indeed given simple hypothesis accounting for steric packing, the well-known structural evolution from direct spherical micelles to reverse micelles shown in Fig.1.6 is determined as a function of p_s.

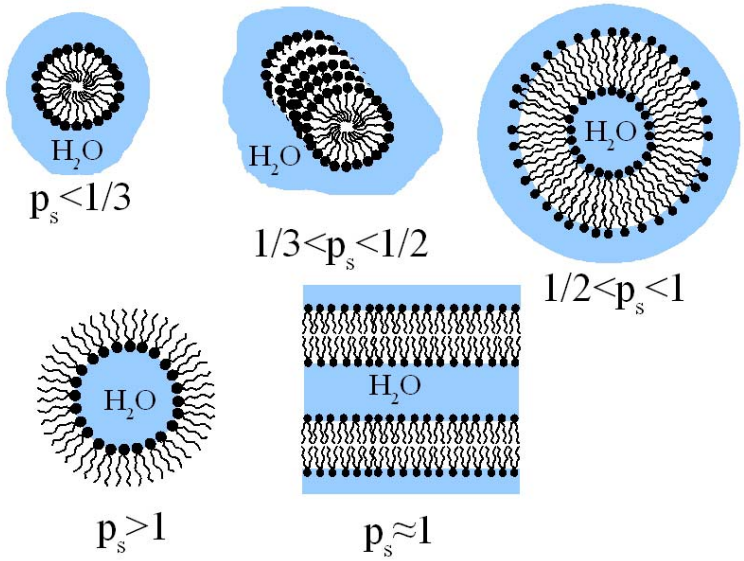

Figure 1.6: Favored structures as a function of the geomatrical surfactant parameter, p_s

Structural Packing: Ordered Phases

In the above section the steric packing of surfactant molecules allows to determine the structures formed in ternary systems. These structures are indeed encountered in ternary systems for which the volume fraction occupied by either direct micelles ($p_s < 1/3$ in Fig.1.6), cylindrical micelles ($1/3 < p_s < 1/2$ in Fig.1.6), bilayers ($1/2 < p_s \leq 1$ in Fig.1.6) or reversed micelles ($p_s > 1$ in Fig.1.6) remains low.

For higher volume fraction, not only the interactions at the surfactant scale need to be considered but interaction between structures as well. Indeed these interactions can lead to the emergence of ordered spacial arrangement at large scales. The characteristics of these lyotropic phases depend mainly on the geometrical surfactant parameter, p_s, the maximum packing parameter, α_p and the water to surfactant concentration ratio, w_0 [6].

Consequently, different ordering such as hexagonal or cubic ones can appear as a function of concentration conditions in a given ternary system. The favored ordering can then be deduced from comparisons between the surfactant volume fraction either in spherical or cylindrical aggregates and the maximum volume fraction allowed for a given conformation [6].

Limitation of the geometrical model

Although, the result of such simple geometrical considerations have proved to be in remarkable agreement with experimental observations, it also shows serious limitations.

Indeed, whereas the temperature and the addition of counterions in the polar solvent strongly influence the polar head area of surfactant molecules, these effects are not accounted for in the previous sections. Besides the hypothesis of non interpenetration of the hydrocarbon chains of apolar solvent and surfactants is not always verified. Such interpenetrations are shown to modify the volume v_s of the surfactant molecules so that the phase diagram of a ternary system depends on the nature of the used apolar solvent. [25–27]

Furthermore, while accounting reasonably well for the structures formed in diluted systems, such geometrical consideration rapidly becomes tedious to describe ternary systems at high volume fractions especially if the coexistence of two phases is considered [6]. The complexity arises from the emergence of long-scales interactions between surfactant aggregates which can not be circumvented

anymore in the model though these are hard to simply formalized in term of 'geometrical parameters' [28].

However and to conclude, in this section we aimed at introduce the complex self-assembling properties of surfactant molecules in the presence of polar and apolar solvents. In spite of serious limitations given above, the geometrical model appears to be the best way of doing so while still preserving the clarity and simplicity of the writing. Let us focus now on the AOT / Iso-octane /Water ternary mixtures studied in this piece of research.

1.4 AOT/Iso-octane/Water Microemulsions

1.4.1 Phase Diagram

Sodium di-2-ethylhexylsulfosuccinate or Aerosol OT (AOT) is an anionic surfactant. As shown in Fig.1.3 and Fig.1.5(b), AOT molecules are compounded of a relatively small polar head (SO_3^- group) bonded to two short hydrocarbon chains. This confers the molecules with amphiphilic properties so that they are accordingly soluble in polar solvent such as water and apolar solvent such as iso-octane [8, 10, 29].

As other amphiphilic molecules in mixed polar and apolar solvents, AOT forms microstructures in which its hydrophobic hydrocarbon chains are swollen in the iso-octane while its hydrophilic polar head points toward water. These microstructures can adopt different shapes and sizes. As mentioned in the previous section the favored shape and size are those minimizing the free energy of each molecules for a given set of conditions (relative concentrations in AOT, water and Iso-octane, temperature, addition of salts to the water,...).

In this piece of research, the effects of the temperature and the presence

of counterions will not be considered. Indeed, all measurements have been performed at the same temperature of $25C$. Furthermore the water used for the samples preparation has been purified and deionized so that its resistivity is $18M\Omega/cm^2$. Besides, AOT and iso-octane have been purchased with 99% and 99.9% purity grades respectively to avoid any additional purification process [10, 29].

AOT-based ternary systems have been studied extensively in the last decades [6, 7, 9–21, 29–33]. The different experimental techniques used in these earlier works have allowed to characterize the different structures favored by AOT molecules in ternary systems as a function of their composition. Notably, the AOT / Iso-octane / water system considered in this study have been characterized by means of cross polarized light microscopy and X-ray scattering by Tamamushi and Watanabe [10]. The ternary phase diagram they determined is illustrated in Fig.1.7.

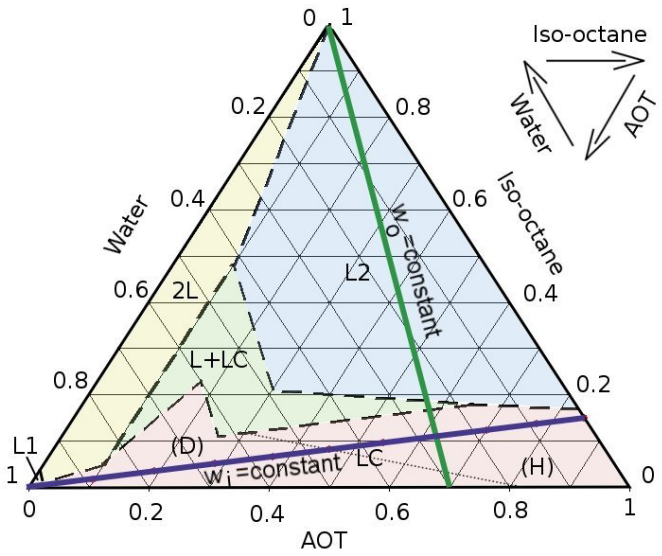

Figure 1.7: Simplified phase diagram of the AOT / Iso-octane / water ternary mixtures at $25C$ [10].

In this phase diagram, $L1$ and $L2$ stands for direct and reversed micellar solution respectively. As expected from geometrical considerations, AOT molecules

clearly favor the formation of reversed micelles (*ie.* 'water-in-oil' microemulsion) rather than direct ones (*ie.* 'oil-in-water' microemulsion). Indeed, the $L2$ region widely extends on the phase diagram over 40 to 50% water content. This remarkable property of AOT-based ternary systems has found numerous applications, notably as microreactors in the synthesis of new nano-materials [6, 12, 18].

Following a dilution line in iso-octane, that is the water to AOT concentration ratio, w_0, is kept constant while the iso-octane content vary (see Fig.1.7), a transition from the isotropic reversed micellar phase $L2$ to lyotropic liquid crystal phases, LC is shown. Here, the intersection of the iso-octane dilution line and the AOT axis is determined by the values of w_0 which decrease as the AOT content increase. Thereby, for intermediate w_0, this dilution line passes by the region $L + LC$ where liquid crystalline structures and micellar structures coexist in equilibrium. At last, further increase of w_0 lead to the unstable phases $2L$ in which two separated phases are formed.

The LC region covers a wide area along the AOT axis. Following now a dilution line in water keeping the iso-octane to AOT concentration ratio, w_i, constant (see Fig.1.7), the ordered structures formed by AOT molecules evolve as a function of the water content. Indeed, a reversed hexagonal conformation is adopted at low water content. On the other hand, an increase of the water content lead to the formation of lamellar structures.

Although well characterized in the $L2$ region, the LC region of AOT-based ternary systems shows a complex transition from Hexagonal to lamellar structures when following a water diltuion line [21, 33]. This complex transition comes along with rich rheological behaviours which remains to be understood at the microscopic and the macroscopic level. In the following chapters we will focus on this characterization by means of usual rheometry, Wide Angle X-ray Scattering and birefringence textures analysis.

1.5 Conclusion

In this chapter, we aimed at introduce the equilibrium properties of self-assembling molecular systems.

To do so, we have considered first the three different molecular forces governing the interactions between molecules in condensed materials. These are the Coulomb interactions, the Van der Waals interactions and the hydrogen bonding interactions. This has allowed us to explain the peculiar amphiphilic properties of surfactant molecules.

In the second section, the self-assembly of surfactant molecules in ternary systems has been addressed. Although the thermodynamic approach does not allow to easily account for the various shapes and sizes of the structures formed by surfactant molecules in ternary systems, it clearly shows the prominent role of the geometrical properties of the surfactant molecules in the 'selection' of a given structural organization. This led us to introduce the *geometrical model* which accounts for the different possible structural organizations of surfactant molecules.

At last, the final section of this chapter has been dedicated to the description of the AOT / Iso-octane / Water phase diagram. Focusing on the liquid crystal region, the rich phase behavior of the lamellar phases has then been emphasized.

We will aim at characterizing the rheological properties of such complex lamellar phases in the second part of this manuscript. Nonetheless, let us first introduce the different experimental techniques we have used and the basic theoretical background on which they rely. These are rheometry, Light and X-Ray scattering and birefringence textures analysis.

References

[1] J. Israelachvili. *Intermolecular and surface forces.* Academic Press, London, 2nd edition, 1992.

[2] C Tanford. Theory of micelle formation in aqueous solutions. *Journal of Physical Chemistry*, 78:2469 – 2479, 1974.

[3] J. Israelachvili, D.J. Mitchell, and B.W. Ninham. Theory of self-assembly of hydrocarbon amphiphiles into micelle and bilayers. *Journal of the Chemical Society - Faraday Transactions II*, 72:1525 – 1568, 1976.

[4] J. Israelachvili, D.J. Mitchell, and B.W. Ninham. Theory of self-assembly of lipid bilayers and vesicles. *Biochemica and Biophysica Acta*, 470:185 – 201, 1977.

[5] R.G. Larson. *The structure and rheology of complex fluids*. topics in chemical engineering. Oxford University Press, New York, 1999.

[6] P. Andre. *D'un Système Colloidal aux Propriétés de Surface*. PhD thesis, Université Pierre et Marie Curie (Paris VI), 2001.

[7] H. Wennerstrom. Ternary phase diagrams in surfactant science. *Journal of Dispersion Science and Technology*, 28:31 – 37, 2007.

[8] P. Ekwall, L. Mandell, and K. Fontell. The cetyhrimethylammonium bromide-hexanoi-water system. *Journal of Colloid and Interface Science*, 29:639 – 646, 1969.

[9] P. Ekwall, L. Mandell, and K. Fontell. Some observations on binary and ternary aerosol ot systems. *Journal of Colloid and Interface Science*, 33:215 –235, 1970.

[10] N.W. Tamamushi and N. Watanabe. The formation of molecular aggregation structure in ternary system: Aerosol ot / water / iso-octane. *Colloid and Polymer Science*, 258:174–178, 1980.

[11] M. Zulauf and H-F. Eicke. Inverted micelles and microemulsions in the ternary system h2o/aerosol ot/isooctane as studied by photon spectroscopy. *Journal of Physical Chemistry*, 83:480–486, 1979.

[12] C. Petit, T. Zemb, and M-P. Pileni. Structural study of microemulsion-based gels at the saturation point. *Langmuir*, 7:223 – 231, 1991.

[13] H.B. Bohidar and M. Behboudnia. Characterization of reverse micelles by dynamic light scattering. *Colloids and Surfaces A: Physicochemical and Engineering Aspects*, 178:313–323, 2001.

[14] M. Kotlarchyk and S-H. Chen. Structure of three-component microemulsions in the critical region determinedby small-angle neutron scattering. *Physical Review A*, 29:2054–2069, 1984.

[15] M. Kotlarchyk, J.S. Huang, and S.H. Chen. Structure of aot reversed micelles determined by smal-angle neutron scattering. *Journal of Physical Chemistry*, 89:4382–4386, 1985.

[16] S.H. Chen, S.L. Chang, R. Strey, and P. Thiyagarajan. Small angl neutron scattering investigation of structural inversion in athree-component ionic micro-emulsion. *Journal of Physics: Condensed Matter*, 3:91–107, 1991.

[17] M-P. Pileni, T. Zemb, and C. Petit. Solubilization by reverse micelles solute localization and structure perturbation. *Chemical Physic Letter*, 118:414–420, 1985.

[18] M-P. Pileni. water in oil colloidal droplets used as microreactors. *Advances in Colloid and Interface Science*, 46:139 – 163, 1993.

[19] H. Gochman-Hecht and H. Bianco-Peled. Structure of aot reverse micelles under shear. *Journal of Colloid and Interface Science*, 288:230–237, 2005.

[20] A. Maitra. Determination of size parameters of water-aerosol ot-oil reverse micellesfrom their nuclear magnetic resonance data. *J. Phys. Chem*, 88:5122–5125, 1984.

[21] P.L. Hubbard, K.M. McGrath, and T. Callaghan. of lamellar domain for an equilibrating lyotropic liquid crystal. *Journal of Physical Chemistry*, 110:20781 – 20788, 2006.

[22] B.A. Coldren, H.E. Warriner, R. Van zanten, J.A. Zasadzinski, and E.B Sirota. Lamellar gels and spontaneous vesicles in catanionic surfactant mixtures. *Langmuir*, 22:2465–2473, 2006.

[23] F. Testard and T. Zemb. Interpretation of phase diagrams: topological and thermodynamical constraints. *Colloids and Surface A: Physicochemical and Engineering Aspects*, 205:3 – 13, 2002.

[24] G.J.M. Koper and W.F.C. Sager. Aggregation in oil-continuous water/ bis(2-ethylhxyl)sulfosuccinate/oilmicroemulsions. *J. Phys. Chem*, 99:13291–13300, 1995.

[25] S.J. Chen, D.F. Evans, B.W. Ninhan, D.J. Mitchell, F.D. Blum, and Pickup S. Curvature as a determinant of microstructure and microemulsions. *Journal of Physical Chemistry*, 90:842 – 847, 1986.

[26] J.M. Chen, Su T.M., and C.Y. Mou. Size of dodecyl sulfate micelle in concentrated salt solutions. *Journal of Physical Chemistry*, 90:2418 – 2421, 1986.

[27] D.F. Evans, D.J. Mitchell, and B.W. Ninhan. Oil, water, and surfactant: properties and conjectured structure of simple microemulsions. *Journal of Physical Chemistry*, 90:2817 – 2825, 1986.

[28] P.G. De Gennes and Taupin C. Microemulsion and the flexibility of oil/water interfaces. *Journal of Physical Chemistry*, 86:2294 – 2304, 1982.

[29] H. Kunieda and K Shinoda. Solution behavior of aerosol ot/water/oil system. *Journal of Colloid and Interface Science*, 70:577 –583, 1979.

[30] J.B. Peri. The state of solution of aerosol ot in nonaqeous solvents. *Journal of Colloid and Interface Science*, 29:6 –15, 1969.

[31] A Kitahara, K. Watanabe, K. Kon-no, and T Ishikawa. Mechanism of solubilization of water by oil-soluble surfactant solutions - i. anionic surfactant. *journal of colloid and interface science*, 29:48 – 54, 1969.

[32] I Lundstrom and K. Fontell. Lateral electrical conductivity in aerosol ot systems. *Journal of Colloid and Interface Science*, 59:360 – 370, 1977.

[33] M. Kotlarchyk, E.Y. Sheu, and M.Capel. Structural and dynamical transformations between neighboring dense microemulsion phases. *Physical Review A*, 46(2):928–939, 1992.

[34] A. Leon, D. Bonn, J. Meunier, A. Al-Kahwaji, and O. Greffier andH. Kellay. Coupling between flow and structure for a lamellar surfactant phase. *Physical Review Letters*, 84:1335–1338, 2000.

[35] L. Courbin and P. Panizza. Shear-induced formation of vesicles in membrane phases: Kinetics and sizeselection mechanisms, elasticity versus surface tension. *Physical Review E*, 69(2):021504(1) – 021504(12), 2004.

[36] O. Diat, D. Roux, and F. Nallet. Effect of shear on a lyotropic lamellar phase. *Journal de Physique II France*, 3:1427–1452, 1993.

[37] J. Bergenholtz and N.J. Wagner. Formation of aot/brine multilamellar vesicles. *Langmuir*, 12:3122–3126, 1996.

[38] L. Courbin, J.P. Delville, J. Rouch, and P. Panizza. Instability of a lamellar phase under shear flow: Formation of multilamellarvesicles. *Physical Review Letters*, 89(14):148305(1) – 148305(4), 2002.

Chapter 2

Rheology & Rheometry

Contents

Résumé du Chapitre 2

Dans ce second chapitre nous introduisons d'abord les notions de bases de la rhéologie que sont le tenseur des déformation, le tenseur des taux de déformation et le tenseur des contraintes. Cela nous permet d'introduire la notion de loi constitutive qui relie le tenseur des taux de déformation et le tenseur des contraintes.

Une fois ces simples notions introduites, nous présentons la notions de cisaillement qui est souvent utilisée en rhéométrie. Alors que pour les fluides newtoniens la relation entre le taux de cisaillement et la contrainte de cisaillement est linéaire et indépendante du temps, ceci n'est plus vrai pour des matériaux plus complexes. Quelques exemples de comportements typiquement non newtonien sont alors présentés notamment les effets de contrainte normale, de vicoélasticité, de thixotropie et rheopexie ainsi que les notions de contrainte seuil et de vieillissement.

Dans une troisième et dernière partie ce chapitre introduit les différent appareils de mesure utlisés pour caractériser le comportement rhéologique en cisaillement des matériaux étudiés dans ce travail. Nous nous attardons notament sur la description et la résolution du problème de couplage inertiel au début des mesures de fluage à l'aide du modèle viscoélastique de Maxwell-Jeffrey.

2.1 Introduction

At the start of the XXth century the theories used until then to describe either liquids or solids failed to describe a new class of materials of which the properties were between these two states. This leads to the development of new theories and experimental techniques which aimed at characterizing and understanding the deformation and flow properties of such materials which are now referred to as complex fluids. This field of science is now known as rheology and has never stopped to be enriched since then. The outcomes of rheology have lead to the development of exceedingly various applications ranging from products used on a daily basis as soaps, foams, rubbers and so on to highly specialized materials. The following section presents the basic notions on which rheological theories rely on as well as some of the main results concerning the rheology of soft jammed systems [4, 5, 8].

2.2 Basic Notions in Rheology

As mentioned above, rheology aims at characterizing the relation existing between the strain, the strain rate and the stress within materials. One usually distinguishes purely viscous materials as newtonian fluids, purely elastic materials as crystalline solid in a certain extend and viscoelastic materials which properties lay between those of purely elastic and purely viscous materials. Prior to any presentation of specific experimental setups usually used to characterize the flow properties of a complex fluid, the next section will introduce the notions of velocity gradient tensor and stress tensor. This latter two are useful mathematical expressions to describe deforming materials under forces.

2.2.1 Velocity Gradient Tensor and Stress Tensor

Velocity Gradient, Rate-of-Deformation and Vorticity Tensors

Let us consider a point in three dimensional space defined by it's Cartesian coordinates $\vec{x} \equiv (x_1, x_2, x_3)$. The velocity vector at point $\vec{x}$ is also defined here by $\vec{v}(\vec{x}) \equiv (v_1(\vec{x}), v_2(\vec{x}), v_3(\vec{x}))$ where v_1, v_2 and v_3 are the components of the velocity in directions parallel to the directions '1', '2' and '3' respectively. The i, j components of the Velocity Gradient Tensor $\nabla \mathbf{v}$ are then given by the following expression:

$$\nabla \mathbf{v}_{i,j} = \left(\frac{\partial v_j}{\partial x_i} \right)_{i,j=1,2,3} \tag{2.1}$$

Considering $\mathbf{v}_0$ as being the velocity of any given point in the flow with the origin $\mathbf{x}_0$ being chosen arbitrarily, the velocity of a nearby point $\mathbf{x}$ is then given as a function of the velocity gradient by the next relation:

$$\vec{v}(\vec{x}) = \vec{v}_0 + (\vec{x} - \vec{x}_0) \cdot \nabla \mathbf{v} \tag{2.2}$$

Equation 2.2 illustrates the physical significance of the velocity gradient tensor which represents the steepness of the velocity variations from points to points in any direction of a flow.

Considering a fluid element in a flow, it is always possible to consider its deformation as a combination of a given stretching and a given rotation. These two components of any flow deformation correspond to the definition of the 'rate-of-deformation' tensor $\mathbf{D}$ and the vorticity tensor $\boldsymbol{\omega}$ which are respectively the symmetric and antisymmetric part of the gradient tensor given by equation 2.3 and 2.4 respectively.

$$\mathbf{D} = \frac{1}{2} \left(\nabla \mathbf{v} + \nabla \mathbf{v}^T \right) \tag{2.3}$$

$$\boldsymbol{\omega} = \frac{1}{2} (\nabla \mathbf{v} - \nabla \mathbf{v}^T) \tag{2.4}$$

Stress Tensor

Let us consider now an infinitesimal cube of material within a flow (see Fig.2.1). $\left(d\vec{F}_j\right)_{j=1,2,3}$ being the forces exerted by the material exterior to the cube on its face perpendicular to the j direction and $(dF_{ij})_{i,j=1,2,3}$ their components on the i directions, the stress vector $\vec{T}(M,\vec{n})$ at the center M of a surface ds oriented by the normal vector $\vec{n}$ is defined by:

$$d\vec{F} = \vec{T}(M,\vec{n})ds \tag{2.5}$$

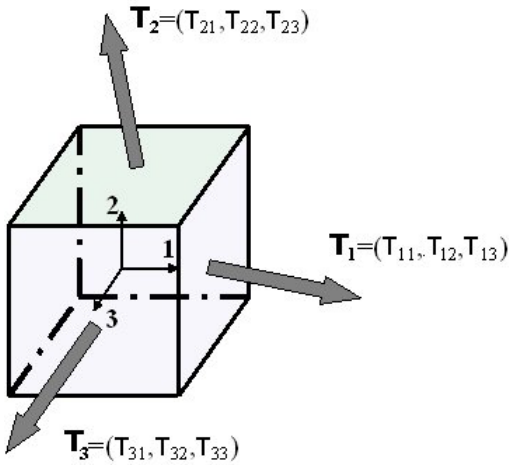

Figure 2.1: Definition of the state of stress in terms of forces acting on the faces of an unit cube

Thence, the state of stress tensor $\mathbf{T}(M)$ is defined by *eq.*2.6.

$$\vec{T}(M,\vec{n}) = \mathbf{T}(M).\vec{n} \tag{2.6}$$

The ij components T_{ij} of the state-of-stress tensor $\mathbf{T}(M)$ are then given by the following expression:

$$T_{ij} = \left(\frac{\mathbf{dF}_{ij}}{ds}\right)_{i,j=1,2,3} \tag{2.7}$$

In a fluid under hydrostatic pressure, the state-of-stress tensor simplifies in an isotropic tensors given by equation 2.8 in which $\boldsymbol{I}$ stands for the unit tensor for which all diagonal components are unity while all non-diagonal components are null.

$$\mathbf{T} = -p\boldsymbol{I} \tag{2.8}$$

As only pressure gradients affect the flow motion of an incompressible fluid, the state of stress tensor is usually decomposed as follows:

$$\mathbf{T} = \boldsymbol{\sigma} - p\boldsymbol{I} \tag{2.9}$$

In which $\boldsymbol{\sigma}$, the extra stress tensor, accounts for the forces affecting the motion of the fluid. One can notice here, that $\boldsymbol{\sigma}$ is not completely defined as adding an isotropic tensor of any given magnitude to $\mathbf{T}$ or $\boldsymbol{\sigma}$ does not affect the flow motion of the fluid.

The relation between $\mathbf{D}$ and $\boldsymbol{\sigma}$ constitutes what is usually referred to as the constitutive equation of a fluid. Depending on its properties, especially degree of anisotropy, history dependence and elasticity, the constitutive equation of a given fluid can present various forms with different degree of complexity. Whereas the constitutive equation 2.10 of Newtonian fluids is linear and implies only one parameter, the shear viscosity η, the constitutive equation of some particularly complex fluids still remains to be formulated.

$$\boldsymbol{\sigma} = 2\eta\mathbf{D} \tag{2.10}$$

2.2.2 Shearing Flows

Among the different flow configurations used in rheometry to characterize the flow properties of a material, shearing flows are certainly the simplest. Indeed, in such flows, several of the components of the *stress* tensor and the *rate-of-deformation*

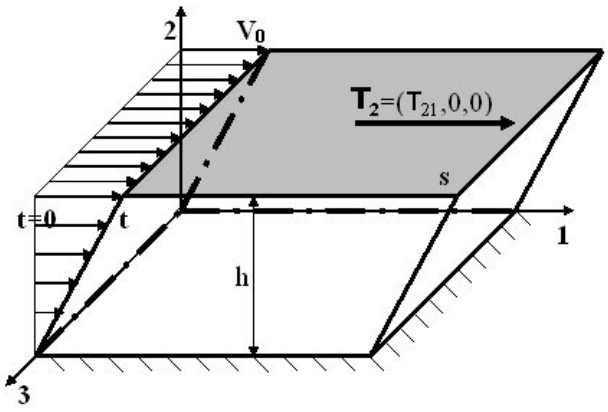

Figure 2.2: deformation induced by a shearing flow

tensor become null. Different flow geometries can be used with various level of approximation to produce an homogeneous shear state of stress and strain within a fluid. The easiest way to illustrate shearing flow is by considering the flow of a fluid confined between two parallel plates, one being fixed and the other one moving at a constant velocity V_0 as displayed in Fig2.2. We assume here that the flow is laminar; that is, the convective terms due to inertial effects in the Navier-Stokes equations can be neglected. In addition, we will consider a no-slip boundary condition at the interface between the plates and the fluid so that equations 2.11 and 2.12 are verified. In such conditions, the deformation of the material bulk can be considered as the sliding of thin fluid layers one over the others.

$$v_1(x_2 = 0) = 0 \tag{2.11}$$

$$v_1(x_2 = h) = V_0 \tag{2.12}$$

Then, considering a 2D flows, the only non null component of the velocity at a distance x_2 from the fixed plate is given by the following relation:

$$v_1(x_2) = \frac{V_0}{h} \cdot x_2 \tag{2.13}$$

So that *the rate-of-deformation* tensor is simply given by:

$$D_{12} = D_{21} = \frac{V_0}{2h} = \frac{\dot{\gamma}}{2} \tag{2.14}$$

where $\dot{\gamma}$ is referred as the shear rate. In the same way, such flow conditions give rise to a simple expression of the *stress* tensor $\boldsymbol{\sigma}$. Indeed, the relative movement of each layer induces friction forces corresponding to the necessary force to move the upper plate F_2. Noting s the surface of the plates, the component σ_{12} of the stress tensor usually referred to as the shear stress is given by the following expression:

$$\sigma_{12} = \sigma_{21} = \frac{F_{21}}{s} \tag{2.15}$$

The shear viscosity of a material is defined in equation 2.16 as the ratio between the shear stress σ_{12} and the shear rate $\dot{\gamma}$. In the simplest case of newtonian fluids, the shear viscosity is constant so that the shear stress σ_{12} is directly proportional to the shear rate $\dot{\gamma}$. Furthermore, the shear stress is the only non null component of the stress tensor, so that the knowledge of the shear viscosity is sufficient for a complete characterization of the shear flow behaviors of newtonian fluids.

$$\eta = \frac{\sigma_{12}}{\dot{\gamma}} \tag{2.16}$$

In complex fluids, the relation between the shear stress and the shear rate is not that simple. Indeed, the shear stress experienced by the sample can be dependent of the applied stress or the shearing time. In some cases the shearing process induces normal forces so that the diagonal components of the stress tensor are no more null. As a consequence, knowing the shear viscosity at a given shear rate is no more sufficient to characterize the material flow properties. Therefore, the shear stress to shear rate ratio of equation 2.17 is often referred to as the *apparent shear viscosity*

$$\eta(\dot{\gamma}, t) = \frac{\sigma_{12}(\dot{\gamma}, t)}{\dot{\gamma}} \tag{2.17}$$

2.3 Non-Newtonian Behaviors

As mentioned in the previous sections, knowing the shear viscosity of a newtonian fluids is sufficient to predict its behavior in other flow configurations. However, unlike for newtonian fluids, the internal structures of complex materials such as those considered in what follows depend on the flow conditions and conversely. These *flow-structures* interactions ultimately result in the emergence of non-linear and time-dependent terms in the constitutive equations controlling their flow properties [5–8].

In the case of lyotropic liquid crystal phases such as those considered in this study, not only the orientation and order of the internal structures can be affected by the flow, but the structures favored by amphiphilic molecules can also undergoes shear induced transition as in the shear induced formation of multilamellar vesicles [7, 9, 10]. That way, a lyotropic lamellar phase can show extremely rich rheological behaviors depending on the regime of strain rate or stress considered and the level of interactions involved. Indeed, the shear induced formation of bilayers free of any topological defects and well aligned lead to *quasi-newtonian* behavior (*ie.* a constant shear viscosity on a significant range of shear rate or shear stress) [11]. On the other hand, the emergence of topological defects or the existence of strong interactions between bilayers can lead to radically different rheological behaviors similar to those encountered in concentrated suspensions in the glassy state, foams, concentrated emulsions and other *soft jammed systems* [12–16].

Since such complex systems are used on a daily basis in many industrial as well as natural processes, the literature concerning their rheological properties have never ceased to grow. The different non-newtonian behaviors one has to consider in a study of these systems are reported in the followings.

2.3.1 Normal Stress in Shearing Flows

Some macromolecules like polymers or amphiphilic structures in solutions present the properties of being able to stretch and orient themselves according to the flow field when sheared [6, 17–20]. This usually results in the emergence of diagonal terms in the *stress* tensor. The microscopic reorganization of the structures in a shear flow as the one depicted in Fig.2.2 generates macroscopic effects consisting in the emergence of a normal force (along direction 2) which tends to either push the two parallel plates apart or pull them closer depending on its sign. As mentioned in the previous definition of the *stress* tensor, $\boldsymbol{\sigma}$ is determined to within an additive isotropic tensor so that only the first and second normal stress differences defined in equations 2.18 and 2.19 can be measured. In practice, only N_1 is conveniently measured with usual apparatus [4].

$$N_1 = \sigma_{11} - \sigma_{22} \tag{2.18}$$

$$N_2 = \sigma_{22} - \sigma_{33} \tag{2.19}$$

The emergence of normal forces within a steadily sheared material is usually a good indication of its elastic properties. Materials presenting both viscous and elastic properties are referred to as viscoelastic fluids. The characterization of their so-called viscoelastic properties can necessitate a dynamic approach which is described in the following section.

2.3.2 Viscoelasticity

As mentioned above, viscoelastic fluids present intermediate properties to those of a purely viscous fluid and those of an elastic solid. As a consequence, viscoelastic materials are characterized by two modulus, the loss modulus $G''(\omega)$ and the storage modulus $G'(\omega)$. These latter correspond respectively to the ability of viscoelastic fluids either to dissipate energy in viscous friction or to store

it in the form of elastic energy. Such properties are controlled by the rate of spontaneous rearrangement or relaxation of the microstructures within the fluid which depends on the frequency ω at which it is solicited. $G''(\omega)$ and $G'(\omega)$ are only defined for deformations of the sample small enough to ensure that the microscopic structures formed within the fluids are not significantly affected by the flow. Such deformation conditions correspond to what is usually called the linear viscoelastic regime. The characterization of the viscoelastic properties of a material can be achieved by imposing small-amplitude oscillating shear strains in the form $\gamma(t) = \gamma_0 sin(\omega t)$ in which γ_0 is the strain amplitude of the oscillation and ω their frequency in $rad.s^{-1}$.

In the linear viscoelastic regime, the shear stress response $\sigma(t)$ to small-amplitude sinusoidal strains is also sinusoidal and its amplitude is proportional to the amplitude of the strains γ_0. The elastic component of the shear stress response is in phase with the strain γ while its viscous component is in phase with the rate of strain $\dot{\gamma}$. Therefore, in the viscoelastic regime σ is related to the imposed strain by equation 2.20.

$$\sigma(t) = \gamma_0(G'(\omega)sin(\omega t) + G''(\omega)cos(\omega t)) \tag{2.20}$$

The relaxation process of the structures within the fluid is usually complex and involves several characteristic times [21–23]. However, some fluids known as Maxwell fluids present a unique relaxation time τ. Maxwell fluid can be compared to a spring of elastic modulus G_0 associated in serial with a 'dash pot' of viscosity η so that $\tau = \frac{\eta}{G_0}$ is the relaxation time of the system. The storage modulus $G'(\omega)$ and the loss modulus $G''(\omega)$ are then given by relations 2.21 and 2.22.

$$G'(\omega) = \frac{G_0\omega^2\tau^2}{1+\omega^2\tau^2} \tag{2.21}$$

$$G''(\omega) = \frac{G_0\omega\tau}{1+\omega^2\tau^2} \tag{2.22}$$

Other models which are not presented here have been developed to take into account multiple relaxation times or more specific features associated with the complex viscoelastic properties presented by some materials. However, as long as the applied sinusoidal strain corresponds to the linear viscoelastic regime, $G'(\omega)$ and $G''(\omega)$ measurements bring information on either a given material behaves more as a solid ($G'(\omega) > G''(\omega)$) or a liquid ($G'(\omega) < G''(\omega)$). However, $G'(\omega)$ and $G''(\omega)$ are defined and therefore meaningful only in the linear viscoelastic regime. Besides, this regime can reduce to extremely small range of applied strain or stress for some given systems. As a result, other experimental methods based on the analysis of large amplitude oscillation shear or of free damped oscillation at the start-up of creep measurement can become necessary to characterize the viscoelastic properties of some complex materials. A complete description of the latter method is given in the following sections of this chapter.

2.3.3 Thixotropy and Rheopexy

When sheared at a constant shear rate $\dot{\gamma}$ or submitted to a constant shear stress σ, some complex fluids exhibit time-dependent apparent shear viscosity $\eta(\dot{\gamma}, t)$. Depending if the apparent shear viscosity tends to decrease or increase after a steep increase from one constant shear rate to another and conversely to increase or decrease after a steep decrease between two constant shear rates, this time-dependent phenomenon is either called thixotropy or rheopexy respectively [24]. Unless the viscosity reach a steady value after a time dependent or transient regime, the rheological characterization of thixotropic and rheopectic fluids becomes extremely complicated. Indeed, in such cases, one would need to know the whole shear stress and strain history of a sample in order to predict its behavior.

Such thixotropic and rheopeptic behaviors are often encountered in structured fluids as liquid crystals [6, 17, 18, 25, 26] or in materials in which elementary

structural units strongly interact with their neighbors. The time-dependence of their flow properties arise from flow induced structural rearrangements. These either concern the positional and orientational orders of the internal structures or even shear induced transitions from a given internal structure to another.

To characterize the flow properties of thixotropic and rheopectic fluids one can either chose to impose a constant shear rate and monitor the shear stress evolution as a function of the time or conversely, impose a constant shear stress and monitor the shear strain. Although these two methods might seem equivalent, the energy density brought to the sample differs. As a consequence, the time scale of the structures rearrangement and thus the transient regime of the flow is likely to depend on the used method.

At last, it can be mentioned that the definition given above is one of the two commonly accepted definitions of thixotropy and rheopexy [24]. Indeed some may understand thixotropy as the property of some concentrated gels to liquefy with time when sheared and to solidify again when left at rest [24]. In fact, as shown in the following paragraph such a definition corresponds to the yielding, rejuvenation and aging phenomena observed in soft jammed systems [12–16].

2.3.4 Yielding, Rejuvenation and Aging

Some complex fluids, usually ordered phases or glassy liquid near the glass transition, behave as elastic solid when under low stresses and only start to flow when the applied stress becomes higher than a critical value τ_y. This critical stress is referred to as the yield stress. The yield stress phenomenon is directly related to the intermolecular forces which ensure that the molecules or the molecular aggregates forming a given material are closely bind together either in an ordered form or a glassy one. Because of these strong binding forces, the molecules or the molecular aggregates occupy a fixed position in the materials when compared to the molecules within a purely viscous liquid. In order to change its position within

the materials, a molecule or a molecular aggregate constituting the elementary unit need to overcome an energetic barrier. At a macroscopic scale, this energetic barrier results in the emergence of the yield stress over which the materials start being irreversibly deformed.

If, once it starts flowing, the fluid present a constant apparent viscosity η_p, the fluid is referred to as a Bingham fluid and its rheological properties are simply described by the constitutive equation 2.23.

$$\dot{\gamma} = \begin{cases} 0 & if\ \sigma_{12} < \tau_y \\ \sigma_{12} = \tau_y + \eta_p \dot{\gamma} & if\ \sigma_{12} > \tau_y \end{cases} \tag{2.23}$$

In spite of real engineering applications, the above definition of *yield stress* does not allow to account for the extremely slow and irreversible deformation process occurring in soft jammed systems and some other materials under low stresses [12, 27]. This phenomenon is at the origin of a long living controversy concerning the very existence of the yield stress [28]. Because of its similarities with the primary creep of solid materials such as metallic alloys and others, this slow deformation process is called primary creep [27, 29]. In soft jammed systems and other glassy materials the time length of the primary creep can evolve from seconds to hours and even days depending on the level of interactions involved between neighboring structural units and the level of local stress they experienced. The end of this primary creep corresponds to a transition from a solid-like behavior to a fluid-like one. This fluidification corresponds to the collapse of the interaction network between internal structures [8, 24, 30]. Unlike for true solid material, the collapse of this interaction network is reversible so that an apparent solid state can be recovered once the material is left at rest. The terms *rejuvenation* and *aging* are often used in the literature to refer to these fluidification and solidification processes respectively.

As previously mentioned, both rejuvenation and aging phenomena in glassy

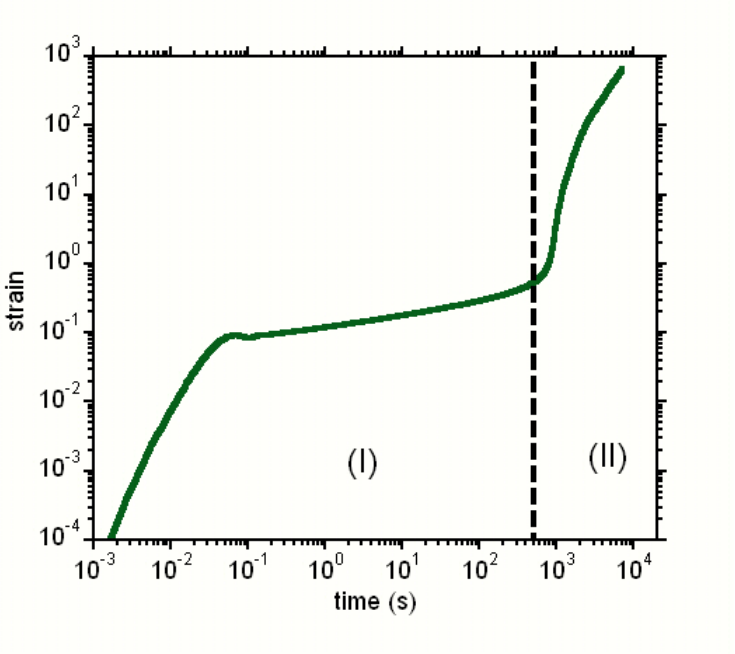

Figure 2.3: Typical evolution of the strain as a function of time for a constant applied shear stress on a given glassy material. At short times (I), an almost *solid-like* behaviour is shown while at long times (II), the material *flows*.

materials are temporal processes. Consequently they are sometimes considered as effects of thixotropy or rheopexy [24]. Besides the time scales involved range from few seconds to hours so that a given glassy material can present radically opposed behaviors depending on the experimental time window considered as shown in Fig.2.3. Indeed, at short times the strain curves shown in Fig.2.3 corresponds to an elasto-plastic behavior. On the other hand, the sample behave as viscoelastic fluids at long times. From an experimental point of view, this latter remark involves that the shear history of a given sample has to be carefully controlled prior to perform any meaningful analysis of the results.

2.4 Rheometry: Technologies and Methods

In the following section, we will describe the different experimental devices and techniques used to understand the macroscopic rheological properties of the AOT / Iso-octane / Water self-assembling systems investigated in this piece of research.

In a first section, we will discuss the functioning of both types of rheometers used in this study, namely stress and strain controlled rheometers. The relation between the technologically controlled parameters and the rheological parameters, *ie.* the shear stress and the shear rate, will be defined for the different shear cell geometries considered in the following studies.

In a second section, we describe the experimental procedures which have been followed to obtain reliable and reproducible data. A model allowing to determine the viscoelastic properties of the investigated sample from an analysis of the inertial coupling at the start-up of creep measurements will be detailed.

2.4.1 Shear Rheometry

Strain and Stress Controlled Shear Rheometers

In this study, transient strain and stress controlled measurements were performed with a rheometer ARES (Rheometrics Scientific) and a rheometer ARG2 (TA Instruments) respectively. Unlike stated in their names, the physical parameters controlled or measured either by a strain or a stress controlled rheometer are not the strain and the stress. Indeed these later quantities are mesoscopic ones and therefore not directly measurable mechanically. Instead, strain and stress controlled rheometers are designed with a moving shaft dragged respectively by a motor of which either the angular velocity or the torque are precisely controlled.

The angular velocity (*resp.* torque) is applied to the studied sample through the use of a shear cell in which the sample is loaded. The torque (*resp.* angular displacement) induced by this mechanical solicitation is then monitored by mean of a transducer (*resp.* an angular displacement captor) attached to the fixed part

(*resp.* the moving part) of the rheometer. The relations between the torque and the angular velocity and their mesoscopic counterparts, the shear stress and the shear rate, can then be determined as a function of the chosen shear cell geometry as discussed in the following paragraphs.

Besides, strain-controlled rheometers are designed with powerful motor so that they can supply the energy necessary to deform the sample in a controlled manner. On the other hand, stress-controlled rheometers are designed with motors of which the torque is precisely controlled. Here the torque-related stress applied to the tested sample and corresponding to the energy density experienced by the sample is precisely controlled. A consequence of this is that the response time-scale of thixotropic material and soft jammed systems is likely to be sensitive to the used technology.

Shear Cell Geometries: Macroscopic to Mesoscopic Relations

We have used the three usual shear cell geometries in our rheological measurements. These are the cup and bob or Couette geometry, the cone and plate geometry and the parallel plates geometry. In the following paragraphs, the relations between the torque and the angular velocity and the shear stress and the shear rate are introduced. To preserve the clarity of the writing, we will assume the shear flow to be newtonian, laminar, isothermal and steady.

- **Cup and bob shear cells**

As shown in Fig.2.4, in cup and bob geometries the sample is loaded between to concentric cylinder of respective radius R_1 and R_2, one being fix and the other moving. Either the angular velocity Ω or the torque Γ is the controlled parameter does not change the relations between these macroscopic and measurable quantities and their mesoscopic counterparts within the sample, the shear rate $\dot{\gamma}$ and the shear stress σ_{12}. Let us now determine these relations.

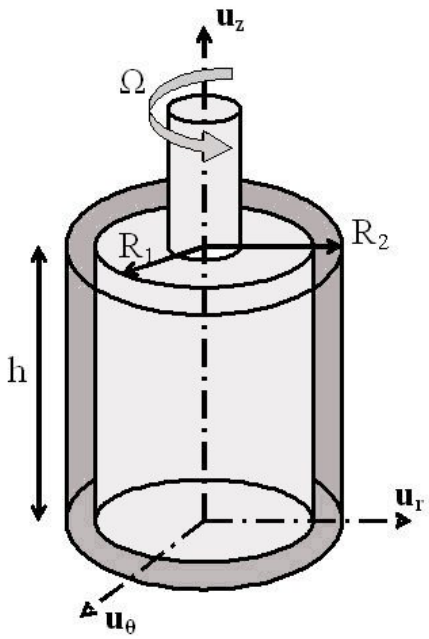

Figure 2.4: Cup and Bob Geometry

Taking into account the symmetry of the velocity field, $\mathbf{v} = v_\theta(r)\mathbf{u}_\theta$, $\sigma_{r\theta} = \sigma_{12}$ is the only component of the stress tensor which is not null. Thenceforwards, the Navier-Stokes equation in cylindrical coordinate reduces to *eq.*2.24 where r is the distance to the $\mathbf{u}_z$ axis.

$$0 = -\frac{1}{r^2}\frac{\partial}{\partial r}(r^2\sigma_{r\theta}) \tag{2.24}$$

One can therefore deduces:

$$\sigma_{12} = \frac{\sigma_1 R_1}{r^2} \tag{2.25}$$

where $\sigma_1 = \dfrac{\Gamma}{2\pi h R_1^2}$ is the stress applied on the inner cylinder ($r = R_1$).

It can be noticed here that the shear stress is not uniform through the gap of cup and bob geometries.

To determine the shear rate $\dot{\gamma}(r)$, one has first to determine the velocity profile of the flowing fluid along the gap of the shear cell. Indeed, $\dot{\gamma}(r)$ is given

in cylindrical coordinates as a function of $v_\theta(r)$ by *eq.*2.26

$$\dot{\gamma} = r\frac{\partial}{\partial r}\left(\frac{v_\theta}{r}\right) \tag{2.26}$$

Considering first the simple case of a newtonian fluid with a viscosity η, the stress is then given by *eq.*2.27

$$\sigma_{r\theta} = \eta\left(r\frac{\partial}{\partial r}\left(\frac{v_\theta}{r}\right)\right) \tag{2.27}$$

The Navier-Stokes equation 2.24 can then be rewritten as follows:

$$\frac{\partial}{\partial r}\left(r^3\frac{\partial}{\partial r}\left(\frac{v_\theta}{r}\right)\right) = 0 \tag{2.28}$$

Thence, the velocity profile along the gap is in the form of:

$$v_\theta = ar + \frac{b}{r} \tag{2.29}$$

In *eq.*2.29, a and b are constants determined by considering the following no-slip boundary conditions: $v_\theta(r = R_1) = R_1\Omega$ and $v_\theta(r = R_2) = 0$.

Thence, the velocity profile of a newtonian fluid along the gap of a cup and bob shear cell is given by *eq.*2.30 and the exact expression of the shear rate by *eq.*2.31.

$$v_\theta = \Omega r\frac{(R_2/r)^2 - 1}{(R_2/R_1)^2 - 1} \tag{2.30}$$

$$\dot{\gamma}(r) = \frac{2\Omega R_1^2 R_2^2}{(R_2^2 - R_1^2)\, r^2} \tag{2.31}$$

As the shear stress, the shear rate profile is therefore not uniform along the gap of cup and bob shear cells. As a consequence, the values one can deduce from macroscopic measurements are not exact but mean values along the gap calculated as follows:

$$\langle\sigma\rangle = \frac{1}{R_2 - R_1}\int_{R_1}^{R_2}\frac{\Gamma}{2\pi h r^2}dr = \frac{\Gamma}{2\pi h R_1 R_2} \tag{2.32}$$

$$\langle\dot{\gamma}\rangle = \frac{1}{R_2 - R_1}\int_{R_1}^{R_2} \frac{2\Omega R_1^2 R_2^2}{(R_2^2 - R_1^2)\, r^2} dr = \frac{2\Omega R_1 R_2}{(R_2^2 - R_1^2)} \tag{2.33}$$

*Eq.*2.32 and *eq.*2.33 can simplify into *eq.*2.34 and *eq.*2.35 if the gap separating both cylinders is small when compared to their radius of curvature: $R_2 - R_1 << R_1$. This later condition being verified in our experiments, we will use these approximate values of stress and shear rate in the following.

$$\sigma \approx \frac{\Gamma}{2\pi h R_1^2} \tag{2.34}$$

$$\dot{\gamma} \approx \frac{R_1 \Omega}{R_2 - R_1} \tag{2.35}$$

- Cone and plate shear cells

The second class of shear cells used in this piece of research are cone and plate geometries. As shown in Fig.2.5, now the sample is loaded between two coaxial fixtures: a truncated cone (the truncation is about $50\mu m$ and therefore not shown in Fig.2.5) and a plate. The truncated cone is positioned so that its virtual vertex coincides with the centre of the fixed plate.

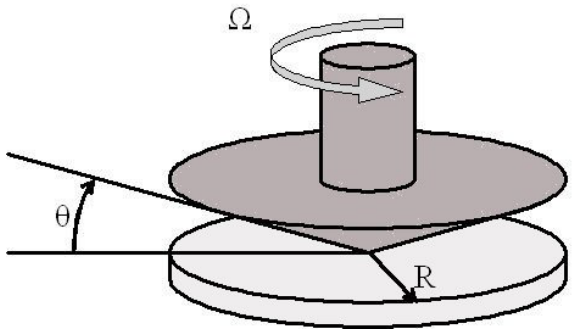

Figure 2.5: Cone and plate geometry

For small enough values of the cone angle ($\theta \leq 4$), the velocity profile between the cone and the plate at a given radius r can be considered as linear. Therefore both the shear rate and the shear stress are uniform in the whole sample volume. These are simply given in *eq.*2.36 and *eq.*2.37 as a function of the

plate radius R, the torque applied to the moving part of the rheometer Γ and the cone angle θ.

$$\dot{\gamma} = \frac{v_\theta(r)}{h(r)} = \frac{r\Omega}{r\,tan(\theta)} = \frac{\Omega}{tan(\theta)} \tag{2.36}$$

$$\sigma = \frac{3\Gamma}{2\pi R^3} \tag{2.37}$$

Besides, the cone and plate geometry is not only the only geometry ensuring uniform shear stress and rate within the tested sample but it also allows to measure the first normal stress difference N_1 by measuring the vertical force F_z applied on the cone by the sheared sample.

$$N_1 = \sigma_{11} - \sigma_{22} = \frac{2F_z}{\pi R^2} \tag{2.38}$$

Cone and plate geometries have the undeniable asset to generate uniform shear rates and shear stresses. However, these geometries are not suitable to characterize the rheological properties of complex fluids with internal structures larger than the cone truncation. Indeed, in that case the basic postulates on which the continuum mechanic has been developed becomes invalidated. As shown in the following chapters, this can indeed severely affects the measurements.

- **Parallel plates shear cells**

The last class of shear cells considered in our studies are the parallel plate geometries. As expected and shown in Fig.2.6, the sample is loaded between two coaxial parallel plates. Here, the distance between both plates is constant along a radius so that neither the shear stress or the shear rate are uniform within the investigated sample. Indeed, according to *eq.*2.39, the local shear rate increases linearly along the radius.

$$\dot{\gamma}(r) = \frac{v_\theta(r)}{h} = \frac{r\Omega}{h} \tag{2.39}$$

As in the case of cup and bob geometries and given in *eq.*2.40, only the mean value of the shear stress can be deduced from the torque Γ applied to the geometry.

$$\langle \sigma \rangle = \frac{3\Gamma}{2\pi R^3} \tag{2.40}$$

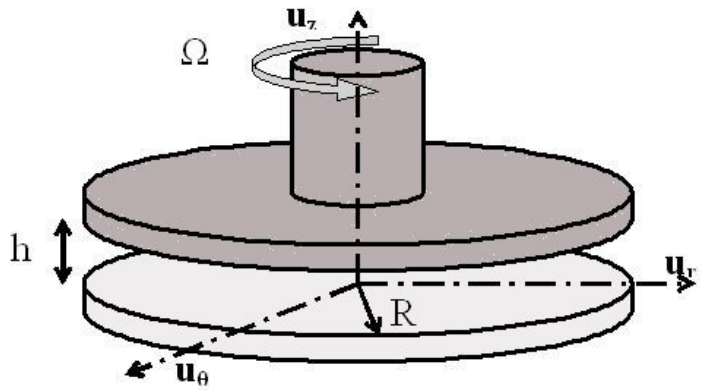

Figure 2.6: Parallel plates geometry

Since the contribution of the sheared sample to the torque applied to the plate is maximum at the rim of the geometry, the apparent shear viscosity measured with such shear cells is defined as follows:

$$\eta_{app} = \frac{\langle \sigma \rangle}{\dot{\gamma}_{r=R}} \tag{2.41}$$

2.4.2 Methodology

Creep Tests and Step Rate Tests

Commercially available rheometers such as those used in this piece of research are designed so that the operator can choose between different functioning modes to characterize the rheological properties of a given sample. As long as these properties rapidly reach steady values or do not evolve in time, the available experimental procedures are relatively straightforward. Indeed the typical curve

$\sigma = f(\dot{\gamma})$ and then the sample viscosity can easily be obtained by *sweep tests* for which either the stress or the shear rate is controlled to increase or decrease while the other parameter, either the shear rate or shear stress is measured. Likewise, the dynamic procedure described above to determine the viscoelastic properties of a given material can be followed.

However, as shown in Fig.2.7(a) and Fig.2.7(b) for the systems studied in this work, some materials see their rheological properties evolve as a function of the time or their previous *shear history* or even with the time they have spent at rest. In such cases, that is if the existence of a steady state is not known *a priori*, the number of available experimental procedures reduces to two: *creep tests* and *step rate tests*. Creep tests are performed on stress controlled rheometers. A constant stress is applied to the investigated sample and the resulting deformation is monitored as function of time (see Fig.2.3 above). Step rate tests are equivalent to creep measurements but performed on a strain controlled rheometers. A constant shear rate is applied to the sample and the resulting stress is monitored (see Fig.2.7(b)).

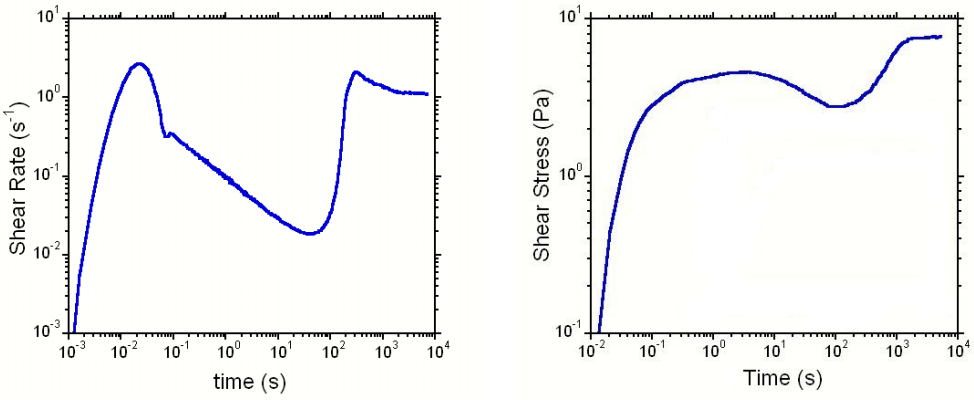

Figure 2.7: Typical temporal evolution of the shear rate (Fig.2.7(a)) and the shear stress (Fig.2.7(b)) within AOT (28.5$wt\%$) / Iso-octane (5$wt\%$) / water (66.5$wt\%$) self-assembling system.
$\sigma = 4Pa$ in Fig.2.7(a), $\dot{\gamma} = 2.5s^{-1}$ in Fig.2.7(b)

Both Fig.2.7(a) and Fig.2.7(b) show two regimes as a function of the shearing time. The first one during which either the shear rate in Fig.2.7(a) or the shear stress in Fig.2.7(b) evolve with the time is the *transient regime* and lasts almost $1000s$. Following the transient regime, both shear rate and shear stress stabilize and enter in the *steady regime* for which the sample rheological properties does not depend anymore on its shear history. The emergence of this steady regime will have important consequences since it will allow us to define the *reference state* of the systems investigated in the following.

Inertial Coupling in Stress Controlled Measurements

Stress controlled measurements present many assets when compared to strain controlled ones when the flow properties of yield stress fluids are considered. Indeed, whereas strain controlled experiments can only give information on a flowing material (*i.e.* above the yield stress τ_y previously defined), stress controlled experiments, especially creep ones, constitute an efficient probe of the macroscopic behaviour of such fluids either in the solid-like stress regime ($\sigma_{12} \leq \tau_y$) or in the fluid-like stress regime ($\sigma_{12} \geq \tau_y$).

If one disable the inertia correction tool on a stress controlled rheometer, imposing a stress step as in creep flow experiments will lead to free oscillations of the monitored strain response. These oscillations result from the inertial coupling between the moving geometry and the investigated sample as described in the equation 2.42 governing the motion of the rotating geometry [12, 31, 32]. In the latter, I is the inertia momentum of the rotating fixture, θ its angular displacement, Γ_{app} the torque applied by the rheometer and Γ_s the torque felt by the sample.

$$I \frac{\partial^2 \theta}{\partial t^2} = \Gamma_{app} - \Gamma_s \tag{2.42}$$

Defining $\alpha = I \frac{F_\gamma}{F_\sigma}$, F_γ and F_σ being the geometrical factors defined in the previous section linking the strain to the angular displacement and the stress to the

torque respectively, equation 2.42 can be written again as a function of mesoscopic instead of macroscopic physical quantities as follows:

$$\alpha \frac{\partial^2 \gamma}{\partial t^2} = \sigma_{app} - \sigma_s \tag{2.43}$$

Assuming that the sample behaviour is governed by a known given constitutive equation, it becomes possible to resolve the differential equation 2.43 as a function of the applied stress and therefore to get informative data on the sample behavior at both small and large level of strain once fitting experimental data to the model.

A particularly interesting model in this study is the Maxwell-Jeffrey model of which an analogical diagram in term of spring and dashpot is shown in Fig.2.8. Indeed, in the limit $\eta_2 >> 0$ it corresponds to the Kelvin-Voight model of viscoelastic solid materials while for $\eta_1 << 0$ it corresponds to the Maxwell model of viscoelastic fluids. As a consequence, it allows to take into account both 'solid-like' and 'fluid-like' behaviours depending if η_2 or η_1 tend either to high or low values respectively.

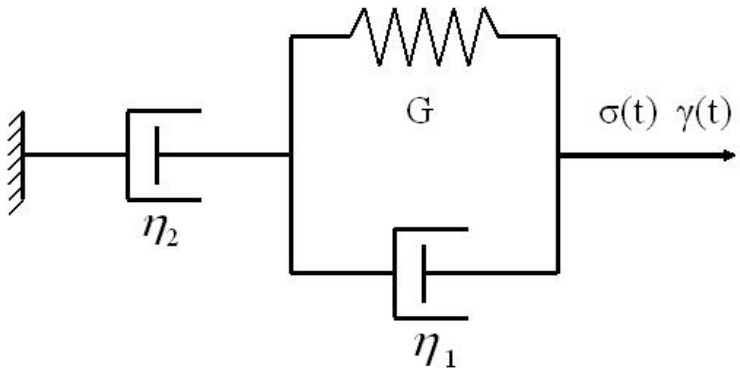

Figure 2.8: Analogical diagram of the Maxwell-Jeffrey model

The shear component of the constitutive equation of such materials is given by the relation 2.45 one can easily obtained considering the relations 2.44 existing between the stress $\sigma(t)$, the global strain $\gamma(t)$ and $\gamma_1(t)$ and $\gamma_2(t)$ the strains of

each stage respectively.

$$\begin{cases} \sigma(t) = G\gamma_1(t) + \eta_1\dot{\gamma}_1(t) = \eta_2\dot{\gamma}_2(t) \\ \gamma(t) = \gamma_1(t) + \gamma_2(t) \end{cases} \tag{2.44}$$

$$\eta_2\left(G\dot{\gamma} + \eta_1\ddot{\gamma}\right) = G\sigma + \left(\eta_1 + \eta 2\right)\dot{\sigma} \tag{2.45}$$

To illustrate the previous statement and anticipating on the following sections,

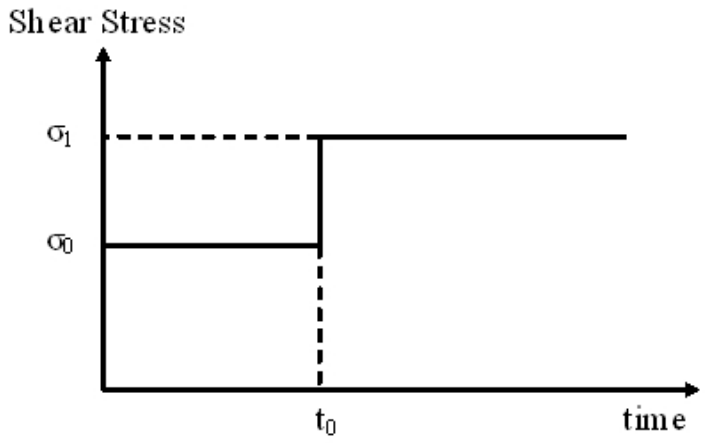

Figure 2.9: Applied stress step in a creep flow measurement

let us resolve the differential equation considering a Maxwell-Jeffrey fluid being submitted to a stress step as displayed in Fig.7.2 so that $\sigma_{app}(t)$ is given by the following expression where $h(t)$ is the step function equal to 0 for $t \leq 0$ and 1 for $t \geq 0$ and $\Delta\sigma = \sigma_1 - \sigma_0$. σ_0 can be considered here as a reference stress which is applied to the sample long enough for a steady state to be reached.

$$\sigma_{app}(t) = \sigma_0\, h(t) + \Delta\sigma\, h(t - t_0) \tag{2.46}$$

Using the constitutive equation 2.45 of Maxwell-Jeffrey fluids and the motion equation 2.43, the differential equation one wants to resolve becomes:

$$\alpha\left(\eta_1+\eta_2\right)\frac{\partial^3\gamma}{\partial t^3}+\left(G\alpha+\eta_1\eta_2\right)\frac{\partial^2\gamma}{\partial t^2}+\eta_2 G\frac{\partial\gamma}{\partial t}=\left(\eta_1+\eta_2\right)\frac{\partial\sigma_{app}}{\partial t}+G\sigma_{app} \tag{2.47}$$

Replacing σ_{app} by its expression 2.46 and using Laplace transforms defined as follows with $F(p)$ being the Laplace transform of $f(t)$:

$$F\left(p\right)=L\left\{f\left(t\right)\right\}=\int_0^\infty e^{-pt}f(t)dt \tag{2.48}$$

the resolution of the differential equation governing $\gamma(t)$ amounts to find the inverse Laplace transform of the following expression of $\Gamma(p)=L\{\gamma(t)\}$. This is done by expending each term of the next equation 2.49 in partial fractions so that simple and known Laplace transforms can be recognized.

$$\begin{aligned}\Gamma(p)= \quad & \Delta\sigma\left[\frac{\left[\left(\eta_1+\eta_2\right)+\frac{G}{p}\right]e^{-t_0p}}{\alpha\left(\eta_1+\eta_2\right)p^3+\left(G\alpha+\eta_1\eta_2\right)p^2+\eta_2Gp}\right]\\ & +\sigma_0\left[\frac{G}{p\left[\alpha\left(\eta_1+\eta_2\right)p^3+\left(G\alpha+\eta_1\eta_2\right)p^2+\eta_2Gp\right]}\right]\\ & +\dot{\gamma_0}\left[\frac{\left[p\alpha\left(\eta_1+\eta_2\right)+\left(G\alpha+\eta_1\eta_2\right)\right]}{\alpha\left(\eta_1+\eta_2\right)p^3+\left(G\alpha+\eta_1\eta_2\right)p^2+\eta_2Gp}\right]\end{aligned} \tag{2.49}$$

The final expression 7.1 of $\gamma(t)$ is then determined as a function of the Maxwell-Jeffrey parameters G, η_1, η_2, the applied stress step magnitude $\Delta\sigma$ and σ_0 and $\dot{\gamma_0}$ the reference stress and its corresponding shear rate in the steady regime.

$$\begin{aligned}\gamma(t) = \quad & \Delta\sigma\left[\beta h(t') + \frac{t'}{\eta_2}h(t') + e^{-\lambda t'}\left[\beta cos(\omega t') + \frac{1}{\omega}\left(\lambda\beta - \frac{1}{\eta_2}\right)sin(\omega t')\right]\right] \\ & + \sigma_0\left[\frac{-2\lambda}{B\eta_2} + \frac{t}{\eta_2} + e^{-\lambda t}\left[\frac{1}{B\omega\eta_2}\left(\lambda^2 - \omega^2\right)sin(\omega t) + \frac{2\lambda}{B\eta_2}cos(\omega t)\right]\right] \\ & + \dot{\gamma_0}\left[\frac{2\lambda}{B} + e^{-\lambda t}\left[\frac{1}{\omega}\left(1 - \frac{2\lambda^2}{B}\right)sin(\omega t) - \frac{2\lambda}{B}cos(\omega t)\right]\right]\end{aligned} \tag{2.50}$$

where $t' = t - t_0$, $B = \dfrac{\eta_2 G}{\alpha\left(\eta_1 + \eta_2\right)}$, $\lambda = \dfrac{G\alpha + \eta_1\eta_2}{2\alpha\left(\eta_1 + \eta_2\right)}$, $\omega = \sqrt{B - \lambda^2}$ and $\beta = \dfrac{1}{B}\left(\dfrac{1}{\alpha} - \dfrac{-2\lambda}{\eta_2}\right)$.

At last, given that experimental data can be fitted to the theoretical model (*i.e.* the investigated materials behaves as Maxwell-Jeffrey fluid at least in a certain extent), the free oscillations of the strain one can observe at the inception of each stress step of a creep experiment allow to determine its viscoelastic properties.

2.5 Conclusion

In this chapter we aimed to introduce basic notions concerning the flowing properties of complex fluids. In a first section we have introduced some basic notions in rheology such as the *rate of deformation* or the *stress* tensor. In a second section we have focused on the presentation of some of the non-newtonian behaviors encountered in this piece of research.

This succinct overview of the theoretical background used in this study is followed by an overview of the available experimental devices and techniques used in rheometry. In this last section, we have presented first the devices used in what follows, namely strain and stress controlled shear rheometers together with their different shear cell geometries. Then, we have introduced the different experi-

mental methods we have used to probe the rheological properties of our samples.

As mentioned in this chapter and later in this study, one important parameter in the characterization of the rheological properties of a given material is its internal structures. Usual rheometry techniques are excellent tools for the characterization of the relation between stress and deformation within a given material. Nonetheless, they do not bring any information concerning its structural properties. As a consequence, other experimental techniques allowing to probe the internal structures of the sample have to be envisioned. Such experimental techniques, notably birefringence texture analysis, X-ray scattering and freeze fracture electron microscopy are introduced in the following chapter together with the different experimental setups with which they have been applied in this piece of research.

References

[1] G.H. McKinley. *Extensional Flow and Instabilities of Elastic Polymer Solutions*. ICL Press, London, 1997.

[2] P. Lindner and T. Zemb. *Neutron, X-Ray and Light: Scattering Methods Applied to Soft Condensed Matter*. Elsevier Science, 2002.

[3] G.G. Fuller. Optical rheometry. *Annual Review of Fluid Mechanic*, 22:387 – 417, 1990.

[4] C.W. Macosko. *Rheology: principles, measurements and applications*. New York Press, 1993.

[5] R.G. Larson. *The structure and rheology of complex fluids*. topics in chemical engineering. Oxford University Press, New York, 1999.

[6] P. Moldenaers and J. Mewis. Transient behavior of liquid crystalline solutions of poly(benzylglutamate). *Journal of Rheology*, 30(3):567–584, 1986.

[7] O. Diat, D. Roux, and F. Nallet. Effect of shear on a lyotropic lamellar phase. *Journal de Physique II France*, 3:1427–1452, 1993.

[8] P. Oswald. *Rhéophysique - Ou comment coule la matière*. Belin, 2006.

[9] P. Panizza, A. Colin, C. Coulon, and D. Roux. a dynamic study of onion phases under shear flow: size changes. *European Physics Journal B*, 4:65–74, 1998.

[10] L. Courbin and P. Panizza. Shear-induced formation of vesicles in membrane phases: Kinetics and sizeselection mechanisms, elasticity versus surface tension. *Physical Review E*, 69(2):021504(1) – 021504(12), 2004.

[11] M. Kotlarchyk, E.Y. Sheu, and M.Capel. Structural and dynamical transformations between neighboring dense microemulsion phases. *Physical Review A*, 46(2):928–939, 1992.

[12] P. Coussot, H. Tabuteau, X. Chateau, L. Tocquer, and G. Ovarlez. Aging and solid or liquid behavior in pastes. *Journal of Rheology*, 50(6):975–994, 2006.

[13] C. Derec, G. Ducouret, A.Adjari, and F. Lequeux. Aging and nonlinear rheology in suspensions of polyethylene oxyde-protectedsilica particles. *Physical Review E*, 67, 2003.

[14] L. Cipelletti, S. Manley, R.C. Ball, and D.A. Weitz. Universal aging features in the restructuring of fractal colloidal gels. *Physical review Letters*, 84(10):2275 – 2278, 2000.

[15] M. Cloitre, R. Borrega, and L. Leibler. Rheological aging and rejuvenation in microgel pastes. *Physical Review Letters*, 85(22):4819–4822, 2000.

[16] J. Mougel, O. Alvarez, C. Baravian, F. Caton, P. Marchal andM J. Stebe, and L.Choplin. Aging of an unstable w/o gel emulsion with a nonionic surfactant. *Rheologica Acta*, 45:555–560, 2006.

[17] P. Moldenaers, G. Fuller, and J. Mewis. Mechanical and optical rheometry of polymer liquid-crystal domain structure. *Macromolecules*, 22:960–965, 1989.

[18] R.G. Larson. Arrested tumbling in shearing flows of liquid crystal polymers. *Macromolecules*, 23:3983–3992, 1990.

[19] J. Mewis, M. Mortier, J. Vermant, and P. Moldenaers. Experimental evidence for the existence of a wagging regime in polymericliquid crystals. *Macromolecules*, 30:1323–1328, 1997.

[20] J-Y. Lee, J.J. Magda, H. Hu, and R.G. Larson. Cone angle effects, radial pressure profile, and second normal stress differencefor shear-thickening wormlike micelles. *Journal of Rheology*, 46:195–208, 2002.

[21] I. Wunderlich, H. Hoffman, and H. Rehage. Flow birefringence and rheological measurements on shear induced micellar structures. *Rheologica Acta*, 26:532–542, 1987.

[22] J-F. Berret, J. Appel, and G. Porte. Linear rheology of entangled wormlike micelles. *Langmuir*, 9:2851–2854, 1993.

[23] J-F. Berret, D.C. Roux, and P. Lindner. Structure and rheology of concentrated wormlike micelles at the shear-induced isotropic-to-nematic transition. *The european physical journal B*, 5:67–77, 1998.

[24] H.A. Barnes. Thixotropy - a review. *Journal of Non-Newtonian Fluid Mechanic*, 70:1–33, 1997.

[25] R.G. Larson and D.W. Mead. Development of orientation and texture during shearing of liquid-crystalline polymers. *Liquid crystals*, 12(5):751–768, 1992.

[26] D.C. Roux, J-F. Berret, G. Porte, E. Peuvrel-Disdier, and P. Lindner. Shear-induced orientations and textures of nematic wormlike. *Marcomolecules*, 28:1681–1687, 1995.

[27] F. Caton and C. Baravian. Plastic behavior of some yield stress fluids: from creep to long time yield. *Rheologica Acta*, 47:601–607, 2008.

[28] H.A Barnes. The yiels stress - a review or " -everything flows? *Journal of Non-Newtonian Fluid Mechanic*, 81:133–178, 1999.

[29] H. Nechad, A Helmstetter, R. El Guerjouma, and D. Sornette. Creep ruptures in heterogeneous materials. *Physical Review Letters*, 94:045501(1) – 045501(4), 2005.

[30] C. Kittel. *Physique de l'état solide*. Dunod, Paris, 2007.

[31] R. Roscoe. Free damped oscillations in viscoelastic materials. *Britanical Journal of Applied Physics (J. Phys. D)*, 2(2):1261 – 1266, 1969.

[32] C. Baravian and D. Quemada. Using instrumental inertia in controlled stress rheometry. *Rheologica Acta*, 37:223–233, 1998.

Chapter 3

Structural Characterizations

Contents

Résumé du Chapitre 3

Dans ce troisième chapitre nous nous intéressons aux méthodes expérimentales utilisées dans cette étude pour caractériser la structure des phase lamellaires lyotropes. Celles-ci sont au nombre de trois et permettent de caractériser les propriétés structurelles à différentes échelles allant du nanomètre au milimètre.

Dans la première partie de ce chapitre nous introduisons les connaissance de base concernant la propagation de la lumière polarisée dans les milieux optiquement anisotrope, biréfringent. nous présentons ensuite le montage expérimental que nous avons utilisé dans cette étude pour visualiser la texture de nos échantillons à l'échelle microscopique.

La seconde partie de ce chapitre introduis les notions de bases relatives à la diffusion de rayons X au sein de matériaux de structures nanoscopiques. De même que dans le cas des expériences de biréfringence, nous présentons ensuite le dispositif expérimental utilisé pour réaliser nos experiences de diffusion des rayons X sur des échantillons cisaillés.

Enfin, nous complétons ce descriptif des méthodes expérimentales utilisées par la technique de microscopie électronique en transmission de cryofracture. Cette technique invasives permet une visualisation direct d'empreintes de fractures à l'échelle nanoscopique si bien que les résultats relatifs à ces observations peuvent être confrontés à ceux obtenus en diffusion des rayons X.

3.1 Introduction

As mentioned in the previous chapters, the internal structures formed in ternary self-assembling systems and their interactions lead to the formation of lyotropic liquid crystal phases. In our attempt to understand the rheological behaviour of such materials, the characterization of their structural properties in equilibrium as in flow is necessary. This has been achieved after three different experimental techniques, namely, birefringence textures analysis, X-ray scattering, freeze fracture Transmission Electron Microscopy and cryo-TEM.

Both birefringence and X-ray scattering are based on the interaction of an electromagnetic wave such as light or X-Ray with the structures formed in our samples. However the physical phenomena on which they are based are different. Indeed, birefringence affects the polarization of the light passing through optically anisotropic materials. On the other hand, X-ray scattering is based on the analysis of the scattering spectrum resulting from the interaction of X-rays with the structures formed in the sample. Both techniques present the asset of being non-invasive. Consequently, they can be coupled to flow measurements so that the rheological behaviour of the tested material can be related to its structural evolution at the microscopic scale (X-ray scattering) as at the mesoscopic scale (birefringence).

In cryo-TEM, the sample is not directly observed. Indeed only the replicas of a fractured sample are observed. Nonetheless, the method constitutes an excellent way of confirming or infirming the results obtained using either birefringence or X-ray scattering.

In this study, X-ray scattering and cryo-TEM were not performed in our laboratories. X-ray scattering experiments were performed at the *European Synchrotron Radiation Facility* on the french beam line D2AM in collaboration with Cyrille Rochas. As for cryofracture TEM, the cryofractures replicas were prepared at the *centre technologique des microstructures (CTμ - Université Claude*

Bernard - Lyon I) with Annie Rivoire and observed in TEM at the *Centre de Recherche sur les Macromolecules Végetales (CERMAV - UPR5301)* in collaboration with Isabelle Pignot-Paintrand.

In the first section of this chapter, we will describe the birefringence phenomenon from a theoretical point of view and the experimental setup especially designed for our observations at the *Laboratoire de Rhéologie*. In a second section we will succinctly describe the two other experimental techniques we have used in collaboration with specialists of microscopy and X-ray scattering. The parallel plate shear cell used in these birefringence and X-ray scattering experiments had previously been designed at the 'Laboratoire de Rhéologie' []. It allows for the control of the gap separating the plates and the angular velocity of the rotating plate.

3.2 Birefringence and Experimental Setup

Some materials such as lyotropic liquid crystals are optically anisotropic [1]. That is, their optical properties are not the same in all the directions of space. Two phenomena are related to such an anisotropy: the dichroism and the birefringence. Whereas, the dichroism involves adsorption of the light propagating in a media, the birefringence concerns changes in its polarization. We will only consider the birefringence phenomena here. In birefringent media the refraction tensor $\mathbf{n}$ is not isotropic so that the propagation speed of a light beam depends on its polarization direction [2].

3.2.1 Theoretical Background

Let us consider the propagation of a monochromatic and initially linearly polarized light wave in an uniaxial birefringent material with e being its thickness and its optical axis being oriented along the direction $0x$ as shown in Fig.3.1. In such conditions the refraction tensor is given by eq.3.1 where n_e is the extraordinary

index of the material along Ox and n_o the ordinary index along the perpendicular direction, Oy. The difference $n_e - n_o = \Delta n$ is the intrinsic birefringence of the material. Besides Ox and Oy are called the fast and slow axis respectively.

$$\mathbf{n} = \begin{pmatrix} n_e & 0 \\ 0 & n_o \end{pmatrix} \tag{3.1}$$

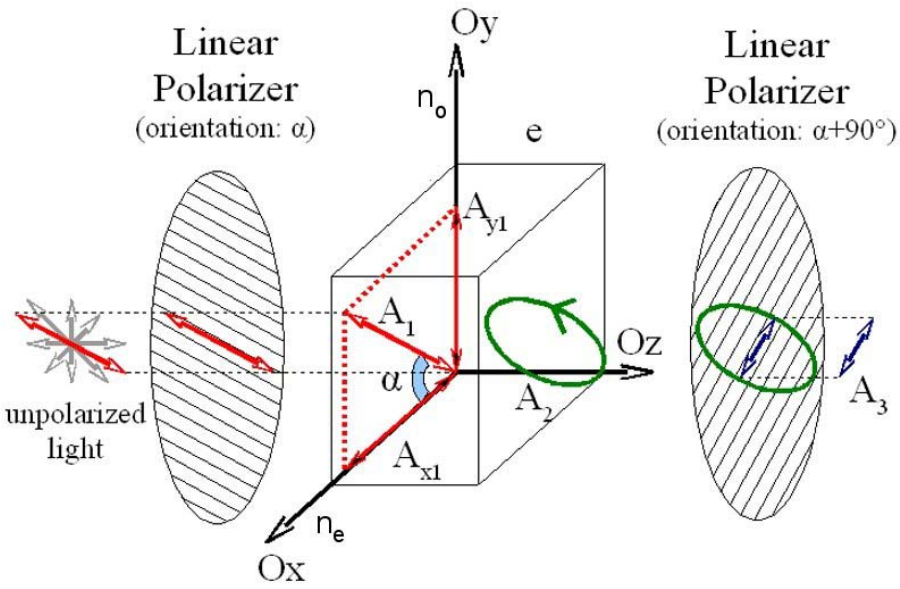

Figure 3.1: Plane linearly polarized light propagating in an uniaxial birefringent material.

As mentioned above the incident plane light wave is linearly polarized by passing through a linear polarizer , the components A_{x1} along Ox and A_{y1} along Oy of $\vec{A}(\vec{z},t)$ are then given by equation 3.2.

$$\begin{aligned} A_{x1} &= A_0.cos(\alpha)\,cos(\omega t) \\ A_{y1} &= A_0.sin(\alpha)\,cos(\omega t) \end{aligned} \tag{3.2}$$

Within the material, the optical path traveled by A_{x1} is $n_e.e$ while the optical path traveled by A_{y1} is $n_o.e$. Thence, the components of the light wave coming out from the sample, A_{x2} and A_{y2}, become:

$$\begin{aligned} A_{x2} &= A_0.cos(\alpha)\, cos\left(\omega t - \frac{2\pi n_e e}{\lambda}\right) \\ A_{y2} &= A_0.sin(\alpha)\, cos\left(\omega t - \frac{2\pi n_o e}{\lambda}\right) \end{aligned} \tag{3.3}$$

Changing adequately the time origin, *eq.*3.3 can be written again as follows:

$$\begin{aligned} A_{x2} &= A_0.cos(\alpha)\, cos\left(\omega t - \frac{2\pi \Delta n.e}{\lambda}\right) \\ A_{y2} &= A_0.sin(\alpha)\, cos(\omega t) \end{aligned} \tag{3.4}$$

Thereby, the polarization state of the light wave coming out from a birefringent material depend on the values of $\phi = \frac{2\pi \Delta n.e}{\lambda}$. For $\phi = \pm\frac{\pi}{2}$, $\vec{A}_2(z = e, t)$ maps out a circle of radius A_0. The electric wave is then circularly polarized, depending if the electric vector $\vec{A}_2$ precesses clockwise ($\phi = +\frac{\pi}{2}$) or counterclockwise ($\phi = -\frac{\pi}{2}$) the light wave is said to be right or left circularly polarized respectively. For $0 < \phi < \frac{\pi}{2}$, the electric wave maps out an ellipse as shown in Fig.3.1 and the polarization is said to be elliptic.

If one places an analyzer as shown in Fig.3.1 behind the birefringent material, the components of the transmitted electric waves $\vec{A}_3$ becomes:

$$\begin{aligned} A_{x3} &= A_0.cos(\alpha)\, cos\left(\alpha + \frac{\pi}{2}\right) cos\left(\omega t - \frac{2\pi \Delta n.e}{\lambda}\right) \\ A_{y3} &= A_0.sin(\alpha)\, sin\left(\alpha + \frac{\pi}{2}\right) cos(\omega t) \end{aligned} \tag{3.5}$$

The light intensity $I = \left\langle (A_{x3} + A_{y3})^2 \right\rangle_t$ to which photosensitive captors are sensitive is then given by equation 3.6.

$$I = I_0.sin^2(2\alpha)\, sin^2\left(\frac{\pi \Delta n.e}{\lambda}\right) \tag{3.6}$$

Thence, if the linear polarizer and the analyzer have the same orientation than the slow and fast optical axis of the birefringent material, that is if $\alpha = 0$ or $\alpha = \frac{\pi}{2}$, the light intensity becomes null and the sample appears to be dark. On the other hand if α differs from 0 or $\frac{\pi}{2}$, the light wave passes through the system and the sample appears bright.

Besides, if $\phi = 0\,[2\pi]$, that is either if the sample is optically isotropic ($\Delta n = 0$) or if the sample thickness is a multiple of $\frac{2\lambda}{\Delta n}$, the light intensity becomes null as well and the sample of Fig.3.1 will appear dark as well.

Thence, to distinguish if a dark domain is either due to an alignment of its local fast and slow optical axis with the polarization directions of the polarizer and the analyzer or to the local birefringence, one can simultaneously rotate the polarizer and the analyzer [3–6]. If the dark domains observed initially remain dark this means that the sample is locally optically isotropic. On the other hand if the initially dark domains become bright and initially bright domains become dark as a function of the rotation angle, this corresponds to different local orientations of birefringent structures. In the latter case, the dark domains correspond to the regions of identical orientation also called isoclines.

Two typical birefringence patterns of the lamellar phases studied in this work are shown in Fig.3.2. These are obtained by observing the sample between two crossed linear polarizers either at rest or when submitted to shear between two parallel plates. Whereas at rest the sample exhibits randomly oriented bright and dark domains (see Fig.3.2a), when sheared the domains orient themselves on the velocity direction (see Fig.3.2b). Thereby, the dark region form a dark cross

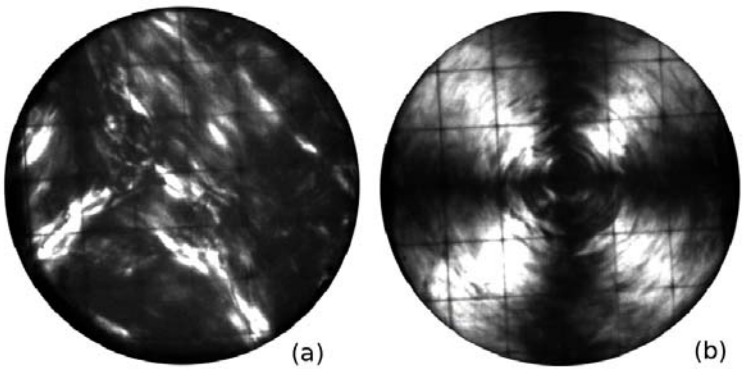

Figure 3.2: Typical birefringent patterns obtained by observing the sample between two crossed linear polarizers. (a) the sample is at rest after being loaded in a parallel plate device - (b) the sample has been sheared for 60s.

of which the directions are aligned on the polarization directions of the crossed polarizers. These dark regions correspond to isoclines for which the local fast and slow axis of the sample are aligned with the polarization directions. However the bright regions of Fig.3.2b, show dark thin domains coexisting with bright domains. This correspond to local topological defects within the structural organization.

Since all our preliminary birefringent observations have indicated that the structures formed in our samples aligned on the velocity field when sheared, the isocline pattern does not present a peculiar interest in this piece of research. Conversely, the birefringence textures corresponding to variation of the local orientation of the structures within the sample can bring us important information concerning the local organization of the structures within the sample.

3.2.2 Experimental Setup

As mentioned above, some liquid crystals and notably defects rich lamellar phases as those studied in this piece of research are locally anisotropic media. Indeed, in such phases the orientation of the lamellar structures is not the same in all

the directions of space. Instead mesoscopic to macroscopic domains of favored orientation separated by defects regions are formed. This local inhomogeneities results in complex isoclines networks which makes it difficult to interpret the birefringence patterns obtained solely with crossed linear polarizers (see Fig.3.2a).

To circumvent the predominant effects of the polarizer and analyzer orientations one can use circularly polarized light instead of linearly polarized light [3]. Indeed, using circularly polarized light is equivalent to simultaneously rotate both polarizer and analyzer at such a speed that the isoclines are 'moving' too fast to be detected by the captor (human eyes or camera). It is then possible to obtain birefringence textures which are characteristic of the structures formed within the sample and their local mesoscopic organization [3, 4, 7–9].

Using circularly polarized white light, the birefringence patterns show coloured domains. The colour of a given domain corresponds to the local retardance, $\Delta n.e$ induced by the birefringent structures which can be compared to the Newton color sequence of fig.3.3. The appearance of colours while using a white light source can be easily explained if one considers *eq.*3.6.

Indeed, white light is compounded by light waves of various wavelengths. Thence, while a given value of the retardance induces a decrease of the light intensity at a given wavelength it does not for other wavelengths. As a consequence, when a given wavelength (colour) is 'extinguished' other wavelengths are not so that the perceived colour is the complementary of the extinguished colour.

The experimental setup used in our birefringence observations is described in Fig.3.4. A parallel white light is sent toward a linear polarizer of which the polarization direction is taken as a reference. The linearly polarized light wave coming out from this polarizer pass through a quarter wave plates of which the fast optical axis is oriented at −45. The circularly polarized electric wave obtained that way, passes through the sample which is loaded in a transparent parallel plate shear cell of which the angular velocity is controlled. The resulting light wave is

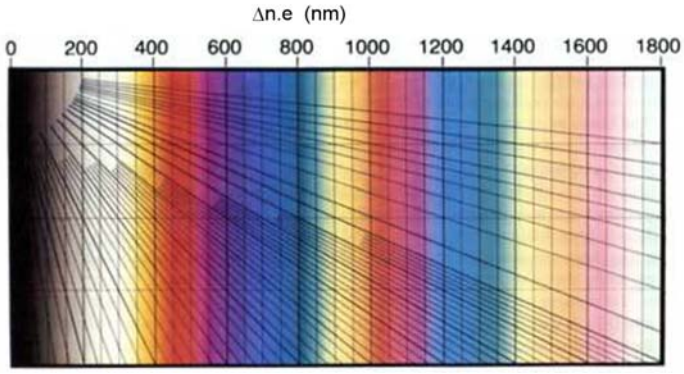

Figure 3.3: Newton colour sequence showing the colours produced by a birefringent sample illuminated by white light as its retardance is increased [1]

then analyzed through a second quarter wave plate having its fast axis oriented at +45 and a linear polarizer oriented at 90. The resulting birefringence texture patterns are recorded by a camera which is either equipped with a microscope lens or a wide angle lens. This allows to collect either refine images of the textures at the local scale or global birefringence patterns within the shear cells.

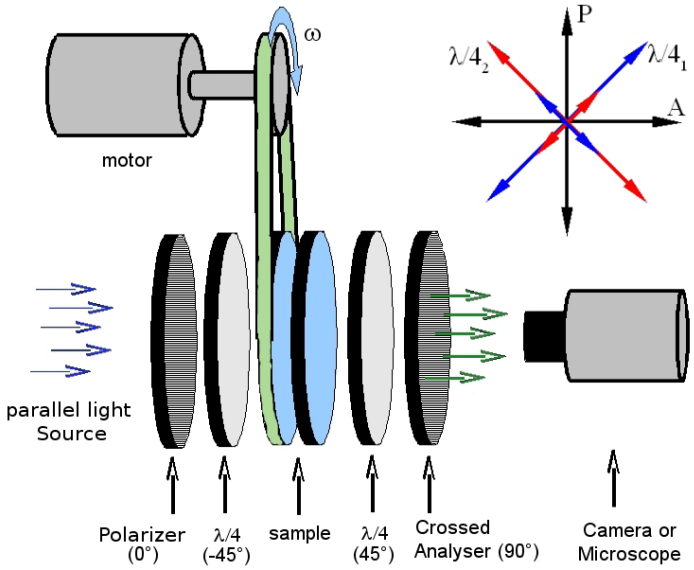

Figure 3.4: Experimental setup for the visualization of birefringent textures in shear.

3.3 Other Experimental Techniques

In the above section, we have introduce the birefringence phenomena which results in the emergence of textures at the mesoscopic length scale when observing a given liquid crystalline sample with crossed polarized light. These typical textures and their evolution in flow bring important information concerning the mesoscopic structural properties of the lyotropic liquid crystalline phases considered in this piece of research. However, one has to consider other experimental techniques in order to probe the sample at the microscopic length scale. In this study, X-ray scattering and cryofracture electron microscopy have been used. In the following paragraphs we will succinctly introduce both techniques.

3.3.1 X-Ray Scattering

Theoretical Background

As mentioned in the first chapter, electromagnetic radiations (X-ray, light or neutron) interact with matter. These interactions result in scattering events [10, 11]. Unlike in imaging techniques, a scattering experiment does not aim to reconstruct an image of the sample structures. Instead it aims at producing the interference pattern resulting from the interference between scattered waves within a sample. These interference patterns can then be transformed to reconstruct an image of the average correlations within the structure of a given material.

We restrict ourselves here to the coherent and static scattering. Let us first consider the scattering by a pair of particle as illustrated in Fig.3.5. In the static approximation the time dependence can be overlooked so that the complex amplitude of a plane incident wave, A_{in}, at a point $\vec{r}$ of space, can be reduced to *eq.*3.7 with $k = \frac{2\pi}{\lambda}$.

$$A_{in} = A_0.e^{(i\vec{k}_0.\vec{r})} \tag{3.7}$$

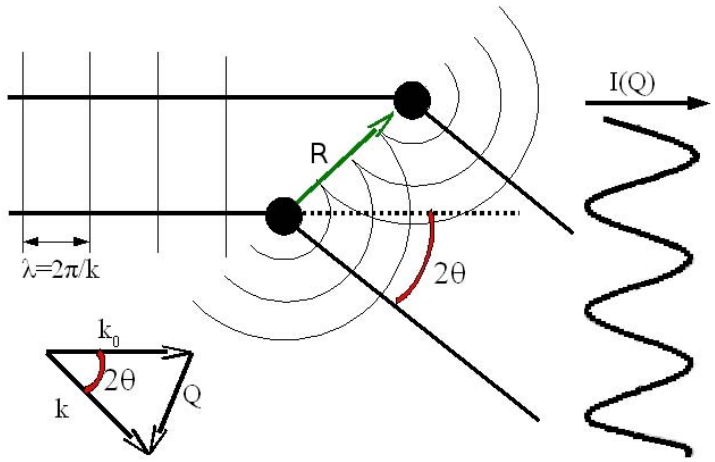

Figure 3.5: Interference between scattered waves from two point scatterers [10].

When interacting with an atom a part of the incident wave is scattered in all directions of space around the scattering centre so that the scattered amplitude in $\vec{r}$ is given by *eq.*3.8.

$$A_{sc} = \frac{A_0 b}{r} e^{i.\vec{k}_0.\vec{r}} \tag{3.8}$$

In the latter equation b is a *scattering length* which depends on the strength of the interaction between the particle and the electric wave. As shown in Fig.3.5, a wave scattered by a scatterer point at the position $\vec{R}$ from the origin in the direction $\vec{k}$ will be phase shifted in respect from the wave scattered in the same direction from a scatterer point located at the origin. The phase difference is given by the scalar products $\vec{Q}.\vec{R}$ where $\vec{Q} = \vec{k} - \vec{k}_0$ is the scattering vector. Its magnitude is given as a function of the scattering angle 2θ by $\left|\vec{Q}\right| = \frac{4\pi}{\lambda} sin\,\theta$.

Accordingly the amplitude of a wave scattered by a particle located in $\vec{R}$ in the direction 2θ is given by *eq.*3.9.

$$A_{sc} = \frac{A_0 b}{r} e^{i(\vec{k}_0.\vec{r} - \vec{Q}.\vec{R})} \tag{3.9}$$

Extending the above relation to very large number of particle scatterers, the total scattered amplitude of the electric wave within a piece of matter can be written again as follows:

$$A_{sc} = \frac{A_0}{r} e^{i\vec{k}_0.\vec{r}} \sum b_i e^{-i\vec{Q}.\vec{R}_i} \tag{3.10}$$

As for birefringence, the radiation captor used in X-ray scattering experiments is sensitive to the wave intensity, $I_{sc}(\vec{Q}) = \left\langle \left| A_{sc}(\vec{Q}) \right|^2 \right\rangle$ rather than the electric vector amplitude. The total scattered intensity can then be written as a function of the incident radiation intensity as follows:

$$I_{sc}(\vec{Q}) = \frac{I_{in}(\vec{Q})}{r^2} \sum b_i b_j e^{i\vec{Q}.(\vec{R}_j - \vec{R}_i)} \tag{3.11}$$

*Eq.*3.11 gives the significance of what is measured in an X-ray scattering experiments. Indeed the interference pattern, *ie.* the variations of the intensity as a function of $\vec{Q}$, corresponds to the probability of finding a particles of scattering length b_j and another one of scattering length b_i separated by a vector $\vec{r} = \vec{R}_j - \vec{R}_i$.

The condition to get constructive interference (high intensity) in the scattering pattern is obtained when the path difference between two scattered waves is a multiple of the wavelength, λ. This condition corresponds to the Bragg law given in *eq.*3.12.

$$2r.sin\,\theta = k\lambda \tag{3.12}$$

In the reciprocal space, the Bragg law defined above corresponds to the emergence of high intensity peaks or Bragg peaks in the scattering pattern for given $\vec{Q}$, that is when *eq.*3.13 is satisfied.

$$\left|\vec{Q}\right| = k\frac{2\pi}{r} \tag{3.13}$$

In an X-ray scattering experiment, one aims at deducing the structural properties of a material from the relative position and order of these Bragg peaks in the reciprocal space. This analysis relies on complex calculations and empirical

methods accounting for the nature of the point scatterers and their organization within the materials. Given the complex nature of the lyotropic phases investigated in this piece of research, such methods have not been considered yet at this stage of the study. However significant insights can be inferred solely from a qualitative analysis of the scattering patterns, notably concerning the local anisotropy of the samples either in equilibrium and in flow.

From an experimental point of view, X-ray scattering techniques allow to probe materials of which the characteristic distances between its constituent structural units range from ≈ 0.1 to $\approx 100nm$. These latter values correspond to scattering vectors ranging from ≈ 60 to $0.06nm^{-1}$. Since the radiation detector have a given size, the selection of the probed scattering vector range, is simply done by changing its distance from the sample. Whereas a close detector allows to probe small structures by collecting the scattered light at wide angles, positioning the detector at large distances from the sample allows to collect only the light scattered at small angles and therefore probe the structural properties of the sample at larger length scales.

In this piece of research we aimed to probe the local structures adopted by AOT surfactant molecules in lyotropic lamellar phases. As mentioned in the first chapter of this thesis, a characteristic size of such molecules is given by the length of the hydrocarbon chains constituting their hydrophobic part. For AOT molecules the length of these chains is approximatively $1.1nm$ [12]. As a consequence Wide Angle X-ray Scattering (WAXS) has been envisioned and used to probe our sample at typical length scales of $\approx 60nm$ and below. The results of these experiments will be introduced in the form of scattering patterns and discussed in the following sections of this manuscript.

Experimental Setup

As previously mentioned, the WAXS measurements have been performed on the beam line D2AM at the European Synchrotron Radiation Facility. In order to

probe the structures formed at 'equilibrium' and their shear induced evolution two different sample holders have been used. These are respectively capillary tubes or a polycarbonate parallel plates shear cell. It is to notice here that a mild shear of the sample could not be prevented during the filling up of both types of cells. Nonetheless, as shown later in this manuscript, the time length of the cell filling is much shorter than the time scale involved in the shear induced structural transformation of our samples. Consequently although the structures orientations might be affected by the filling process, the structures in itself is assumed to be relatively unchanged when compared to a sample at rest.

The experimental setup used to probe the shear induced structural evolution of the investigated phases is shown in Fig.3.6. In this setup, the parallel plates shear cell angular velocity is controlled. The two plates are made of polycarbonate to circumvent prohibitive adsorption of the X-ray beam when it passes through the shear cell. The whole systems is fixed on a translating plate. The translation is controlled so that the X-ray beam passes through either a high shear region close to the edge of the parallel plates or a low shear region close to the center of the shear cell (see $\dot{\gamma}_2$ and $\dot{\gamma}_1$ in Fig.3.6). The integration time is fixed to $10s$ and the scattering patterns are recorded repeatedly one position after the other.

3.3.2 Transmission Electron Microscopy

Unlike for birefringence and wide angle X-ray scattering, the samples observed in transmission electron microscopy have to be prepared according to the most appropriate method for a given sample. In this piece of research, transmission electron microscopy and the prior sample preparation were performed after two cryogenic techniques presented below.

In the first technique we have used, cryo-TEM, the sample is stretched so that it forms a thin layer within the apertures of a carbon grid. Once obtained these grids are immersed in liquid ethane so that the sample is frozen fast enough

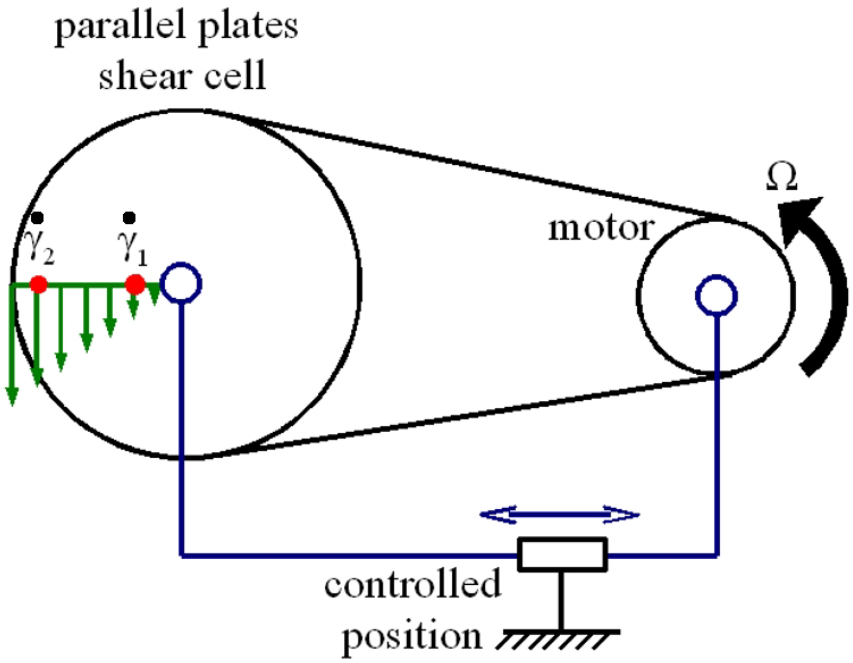

Figure 3.6: Experimental setup for in flow WAXS measurements

to circumvent the formation of crystalline ice. Once frozen the grid is placed on a refrigerated sample holder and observed in transmission electron microscopy at $120keV$. Although this first technique is relatively simple and straightforward, the lack of contrast in the microscopy photographs led us to envision Freeze Fracture Transmission Electron Microscopy which had already been used with success on lyotropic liquid crystals [7, 13, 14].

Indeed, this second technique appears to be a good alternative for the observation of liquid crystalline samples. Unlike in cryo-TEM, the sample is not observed directly in freeze fracture electron microscopy. Instead the replicas of freeze fractured samples are observed. These replicas are prepared after the following method.

The sample is loaded between two semi-hollow cups forming a sandwich. At first this sandwich, is plunged in pasty nitrogen ($T \approx 200C$). It is then loaded in a Reichert Jung cryofract in which it is opened. Both faces of the fractures are

then shaded with platinum at 45° before a carbon layer is deposited at normal incidence. The replicas are recovered at room temperature by specimen dissolution in iso-octane and in water, then collected onto a 600HH mesh grid prior to be observed in TEM at 120KV.

3.4 Conclusion

In this chapter we have introduced the different techniques used to characterize the structural properties of the lyotropic lamellar phases investigated in this piece of research. These are birefringence texture analysis, Wide angle X-ray scattering and Freeze Fracture and Cryogenic Transmission Electron Microscopy.

Such methods have allowed to characterize the structural properties of the investigated self-assembling systems either at equilibrium or during the shearing process.

Let us now introduce the different results we have obtained in the second part of this manuscript. In the following chapter we will present the preliminary results we got concerning the rheology of these systems. In a following chapter, we will show that the macroscopic behaviour of such systems are related to structural transitions at the mesoscopic and microscopic scales. At last the properties of the shear induced phases will be considered and characterized by means of rheometry techniques, in flow birefringence and wide angle X-ray scattering.

References

[1] R.G. Larson and D.W. Mead. Development of orientation and texture during shearing of liquid-crystalline polymers. *Liquid crystals*, 12(5):751–768, 1992.

[2] J. Drappier. *Plateaux de contrainte et bandes de cisaillement dans les fluides complexes.* PhD thesis, Université Paris VII, 2004.

[3] R. Duffait. *Expériences d'optique: Aggregation de Sciences Physisqueq*. Bréal, 1994.

[4] E. Cappelaere, J-F. Berret, J.P. Decrueppe, R. Cressely, and P.Lindner. Rheology, birefringence, and small-angle neutron scattering in a charged micellar system: evidence of a shear induced phase transition. *Physical Review E*, 56:1869–1878, 1997.

[5] E. Cappelaere. *Contribution rheologique et optique à l'etude experimentale de transitions induites par cisaillement dans des solutions micellaires*. PhD thesis, Université de Metz, 1996.

[6] C. Humbert. *Contribution à l'etude de la loi tensio-optique dans les solutions micellaires viscoélastiques*. PhD thesis, Université de Metz, 1998.

[7] B.A. Coldren, H.E. Warriner, R. Van zanten, J.A. Zasadzinski, and E.B Sirota. Lamellar gels and spontaneous vesicles in catanionic surfactant mixtures. *Langmuir*, 22:2465–2473, 2006.

[8] A. Leon, D. Bonn, J. Meunier, A. Al-Kahwaji, and O. Greffier andH. Kellay. Coupling between flow and structure for a lamellar surfactant phase. *Physical Review Letters*, 84:1335–1338, 2000.

[9] L. Courbin and P. Panizza. Shear-induced formation of vesicles in membrane phases: Kinetics and sizeselection mechanisms, elasticity versus surface tension. *Physical Review E*, 69(2):021504(1) – 021504(12), 2004.

[10] B Cabane. Small angle scattering methods. In *Surfactant Science series Vol.22*. Zana R., 1986.

[11] O. Glatter and O Kratky. *Small Angle X-Ray Scattering*. Academic Press, 1982.

[12] J. Bergenholtz and A. Romagnoli. Viscosity, microstructure and interparticle potential of aot/h2o/n-decaneinverse microemulsion. *Langmuir*, 11:1559–1570, 1995.

[13] H. Hoffmann, C. Thunig, U. Munkert, H.W. Meyer, and W. Richter. From vesicles to the l_3 (sponge) phase in alkyldeimethylamine oxide/heptanol systems. *Langmuir*, 8:2629–2638, 1992.

[14] J.I. Escalante, M. Gradzielski, H. Hoffmann, and K Mortensen. Shear-induced transition of originally undisturbed lamellar phase to vesicle phase. *Langmuir*, 16:8653 – 8663, 2000.

Part II

Results And Discussions

Chapter 4

Front Matter

Contents

Résumé du Chapitre 4

Dans ce quatrième chapitre, nous traitons des propriétés structurelles des système lyotropes lamellaires formés par l'AOT en présence d'eau et d'Iso-octane au repos. Pour ce faire nous travaillons sur des échantillons préparés le long d'une ligne de dilution en eau.

La première partie de ce chapitre est consacrée à la caractérisation des structures lamellaires formées par l'AOT, épaisseur de membrane et distances inter-membranaires, en fonction de la teneur en eau des différents échantillons considérés. Pour ce faire nous utilisons la technique de diffusion des rayons X au grands angles.

Dans la deuxième partie de ce chapitre, nous portons notre étude sur les propriétés de ces phases lamellaires à l'échelle microscopique. Pour ce faire nous utilisons la technique de microscopie en lumière polarisée. Cette technique permet de mettre en évidence la formation de défauts topologiques permanents pour les échantillons les plus dilués.

Nous montrons ensuite par des mesures simples de rhéométrie que l'emergence de ces défauts topologiques s'accompagne de comportements rhéologiques complexes. Ceux-ci seront l'objet d'une étude complète aux echelles nano-, micro- et macroscopiques dans les chapitres suivants.

4.1 Introduction

As mentioned in the first chapter of this manuscript, this study aims at characterizing the rheological properties of lamellar liquid crystalline phases formed by AOT, Iso-octane and water in the concentrated regime. However one needs first to characterize their structural properties at rest prior to consider their rheological properties.

In this chapter we will work on different liquid crystalline samples along the water dilution line shown in the AOT / Iso-octane / Water phase diagram of Fig.4.1 [1]. To do so, we will probe the structural properties of these samples as a function of their water content at the nanoscopic and microscopic scales using Wide Angle X-ray Scattering and circularly polarized light microscopy.

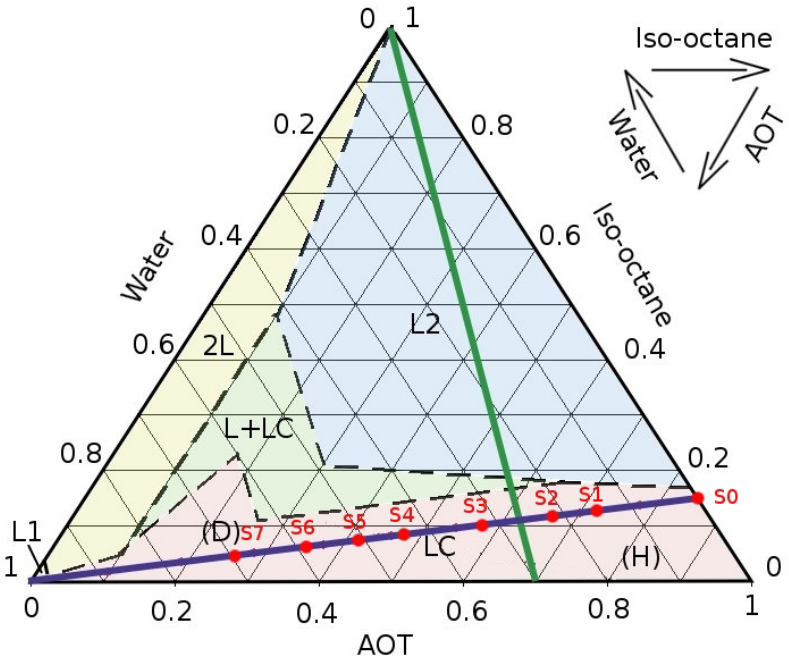

Figure 4.1: Samples composition along the considered water dilution line. Adapted from [1]

Finally, we will show that the various properties of the investigated lamellar phases at the microscopic scale come along with various rheological properties

ranging from Newtonian behaviour to strongly time and shear-history dependent viscoelastic behaviour. These complex rheological properties will be further investigated in the following chapters and discussed on the basis of previous studies of the literature on other lyotropic lamellar phases in the dilute regime [2–7].

4.2 Stuctural Properties along a Dilution Line

4.2.1 Interference Patterns in WAXS

As mentioned above, we have performed wide angle X-ray scattering experiments on samples with different compositions along the water dilution line of Fig.4.1. The samples $S0$ to $S7$ have been prepared following a standard dilution procedure of the mixture $S0$ of AOT ($85wt\%$) and Iso-octane ($15wt\%$). The samples have then been loaded in capillary tubes and placed in the sample holder of the D2AM beamline at the European Synchrotron Radiation Facility.

It can be noticed here that the loading procedure used to fill the capillary tubes involves the use of a syringe. Anticipating on what follows, the shear experienced by the samples during this process may have uncontrolled effects on their structural properties, especially for water rich samples.

The results of these WAXS experiments are reported in Fig.4.2 in the form of interference patterns together with the result obtained on a BeAg sample taken as reference. As expected considering the previous observations by Tamamushi and Watanabe [1], the interference patterns shown in Fig.4.2 indicate a complex transition with increasing water concentrations. Indeed, they show an evolution from an isotropic pattern for the sample $S0$ to highly anisotropic patterns corresponding to different liquid crystalline organization of the amphiphilic structures for samples $S1$ to $S7$.

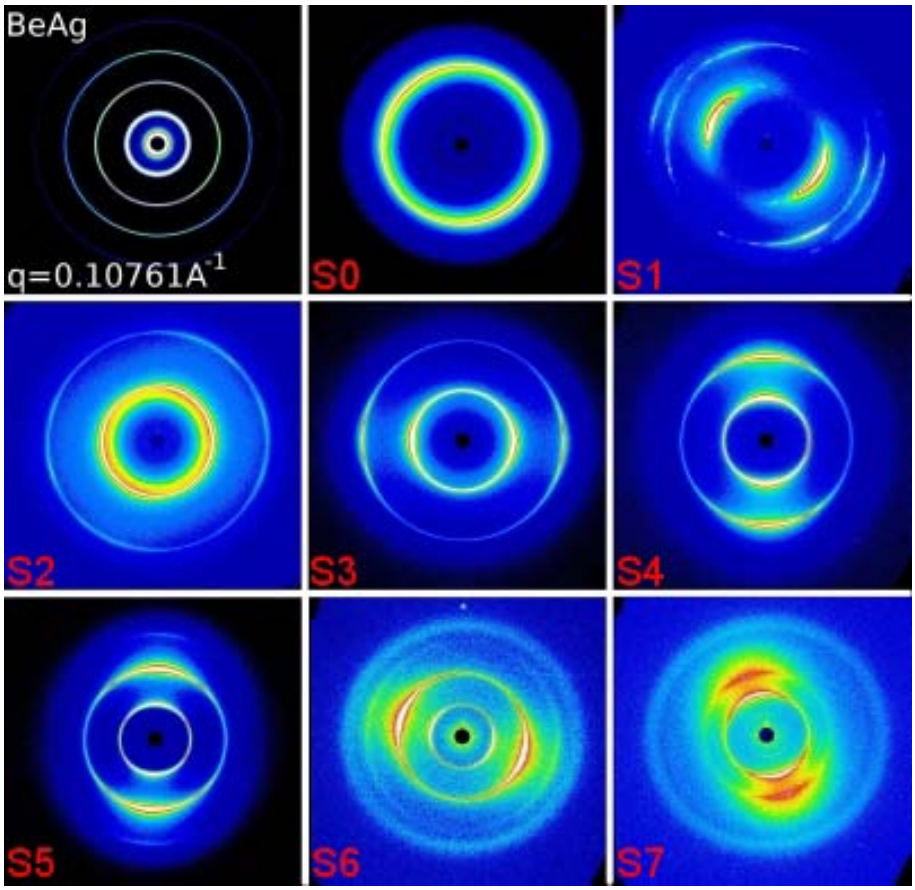

Figure 4.2: Interference patterns obtained on sample with various degree of water content along the previously considered dilution line (see Fig.4.1).

In this piece of work, we will restrict the analysis to the samples in which lamellar structures are formed. These are characterized by anisotropic interference patterns showing two peaks at characteristic scattering lengths q and $2q$. Such patterns correspond to those obtained on samples $S3$ to $S7$ in Fig.4.2. That is for sample with water concentration exceeding 30% in weight of sample.

4.2.2 Characteristic Sizes

Having identified the concentration range for which lamellar structures are formed, it is then possible to characterize them more precisely. To do so, we aim to determine the bilayer thickness δ and the interlamellar distance d as a function of

the membrane volume fraction ϕ (see Fig.4.3).

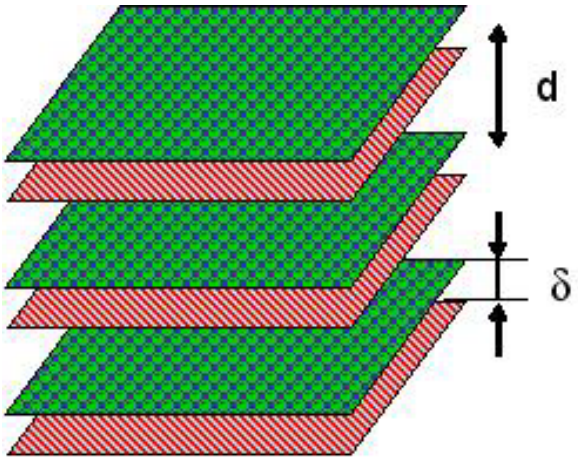

Figure 4.3: Schematic view of a bilayer structure with its two characteristic sizes: the interlamellar distance d and the bilayer thickness δ

Since we have followed a dilution line in water, the AOT to Iso-octane concentration ratio is kept constant in all investigated samples. In such conditions one might expect the bilayers thickness to be constant and the membrane volume fraction to be given by the AOT plus Iso-octane volume fraction as defined in Eq.4.1. In the latter m_{AOT}, m_{Iso} and m_{H2O} are the mass percentages of the sample in AOT, Iso-octane and water respectively and ρ_{AOT}, ρ_{Iso} and ρ_{H2O} their respective densities in the mixture.

$$\phi = \frac{\frac{m_{AOT}}{\rho_{AOT}} + \frac{m_{Iso}}{\rho_{Iso}}}{\frac{m_{AOT}}{\rho_{AOT}} + \frac{m_{Iso}}{\rho_{Iso}} + \frac{m_{H2O}}{\rho_{H2O}}} \tag{4.1}$$

Besides with increasing water contents, the interlamellar distance is expected to be related to δ and ϕ as given by Eq.4.2 [8].

$$d = \frac{\delta}{\phi} \tag{4.2}$$

The scattered intensity profiles along the favored direction of scattering for the different bilayers volume fractions considered in this study are reported in

Fig.4.4. They all show the typical features of lamellar phases with two scattering peaks at scattering length q and $2q$. The characteristic scattering lengths corresponding to the position of the two peaks gradually decrease with decreasing values of the bilayer volume fraction.

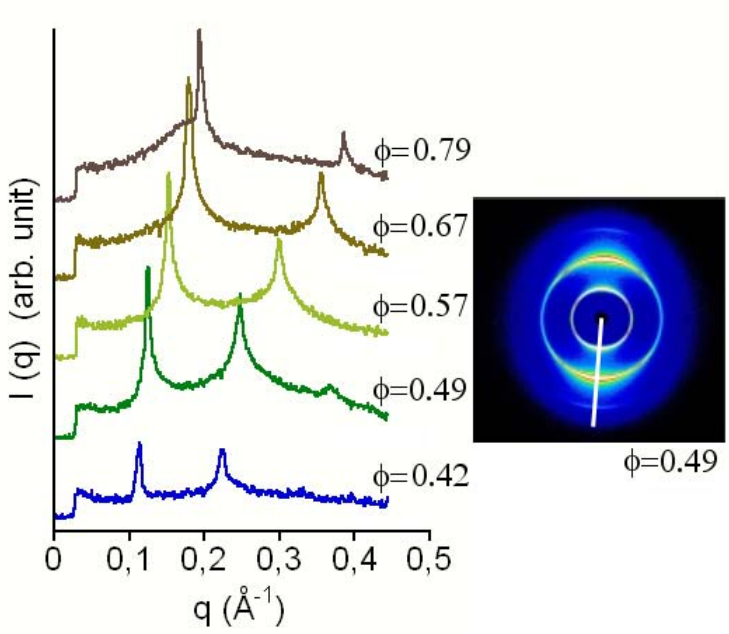

Figure 4.4: Scattered intensity profile along the favored direction of scattering (asshown on the interference pattern at the right hand side) for different values of the membrane volume fraction. The curves are shifted for clarity.

As shown in the third chapter, the interlamellar distances in each sample can be determined by Eq.4.3 from the values of the characteristic scattering lengths q obtained in Fig.4.4 [8].

$$d = \frac{2\pi}{q} \tag{4.3}$$

The values of the interlamellar distance, d, deduced from our analysis of the interference patterns are reported in Fig.4.5 as a function of the membrane volume fraction. As expected since we have considered samples along a water dilution line, the interlamellar distance is shown to be inversely proportional to the

membrane fraction. It evolves from $91\dot{A}$ to $35\dot{A}$ with increasing values of ϕ. The bilayers thickness is deduced from Fig.4.5 by fitting Eq.4.2 to the experimental data. The bilayer thickness deduced that way is found to be: $\delta = 24.1\dot{A}$.

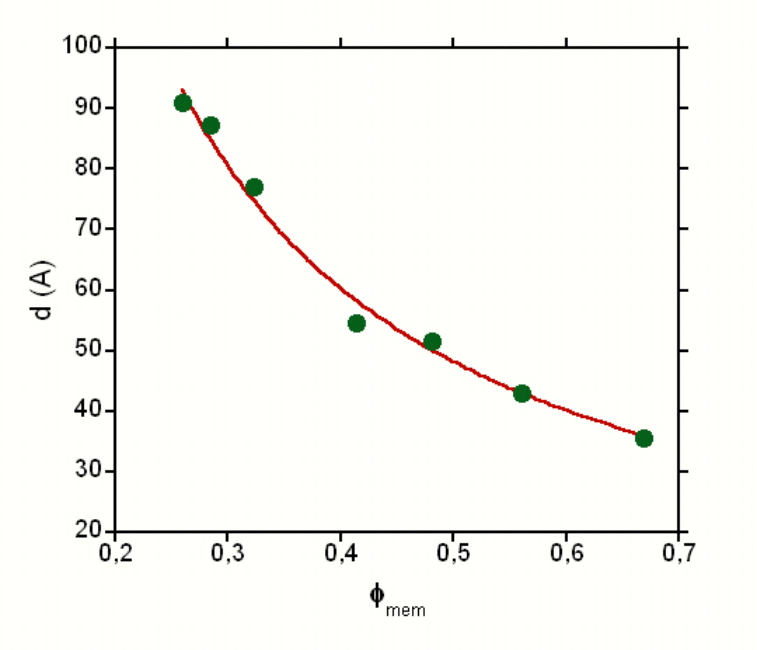

Figure 4.5: Interlamellar distance, d, as a function of the membrane volume fraction, ϕ. The plain line is the best fit of eq.4.2 to the experimental data obtained for $\delta = 24.1\dot{A}$.

We now have characterize the nanoscopic lamellar structures formed by AOT, Iso-octane and water along the considered water dilution line. The bilayer thickness deduced from this analysis of WAXS interference patterns is almost twice the value found in the literarure for the hydrocarbon chains length of AOT molecules, $l_s = 11\dot{A}$ [9]. Considering the relatively low iso-octane content of the investigated samples, this latter result is in good agreement to what one could expect.

As a conclusion, lamellar structures are formed for water concentration exceeding $30wt\%$. The thickness of the bilayers is constant along the water dilution line while the interlamellar distance is found to increase as water is added to the mixture. Whereas these lyotropic lamellar phases conserve their nanoscopic

bilayer structures, the increase of the interlamellar distance comes along with interesting features at the microscopic scales. These are investigated in the following section.

4.3 Microscopic Properties and Rheological Consequences

4.3.1 Topological Defects

As shown by our WAXS experiments, the interlamellar distance increase as water is added to the ternary mixture considered in this chapter. As a consequence one can assume that the interlamellar interactions resulting from the formation of charged layers of AOT headgroups are weaker for low values of membrane volume fraction than for higher value.

As suggested by Warriner *et al.* [8, 10–12], this reduced interactions are likely to allow for the development of local defects in the lamellar organizations of the sample. As illustrated by Fig.4.6 such local defects induces a local anisotropy and can therefore be observed in cross-polarized light microscopy.

Warriner *et al.* have shown that addition of water in the lamellar biogel they studied lead to the texture transition shown in Fig.4.6. This transition is characterized by the emergence of the permanent 'band' textures of Fig.4.6B while only the temporary textures of Fig.4.6A can be observed for lower water contents.

Anticipating on what follows one may noticed here that the development of permanent topological defects at the microscopic scale observed by Warriner *et al.* [10, 11] comes along with an apparent thickening of the lamellar phase. This thickening phenomena is such that two samples with quite similar structures at the nanoscopic scale, that is bilayers with different interlamellar distances, may show either liquid or solid behaviour depending if the defects are permanent or

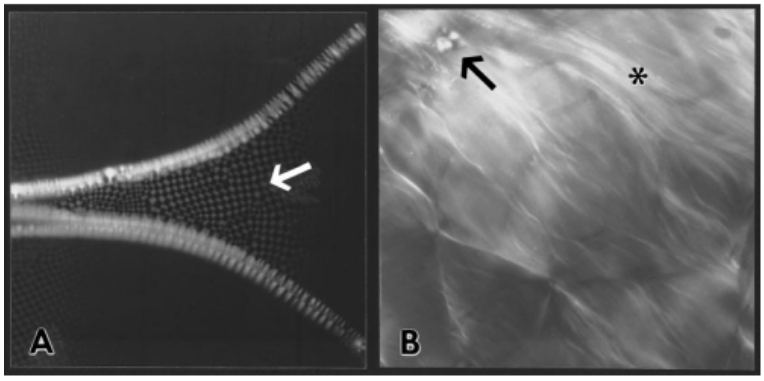

Figure 4.6: Reproduced from [10]. (A) Sample at ϕ_w = 0.748 showing oily streaks and (arrow) parabolic focal conic array surrounded by homeotropic regions. (B) Sample at ϕ_w = 0.78, around the sol/gel transition showing the 'whispy' permanent band texture (especially near asterisk) and a spherulite with an anisotropic cross (arrow).

not. This is shown in Warriner and co-workers publications by dynamic rheometry techniques [10, 11].

To characterize the microscopic properties of the different samples previously considered we have used circularly light microscopy which allows for the visualization of isochrome patterns and therefore topological defects within the considered samples. To do so the experimental setup described in Fig.3.4 of the third chapter has been used.

Three characteristic micrographs obtained on samples with different membrane volume fraction are displayed in Fig.4.7.

The micrograph displayed in Fig.4.7(a) corresponds to the higher membrane volume fraction (ϕ = 0.79). At such values of *phi* strong interactions between neighbouring bilayers does not allow for the proliferation of permanent topological defects. As in the case of the lamellar phases studied by Warriner *et al.* the micrograph 4.7(a) obtained in circularly polarized light microscopy shows only sparse defects (arrow) surrounded by large homeotropic domains. After few minutes left within the sample holder, all defects have disappeared so that a fully homeotropic black pattern is observed in circularly polarized light microscopy.

This indicates an alignment of the lamellar structures within the sample according to the surface of the parallel plates cell containing the sample.

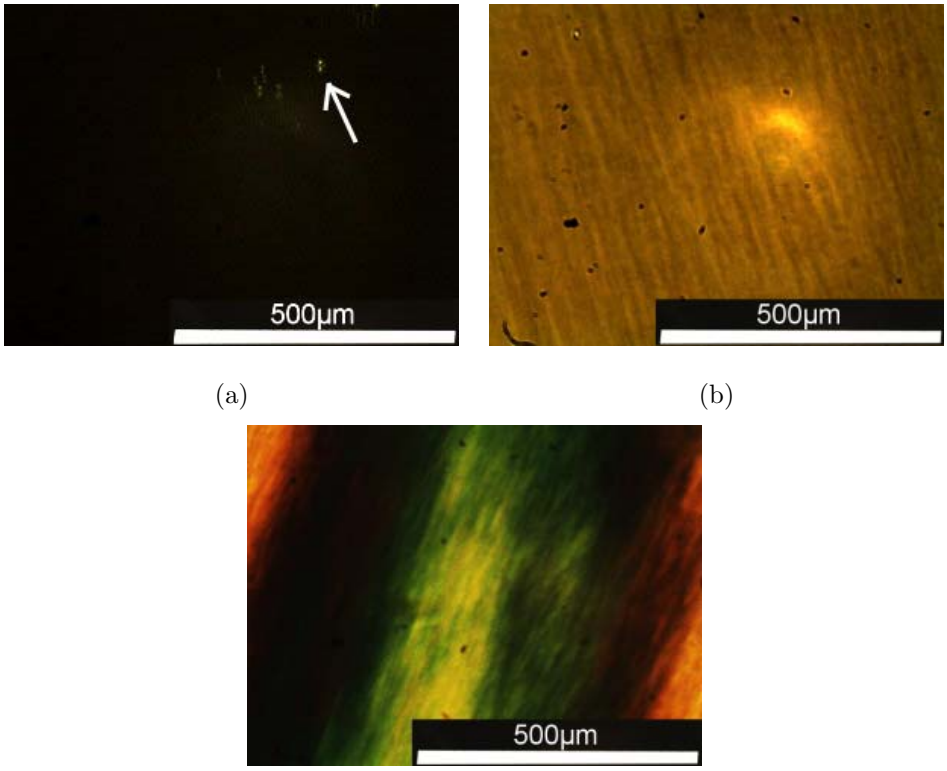

(a) (b)

(c)

Figure 4.7: Isochrome Pattern for different values of the membrane volume fraction. (a) $\phi = 0.79$, (b) $\phi = 0.41$, (c) $\phi = 0.32$.

As mentioned in the previous section, the interactions between neighboring bilayers are not as strong for lower membrane volume fractions. As shown in the micrographs 4.7(b) and 4.7(c) for membrane volume fractions $\phi = 0.41$ and $\phi = 0.32$ respectively, this allows for the proliferation of topological defects and the emergence of permanent textures. On both micrographs 4.7(b) and 4.7(c), clear 'band' textures can be observed. As for the emergence of colored domains shown for $\phi = 0.32$ in Fig.4.7(c), this corresponds to the formation of macroscopic stacked bilayers domains of inhomogeneous orientation. Finally it can be added here that, unlike for higher membrane volume fractions, the textures shown in

Fig.4.7(c) remains permanently.

The texture patterns obtained on AOT / Iso-octane /water lyotropic lamellar phases show slight differences with those obtained by Warriner *et al.* on lamellar biogels. However addition of water in our systems appears to have the same effects with the proliferation of permanent topological defects [10, 11]. The characteristic length scales of this topological defects and their associated energy is such that the rheological properties of these lyotropic systems is likely to depend on the membrane volume fraction.

4.3.2 Flow Properties

The emergence of permanent topological defects between and heterogeneous domains of favored orientation comes along with strongly different flowing properties. This is shown here by a comparison between two samples along the previously considered dilution line.

Let us first consider a sample at high membrane volume fraction ($\phi = 0.79$) and therefore free of any permanent topological defects (see Fig.4.7(a) above). The temporal evolution of the shear stress under the application of a constant shear rate is reported in Fig.4.9. As shown for an applied shear rate of $25s^{-1}$, the steady flow regime is almost instantaneously reached. Besides repeating the same measurement for different applied shear rates shows that the stress is perfectly proportional to the level of shear rate experienced by the sample.

As consequence one can assume that such defect free lamellar phases have a simple Newtonian behaviour with a shear viscosity of $0.4Pa.s$.

Considering now a sample at lower membrane volume fraction ($\phi = 0.32$)) which allows for the formation of permanent topological defects (see Fig.4.7(c) above) the apparent rheological behaviour is more complex. The results of these rheometry measurement are reported in Fig.2.7. The temporal evolution of the shear stress show a complex transient regime which leads to an apparent steady

flow. The main feature of this transient regime is an increase of the shear stress on a time length depending on the level of shear rate experienced by the sample.

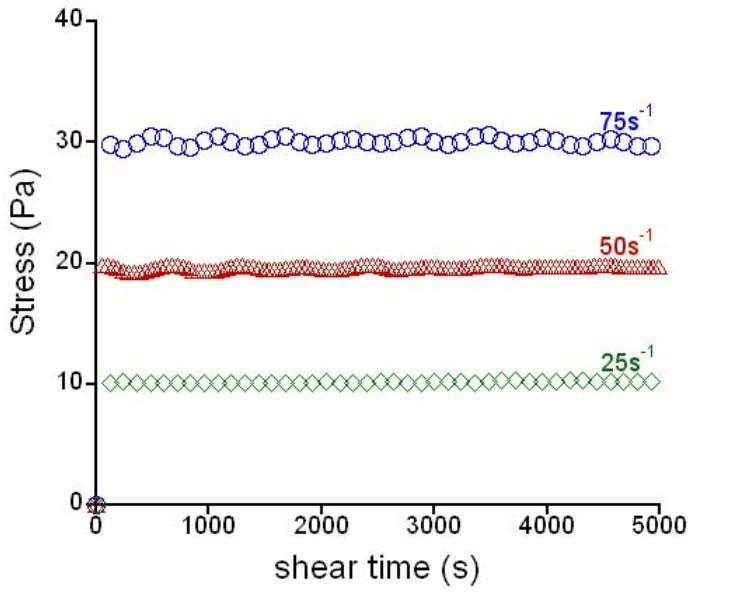

Figure 4.8: Stress temporal evolution under application of constant shear rates for a sample at high membrane volume fraction, $\phi = 0.79$.
$\circ$ - $\dot{\gamma} = 75s^{-1}$, $\triangle$ - $\dot{\gamma} = 50s^{-1}$, $\diamond$ - $\dot{\gamma} = 25s^{-1}$

According to previous studies on other lyotropic lamellar phases [2–7], such an increase of the shear stress is likely to indicate a structural transition from initially stacked bilayers in the L_α lamellar phase to unilamellar or multilamellar vesicles in the L_4 or 'onion' phase. Indeed, as shown by Diat *et al.* on SDS/pentanol/water/dodecane and AOT/brine systems, the effect of shear on initially L_α and mixed L_α/L_3 lamellar phases can lead to the formation of lamellar vesicles of which the size is controlled by the applied shear rate [3, 4].

Bergenholtz *et al.* [5] and more recently Courbin *et al.* [6, 7] have studied the dynamic of the shear-induced transition from one conformation to the other. Coupling viscosity measurements with crossed polarized light microscopy and Small Angle Light Scattering, their results indicates that the slow emergence

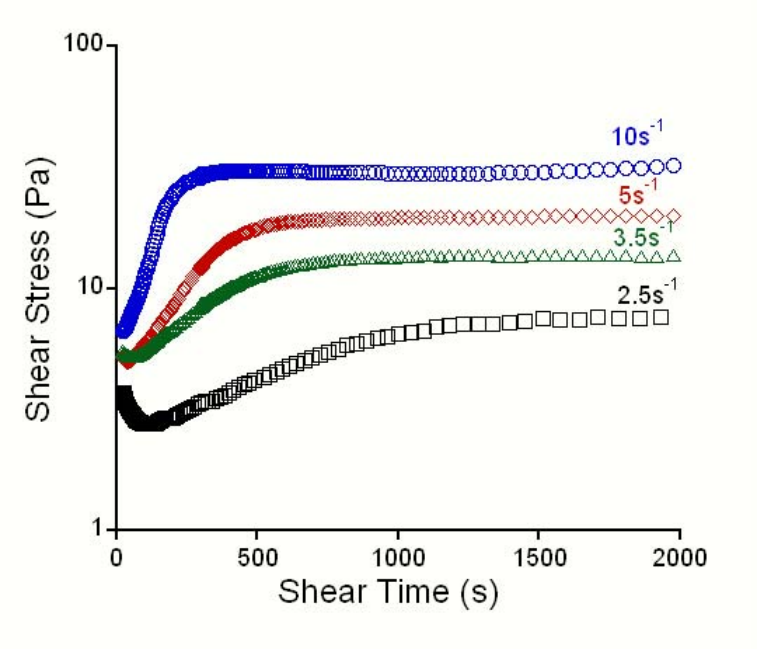

Figure 4.9: Stress temporal evolution under application of constant shear rates for a sample at low membrane volume fraction, $\phi = 0.32$.
○ - $\dot{\gamma} = 10s^{-1}$, ◇ - $\dot{\gamma} = 5s^{-1}$, △ - $\dot{\gamma} = 3.5s^{-1}$, □ - $\dot{\gamma} = 2.5s^{-1}$

of vesicles during the shearing process correspond to a strong and slow increase in the viscosity. The later is shown to only reach a steady value after few hours in Fig.4.10. Besides, plotting the time t_e at which they first observe the appearance of a Bragg peak in their SALS patterns as function of applied shear rates and measuring the variation of their samples conductivity for different shear rates, they show that the formation of vesicles in sheared L_α and L_α/L_3 lamellar phase results from a strain-controlled process.

These observations tend to confirm that the shear-induced formation of vesicles does occur through the development of a hydrodynamic instability of the membranes as predicted in some theoretical studies [13–15]. All theoretical models accounting for vesicles formation require the existence of dislocations or topological defects. The origin of these dislocations is still under debate. They might originate either from spatial variations in the gap cell [3] or the suppression by the flow of the short wavelength membranes undulation [14]. Nonetheless, un-

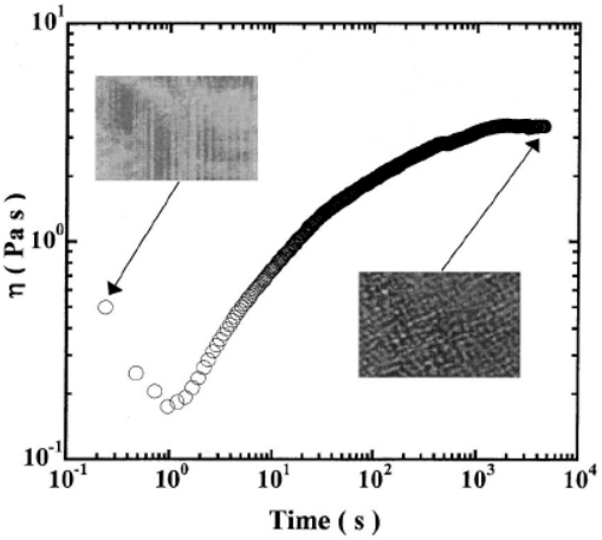

Figure 4.10: Reproduction from [7]. Variation of the viscosity under a constant shear stress (σ = 27Pa) for a 20wt%-AOT/80wt%-brine (S=1.6%). the insets are microscope images between crossed polarizers of the initial L_α/L_3 mixtures and once the final steady state is reached.

der low shear, these dislocations are believed to be able to move with the mean flow whereas at higher shear rates they can no longer follow it. This would lead to the development of a buckling instability above a critical shear rates and the subsequent rearrangement of the membranes into vesicles as shown in Fig.4.11.

4.4 Conclusion

It is now well accepted that this shear-induced lamellar to vesicles transition is a strain-controlled process. Nonetheless and in spite of numerous studies on the subject, such internal structure changes give rise to numerous experimental difficulties in rheometry. Notably, the time and shear-history dependences of the rheological properties of such structured materials makes it extremely difficult to obtain satisfying reproducible data [5]. Besides, the dynamic of the structure

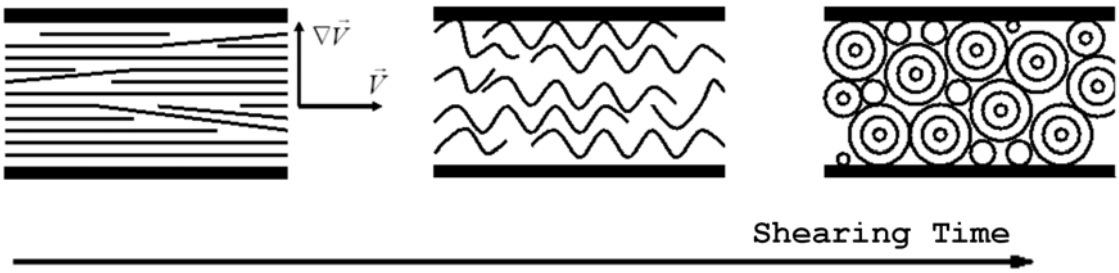

Figure 4.11: adapted from [7, 14]. Schematic representation of shear-induced Lamellar to vesicles transition. Above a critical shear rate, the dislocations accommodating for spatial arrangement of the membranes can not 'follow' the flow, this results in the emergence of a buckling instability and the subsequent formation of multilamellar vesicles tending to have a monodisperse size.

transition appears to depend on the controlled parameters in rheometry either the shear stress or the strain as well as the geometry of the shear cell [5]. At last, it is worth mentioning here that the development of vesicles comes along with an increase in the sample elasticity [16]. Curiously, only few studies can be found in the literature concerning the viscoelastic properties of the lamellar phases either in the L_α or vesicles conformations [16–18].

In the following chapters we will focus on a thorough investigation of the shear induced structural transition undergone by the defect rich lamellar phases formed by AOT in Iso-octane and water prior to focus on the rheological characterization of their shear-history and time dependent viscoelastic properties.

References

[1] N.W. Tamamushi and N. Watanabe. The formation of molecular aggregation structure in ternary system: Aerosol ot / water / iso-octane. *Colloid and Polymer Science*, 258:174–178, 1980.

[2] B.D. Simons and M.E. Cates. Vesicles and onion phases in dilute surfactant solutions. *Journal de Physiques II France*, 2:1439–1451, 1992.

[3] O. Diat, D. Roux, and F. Nallet. Effect of shear on a lyotropic lamellar phase. *Journal de Physique II France*, 3:1427–1452, 1993.

[4] O. Diat and D. Roux. Layering effect in a sheared lyotropic lamellar phase. *Physical review E*, 51:3296–3299, 1995.

[5] J. Bergenholtz and N.J. Wagner. Formation of aot/brine multilamellar vesicles. *Langmuir*, 12:3122–3126, 1996.

[6] L. Courbin, J.P. Delville, J. Rouch, and P. Panizza. Instability of a lamellar phase under shear flow: Formation of multilamellarvesicles. *Physical Review Letters*, 89(14):148305(1) – 148305(4), 2002.

[7] L. Courbin and P. Panizza. Shear-induced formation of vesicles in membrane phases: Kinetics and sizeselection mechanisms, elasticity versus surface tension. *Physical Review E*, 69(2):021504(1) – 021504(12), 2004.

[8] B.A. Coldren, H.E. Warriner, R. Van zanten, J.A. Zasadzinski, and E.B Sirota. Lamellar gels and spontaneous vesicles in catanionic surfactant mixtures. *Langmuir*, 22:2465–2473, 2006.

[9] G.J.M. Koper and W.F.C. Sager. Aggregation in oil-continuous water/ bis(2-ethylhxyl)sulfosuccinate/oilmicroemulsions. *J. Phys. Chem*, 99:13291–13300, 1995.

[10] H. Warriner, P. Davidson, N.L Slack, M. schellhorn, P. Eiselt, H.J. Idziak, H.W Scmidt, and C.R. Safinya. Lamellar biogels comprising fluid membranes with a newly synthesized class of polyethylene glycol-surfactant. *Journal of Chemical Physics*, 107(9):3707–3722, 1997.

[11] H. Warriner, H.J. Idziak, N.L Slack, P. Davidson, and C.R. Safinya. Lamellar biogels: Fluid-membrane-based hydrogels containing polymer lipids. *Science*, 271:969 – 973, 1996.

[12] S.L. Keller, H.E. Warriner, C.R. Safinya, and J.A. Zasadzinski. Direct observation of a defect-mediated viscoelastic transition in a hydrogelof lipid membranes and polymer lipids. *Physical Review Letters*, 78:25, 1997.

[13] A.S. Wunenburger, A. Colin, T. Colin, and D. Roux. Undulation instability under shear: A model to explain the different orientations of a lamellar phase under shear. *The european physical journal E*, 2:277–283, 2000.

[14] A.G. Zilman and Granek R. Undulation instability of lamellar phases under shear: A mechanism for onion formation. *European Physical Journal B*, 11:593–608, 1999.

[15] S.W. Marlow and P.D. Olmsted. The effect of shear flow on the helfrich interaction in lyotropic lamellar systems. *The European Physical Journal E*, 8:485–497, 2002.

[16] P. Panizza, D. Roux, V. Vuillaume, C.Y.D Lu, and M.E. Cates. Viscoelasticity of the onion phase. *Langmuir*, 12:248–252, 1996.

[17] O. Roblez-Vasquez, S. Corona-Galvan, J.F.A Soltero, and J.E. Puig. Rheology of lyotropic liquid crystals of aerosol ot ii.high concentrationsregimes. *Journal of Colloid and Interface Science*, 160:65–71, 1993.

[18] O. Robles-Vasquez, J.F.A Soltero, J.E. Puig, and O. Manero. Rheology of lyotropic liquid crystals of aerosol ot. iii. effect of salt and hydrocarbons. *Journal of Colloid and Interface Science*, 4163:432–436, 1994.

Chapter 5

Transient Flow Regime and Controlled Steady State

Contents

Résumé du Chapitre 5

Dans ce cinquième chapitre nous nous focalisons sur l'étude du comportement rhéologique d'une phase lamellaire riche en défauts topologiques. Celle-ci correspond à une quantité relative d'eau de 66.5% en masse le long de la ligne de dilution etudiée au chapitre précédent.

La première partie du chapitre est consacré à l'etude des régimes transitoires observés en rhéométrie de cisaillement controllée en déformation ou en contrainte. Dans les deux cas, nos résultats montrent que la fin de ce régime transitoire correspond à une transition rhéopectique conduisant au régime permanent. Cette transitions est interprétée comme la conséquence d'une transformation de l'échantillon à l'échelle microscopique sur la base de résultats de la litérature.

Que la déformation ou la contrainte soient contrôlées, nous montrons que dans les deux cas, le régime transitoire est contrôlé par le niveau de déformation de l'échantillon.

Dans un deuxième temps, nous nous intéressons aux regimes permanents obtenus en rhéométrie à déformation puis à contrainte imposée. Alors que les résultats obtenus concordent sur une certaine gamme de gradient de cisaillement ou de contrainte, ce n'est plus le cas lorsque les niveaux de contraintes et de déformations considéré deviennent trop faibles.

Enfin, dans une troisième partie nous montrons que le confinement de l'échantillon affecte fortement son comportement rhéologique. Cependant, l'effet de la géométrie de le cellule de cisaillement utilisée sur la mesure devient négligeable lorsque ces dimensions caractéristiques sont suffisament importantes.

5.1 Introduction

Surfactant molecules such as AOT are compounded by two parts with opposite properties. Whereas their polar head is hydrophilic, their apolar tail formed by one or several hydrocarbon chains is strongly hydrophobic. This confers them with the ability to self-assemble into microstructures when mixed with polar and apolar solvents such as water and iso-octane [1, 2]. In these microstructures, their polar heads are oriented toward the polar solvent, while their hydrophobic tails are swollen by the apolar solvent so that microemulsions of 'water-in-oil' or 'oil-in-water' droplets can be formed spontaneously. Such properties have found applications in many industrial processes as detergency, lubrication, emulsification, food and consumer products and so on. A consequence of these various applications is that numerous studies have been carried out on the dilute and semi-dilute regimes of surfactant concentration of self-assembling systems [3–9] and notably on AOT based ternary systems [10–16]. These studies show that the favored structures in these concentration regimes are either spherical micelles or rod-like micelles depending on the ratio between apolar and polar solvents. Coupling numerous experimental techniques have allowed to correlate their rheological properties with their structural properties.

Upon further increase in surfactant concentration, strong molecular interactions lead to the formation of ordered phases known as lyotropic liquid crystals [2]. Depending on the relative concentrations in surfactant, polar and apolar solvents, one might find different structures and spacial arrangements such as in lamellar, nematic or hexagonal lyotropic liquid crystals.

Investigating AOT based lamellar liquid crystal formed for AOT concentration up to $20wt\%$ and other self-assembling system favoring the formation of bilayers, Diat *et al.* [17] and more recently Courbin and Panizza [18] have shown that these systems exhibit complex rheological properties. Notably, the shear induced formation of multilamellar vesicles resulting from the development

of buckling instabilities above a critical shear rates have been particularly studied [17–24]. These shear induced transition have been shown to come along with a strong increase of the viscosity at a time depending on the level of strain experienced by the sample.

In spite of the numerous results concerning the shear induced formation of multilamellar vesicles in AOT based lamellar liquid-crystal phases at surfactant concentration below $20wt\%$, the rheological properties of these systems is only scarcely understood once the considered surfactant concentration is further increased. Dynamic measurements performed by Robles-Vasquez *et al.* [25, 26] show viscoelatic properties similar to that of weak gels with an elastic modulus almost one order of magnitude larger than the loss modulus. A likely reason why relatively few studies have been focused on the characterization of the flow properties of dense lamellar phases is that they exhibit strong time and shear history dependences as well as a yield stress [27]. Consequently reproducibility between measurements is hard to obtain unless precautions are taken. These complex properties are thought to result from the development of topological defects with increasing surfactant concentration which allow for the relaxation of internal stresses within the material [28–31].

The system investigated in this study is a ternary mixture of $28.5wt\%$, $66.5wt\%$ and $5wt\%$ of AOT, Water and Iso-octane respectively. These concentrations lead to the formation of a lyotropic lamellar phase at rest as shown on Cryo-electron Microscopy images in Fig.5.1.

As we can observe in Fig.5.1(a), the liquid film is stretched and observed through the aperture of a carbon grid. Clear $25nm$ thick white threads can be seen (see arrows). These are formed by stacked lamellae about $5nm$ thick (see close up view in Fig.5.1(b)). As indicated by the left arrow in Fig.5.1(a) and shown in Fig.5.1(b) the bilayers form a multiconnected structure known as sponge phase [32].

In this study, we report the results of extensive strain and stress controlled

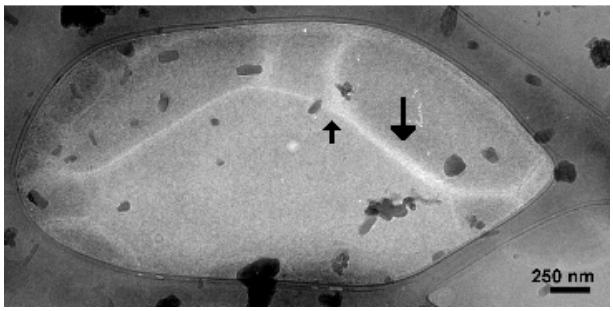

(a)

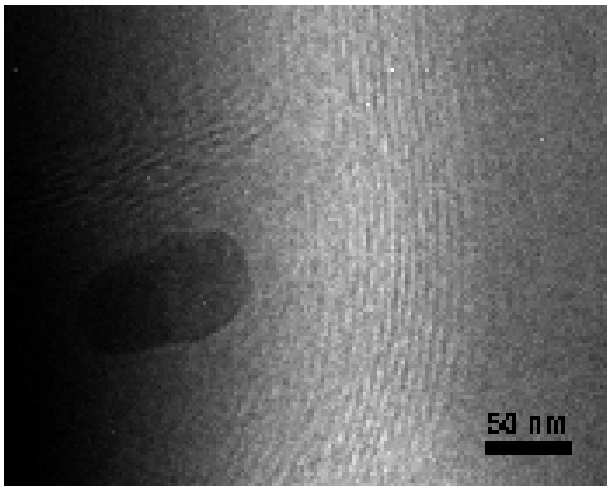

(b)

Figure 5.1: Cryo-electron microscopy images obtained on a mixture of $28.5wt\%$, $66.5wt\%$ and $5wt\%$ of AOT, Water and Iso-octane respectively. (a) View of one hole of the grid containing the mixing film. (b) Zoom on one thread identical to what is observed on the figure (a).

rheometry measurements performed on the ternary system AOT/Water/Iso-octane described above. In the first sections of the study, we focus on the transient flow regimes which exhibit strong rheopectic transitions (*ie.* an increase of the viscosity over a given length of time) for both strain and stress controlled measurements. The apparent steady states following the transient regimes in both used measurements methods are then investigated and discussed on the basis of our previous observations concerning the transient regimes. In a last section, the geometry dependence of both transient and steady regimes in the stress controlled mode are

discussed on the basis of flow field birefringence visualizations. This last remark makes it clear that all the quantities, shear rate, shear strain, deformation and shear stress, used in what follows are apparent ones. These effects of the sample confinement as well as the effects of the surface roughness on the apparent rheological properties will be thoroughly investigated in a next article. Indeed, a prerequisite for such a study is the actual existence of an apparent steady flow which is shown and discussed in the following.

5.2 Experimental Procedure

5.2.1 Materials

The anionic surfactant AOT (sodium bis[2-ethylhexil]sulfosuccinate) and Iso-octane (2-2-4 trimethylpentane) were supplied by sigma-aldrich and chosen to be 99% and 99.9% pure respectively so they were used without any additional purification process. The water was purified and deionized (resistivity $18M\Omega/cm^2$). To avoid any scattering in our data due to sample composition, a large amount of sample (200mL) containing respectively $66.5wt\%$, $28.5wt\%$ and $5wt\%$ of water, AOT and Iso-octane was prepared as follows. The desired amount of AOT was first dissolved in the corresponding amount of Iso-octane. The water was then added to the resulting solution and the whole mixture was stirred with a magnetic bar during one day in order to obtain an homogeneous phase. The remaining air bubbles were then removed by centrifugation (500rpm during 15mins). The solution was finally kept in a tightly closed container to avoid any evaporation. An evaluation of the latter consisting in weighing a given amount of sample in open space and then in a sealed environment saturated with water vapor have been performed. After 3 hours at room temperature ($T \approx 25^oC$), the sample placed in saturated atmosphere was found to have lost 2.7% of its initial mass whereas the sample placed in a free space had lost 19% of its initial mass in the same time.

As a consequence, all experiments were performed with a solvent trap so that the air surrounding the sample was saturated with water vapour.

5.2.2 Instrumentation

In this study, transient strain and stress controlled measurements were performed with a rheometer ARES (Rheometrics Scientific) and a rheometer ARG2 (TA Instruments) respectively. Strain-controlled rheometers are designed with powerful motor so that they can supply the energy necessary to deform the sample in a controlled manner. The stress responses of the tested samples are then recorded by mean of a transducer. On the other hand, stress-controlled rheometers are designed with motors of which the torque is precisely controlled. Here the torque-related stress applied to the tested sample and corresponding to the energy density experienced by the sample is precisely controlled. A consequence of this is that the response time-scale of thixotropic samples is likely to be sensitive to the used technology. Three fixtures were used in our experiments. All measurements on the rheometer ARES were performed with a Cone&Plate geometry (cone angle: $0.02rad$, Diameter: $50mm$, truncation: $47\mu m$). Except where indicated for the measurement performed with a Cup&Bob fixture (bob length $32mm$, inner radius $16mm$, outer radius $17mm$), all the measurements performed on the rheometer ARG2 were done with a Cone&Plate geometry (cone angle: $0.0175rad$, Diameter: $60mm$, truncation: $29\mu m$). The temperature was controlled to be $T = 25 \pm 0.1^oC$ by means of a 'Peltier plate' on both rheometers.

Cryo-electron microscopy experiments allowing to identify the lamellar structures of our sample at rest was performed with a Transmission Electron Microscope (cryo-TEM CM200) Philips by quench freezing thin liquid film.

5.3 Results and Discussion

5.3.1 Strain Controlled Transient Rheometry

The results of transient strain controlled measurements performed on an ARES rheometer are shown and discussed in the following. The chosen measurement method consists in monitoring the stress and normal force as a function of time upon application of a constant deformation rate using a cone and plate geometry.

The typical temporal evolution of the first normal stresses difference ($N1$) and the stress upon application of a constant shear rate ($\dot{\gamma} = 5s^{-1}$ here) is shown in Fig.5.2. Focusing first on the temporal evolution of $N1$, the flow start-up is shortly followed by a peak. Then a strong decrease toward a relative minimum reached after ten seconds is observed. Once this relative minimum reached, $N1$ starts to increase again until it settles down to an apparent plateau value.

Although the shear effects are not as pronounced for the shear stress than for $N1$, the temporal evolution of the stress in Fig.5.2 also show significant variations with the time. Indeed, the start-up of the flow is shortly followed by a slight overshoot (t_o in Fig.5.2). Then the curve slightly decreases toward a relative minimum (t_i in Fig.5.2) before it starts to strongly increase toward an apparent plateau reached at $t_s \approx 500s$. As shown in Fig.5.2, t_s also corresponds to the stabilization time of $N1$. Since the applied shear rate is constant, this strong increase of the apparent shear stress between the time t_i and t_s corresponds to an increase of the apparent viscosity. This phenomenon is therefore referred to as a *rheopectic transition* in the following discussions.

Except for the peak at the start-up of the shear flow, similar trends under constant shear have been observed on other self-assembling systems, either favoring the formation of cylindrical micelles or bilayers [5, 6, 18, 21, 24, 33, 34]. In the previously mentioned studies, such a 'rheopeptic transition' is shown to result from a shear induced structure transition governed by the level of strain experienced by the sample. In order to check that the three events presented

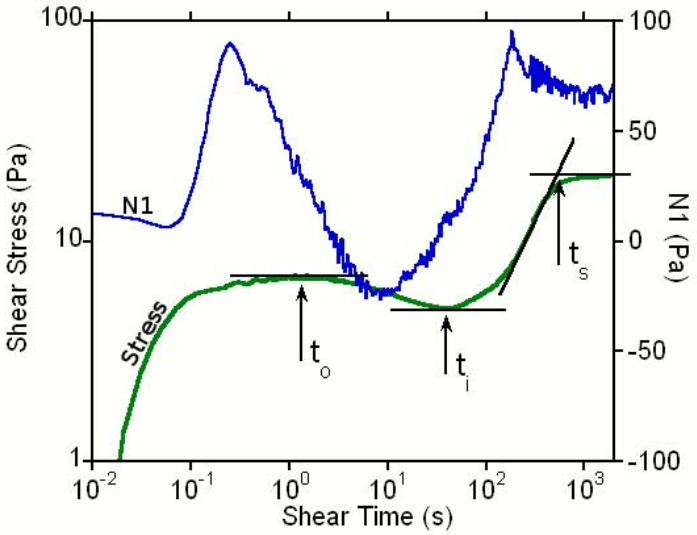

Figure 5.2: Temporal evolution of the shear stress and $N1$ upon application of a constant shear rate $\dot{\gamma} = 5s^{-1}$.

above, namely the start-up stress overshoot, its relative minimum and the transition to an apparent steady state, were indeed controlled by the level of strain experienced by the sample we simply performed measurements at different shear rates evolving from $50s^{-1}$ to $0.1s^{-1}$. The corresponding curves of the shear stress evolution as a function of time are shown in Fig.5.3.

For applied shear rates above $1s^{-1}$, the curves displayed in Fig.5.3 show similar trends as those described above (see arrows for an applied shear rates of $2.5s^{-1}$). Nonetheless, a few remarks can be added here.

For higher shear rates ($\dot{\gamma} \geq 20s^{-1}$), the length of the apparent steady stress plateau is short ($\approx 90s$ for $\dot{\gamma} = 50s^{-1}$). We have observed that its end corresponds to a shear fracture of the sample characterized by the emergence of instabilities at the edge of the cone fixture and ensuing ejection of the sample from the gap. For intermediate shear rates, no shear fracture is observed through the transparent solvent trap. The shear stress plateau is found to be stable on the whole length of the experiment. For the lower investigated shear rates ($\dot{\gamma} \leq 1s^{-1}$), the stress evolution no longer exhibits any sharp increase once the minimum t_i is reached.

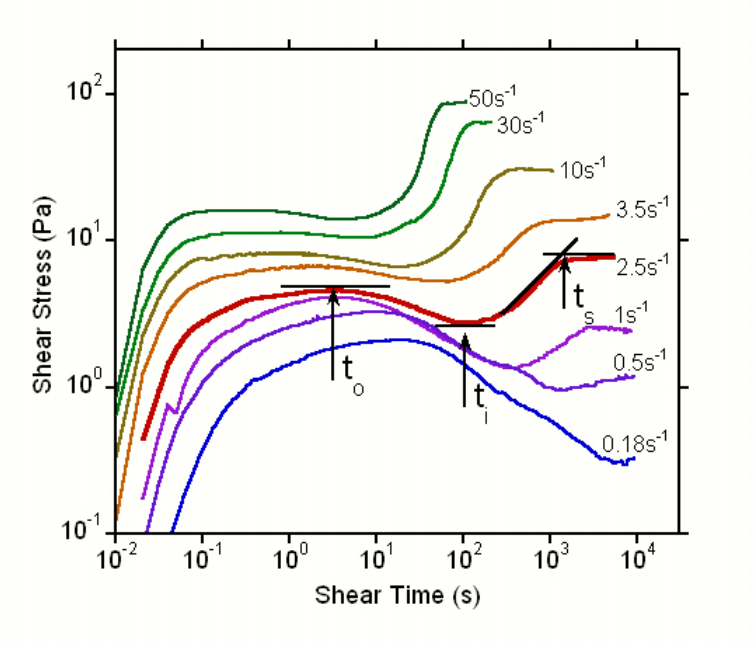

Figure 5.3: Shear stress as a function of time for constant applied shear rates evolving from $50s^{-1}$ to $0.18s^{-1}$ (from top to bottom) .

This later remark confirms previous experimental observations by Bergenholtz *et al.* [21] and Courbin *et al.* [18] who show that a sufficient shear rates is necessary to induce a structure transition in lamellar systems.

The values of the times t_o, t_i and t_s corresponding respectively to the start-up overshoot, the relative minimum and the stabilization of the shear stress for the different applied shear rates are reported in Fig.5.4. The three data sets appear to fit well to the following expressions: $\dot{\gamma} \cdot t_o = \gamma_o \approx 5$, $\dot{\gamma} \cdot t_i = \gamma_i \approx 220$, $\dot{\gamma} \cdot t_s = \gamma_s \approx 2500$. In these expressions, γ_o, γ_i and γ_s are the respective strains at which the stress overshoot, minimum and stabilization occur for all applied shear rates above $\dot{\gamma} = 1s^{-1}$. As expected, these indicate that the transient flow regime is controlled by the level of strain experienced by the sample rather than the applied shear rate. This latter property together with the rheopectic transition observed for applied shear rates above $\dot{\gamma} = 1s^{-1}$ suggest a shear induced structure transition similar to those observed by Diat *et al.* [17], Bergenholtz *et al.* [21] and

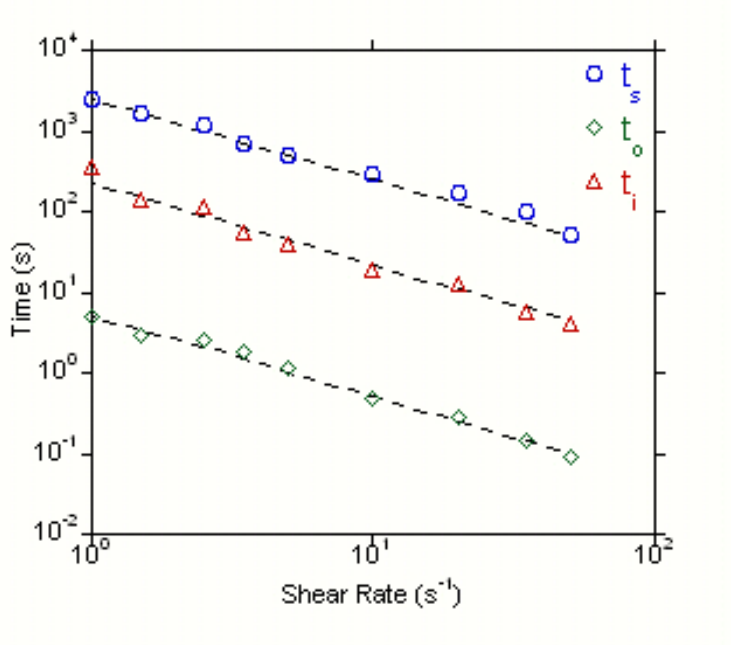

Figure 5.4: Shear rate dependence of the characteristic times corresponding to the stress overshoot at the flow start-up (t_o), the beginning of the rheopectic transition (t_i) and the stabilization of the shear stress to a plateau value (t_s). Each of them fits respectively to power law (dashed lines) given by $t_o = (5.1 \pm 0.2)\dot{\gamma}^{-1}$, $t_i = (221 \pm 12)\dot{\gamma}^{-1}$ and $t_s = (2486 \pm 62)\dot{\gamma}^{-1}$

Courbin *et al.* [18] in other lamellar systems.

5.3.2 Stress Controlled Transient Rheometry

Further insight into the rheological behaviour of these structured systems may be obtained using stress-controlled rheometry [21, 35–37]. The results of creep measurements performed on the studied system are discussed in the following section. These tests consist of imposing a constant shear stress to the sample, rather than a constant shear rate as in step rate tests, and monitoring the resulting strain as a function of time. This might seem insignificant but since the energy density brought to the sample is constant in such tests the transient deformation regime of textured materials is likely to differ from that observed in the previous section where the energy brought to the sample was the one necessary to deform the

sample at a controlled rate.

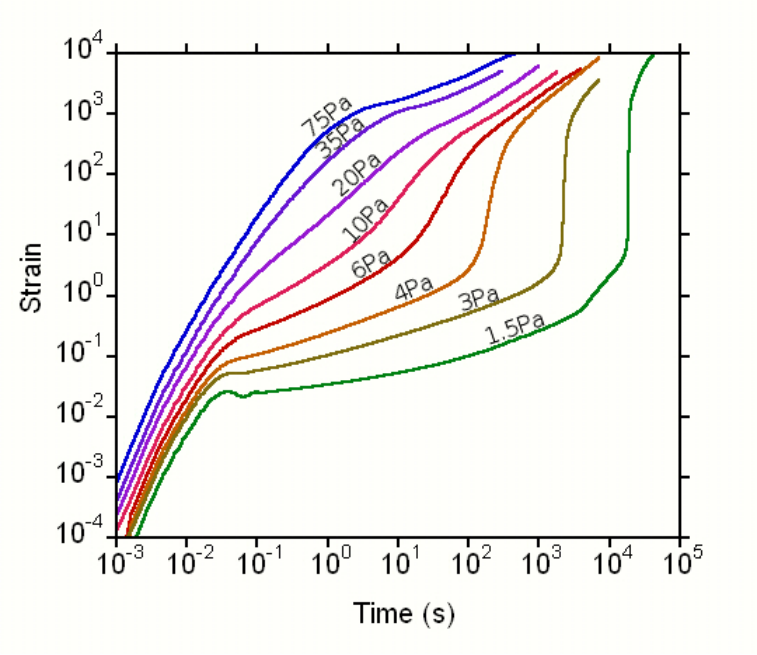

Figure 5.5: strain as a function of time upon applying constant shear stresses evolving from $75Pa$ to $1.5Pa$ from top to bottom at $T = 25^oC$

The temporal evolution of the strains upon application of constant stresses between $75Pa$ and $1.5Pa$ on freshly loaded samples is shown in Fig.5.5. As expected the displayed creep curves exhibit a complex transient regime which depends on the level of stress experienced by the sample. Such stress dependent temporal evolutions are quite similar to those recently observed by Caton and Baravian, and Coussot *et al.* on yields stress fluids of various internal structures [35, 37, 38]. As shown by these authors the start-up of the creep curves (first $0.1s$) in Fig.5.5 is governed by the inertial coupling between the material elasticity and the inertia of the rotating part of the rheometer (see references [39] and [40]). Then a complex transition is observed depending on the applied stress. For higher considered stresses (above $30Pa$) an apparent steady flow corresponding to a linear increase of the strain is rapidly reached after a decrease of the apparent shear rate (that is the local slope of the strain versus time curves).

Since the applied stress is constant, this strong decrease of the apparent shear rate one can observe in Fig.5.5 also corresponds to a rheopectic transition (*ie.* an increase of the apparent viscosity over a given length of time).

Decreasing the applied stress below $30Pa$ and further lead to the appearance of a transient regime similar to the primary creep one can observe in solid materials (*ie.* the slow deformation occurring upon application of a given stress over long time [37]). The length of time of this transient regime continuously increases as the applied stresses decrease until a dramatic increase of the strain is observed for all considered stresses. At last, this fluidification is also followed by a rheopectic transition through which an apparent steady flow regime is reached.

In the previous section, we show that the time at which the rheopectic transition occurred in strain controlled measurements was controlled by the level of strain experienced by the sample. In order to confront both measurement methods in the transient regime, we report in Fig.5.6 the evolution of the deformation rate with the level of strain experienced by the sample upon application of constant stresses evolving between $75Pa$ and $2.5Pa$.

For higher stresses (above $30Pa$), the shear rates increases continuously until it saturates for $\gamma \approx 200$ strain units. It then settles down to an apparent steady value reached at $\gamma \approx 3.5.10^3$ after a rheopectic transition (*ie.* a decrease of the apparent shear rate at constant stress). Nonetheless, at such level of applied stresses, no noticeable effect of creep or aging is observed and the studied material exhibits a 'fluid-like' behavior during the whole transient regime. For decreasing stresses, the emergence of a minimum of the deformation rates for strain values evolving from $\gamma \approx 10$ to $\gamma \approx 1$ corresponds to the end of the primary creep mentioned above. This creep regime is followed by a fluidification process which ends up with the onset of a rheopectic transition for $\gamma \approx 200$. The later decrease of the apparent deformation rate is followed by an apparent steady plateau which is reached for unusually large strain values ($\gamma \approx 2.10^3$).

To conclude on what concerns the transient regime in stress-controlled ex-

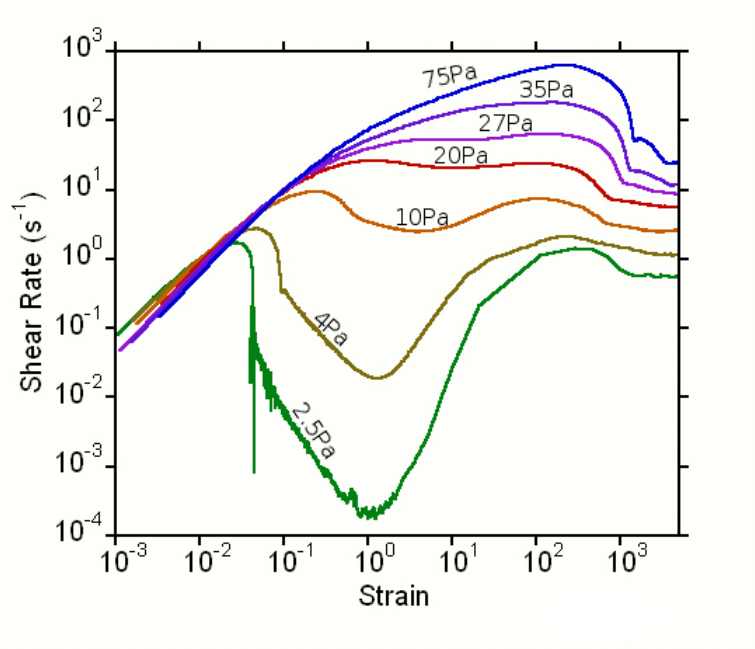

Figure 5.6: Shear rate as a function of the strain upon application of constant stresses evolving from $2.5Pa$ to $75Pa$.

periments, the following remarks can be added. Although the time-scale of the transient regime is strongly dependent on the level of stress experienced by the sample, once the studied material has entered in a fluidification process, its behavior appears to be controlled by the level of strain it experiences rather than by the level of applied stress. Besides, the characteristic levels of strain corresponding respectively to the end of the creep regime ($\gamma \approx 5$), the onset of the rheopectic transition ($\gamma \approx 200$) and the stabilization of the shear rates ($\gamma \approx 2.10^3$) match (at least in term of magnitude order) to those observed in our transient strain-controlled measurements. Consequently, the strain rather than the applied stress or shear rate appears to be the controlling parameter of the complex transient rheological behavior investigated here. Based on previous studies [17, 18, 21], these results suggest that the different characteristic strains mentioned above are the macroscopic signature of the shear induced structural rearrangement undergone by the studied system.

5.4 Apparent Steady State Flow Curves

The apparent steady values of shear stresses and shear rates obtained using stress-controlled and strain-controlled rheometry are reported in Fig.5.7. Both sets of data are shown to agree when intermediate values of either applied shear stress or shear rates are considered for $1s^{-1} \leq \dot{\gamma} \leq 20s^{-1}$ (see dashed line in Fig.5.7). Indeed, in the intermediate range, both curves appear to fit to the same power law. Anticipating on what follows, it can be noticed here that in this intermediate range all the obtained apparent steady states are preceded by a rheopectic transition.

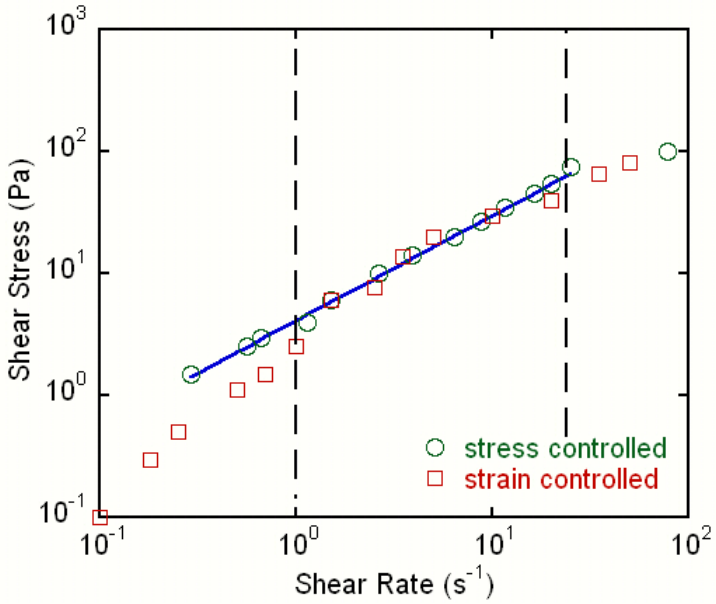

Figure 5.7: Apparent steady stress as a function of the shear rate from strain-controlled and stress-controlled rheometry. Plain line is the power law to which the measured data fit for intermediate shear rates and stresses: $\tau_{12} = 4.1(\dot{\gamma})^{0.86}$

Important remarks should be added here concerning the data shown in Fig.5.7. For higher level of considered shear stress and strain rates ($\dot{\gamma} \geq 20s$, $\sigma \geq 75Pa$), the plotted data are found to deviate from this power law. As mentioned

above, these points correspond to the emergence of instabilities at the edge of the cone & plate fixture and the following fracturation of the sample observed after the apparent stabilization of either the stress or the strain rate. Nonetheless both measurement methods show a clear stabilization of either the shear stress or the shear rates for significant length of time (not less than $90s$) prior to the emergence of instabilities. At this stage of the study, the origin of these instabilities and the subsequent sample fracturation remains to be identified.

Whereas, stress-controlled measurements match to the above power law even for lower applied shear stresses, strain-controlled measurements do not once the applied shear rates is decreased below $1s^{-1}$. The origin of these different behaviours is apparently related to the level of deformation rates experienced by the sample during the transient regime and the subsequent existence or not of a rheopectic transition prior to the apparent steady state. Indeed, As mentioned in the previous sections concerning strain-controlled experiments, levels of applied shear rate lower than $1s^{-1}$ do not lead to any clear rheopectic transition. Instead, the stress appears to stabilized close to its minimum value (see Fig.5.3). On the other hand, it is shown in Fig.5.6 for stress controlled measurements that although the time necessary for the fluidification process to occur is unusually long ($\approx 9.10^3 s$ for an applied stress of $2.5Pa$), the apparent shear rates increases up to $\dot{\gamma} \approx 1.5s^{-1}$ and remains above $1s^{-1}$ for almost $600s$. As shown in Fig.5.3 and in Fig.5.6, such levels of deformation rate are sufficient to induce a rheopectic transition. Now, previous works by Diat *et al.* and Courbin and Panizza [17, 18] have shown that such rheopectic transitions are the macroscopic consequence of the shear induced structural rearrangement of lamellar lyotropic liquid crystals into structures likely to be multilamellar vesicles. Besides, the experimental results of Courbin and Panizza as well as theoretical results [18, 41–43] indicate that the onset of this structural rearrangement results from the development of buckling instabilities above a critical shear rates. Thence, the internal structures of the sample once the steady state is reached is likely to depend on the used method, either stress

controlled or strain controlled as well as its previous shear history. Since, as it is mentioned above, low deformation rates in strain-controlled measurements do not lead to any clear structural transition while low stresses measurements do in stress controlled measurements, it can be expected that both used measurement methods do not lead to identical apparent steady states in the lower range of considered deformation rates.

5.4.1 Geometry effect on the flow curves

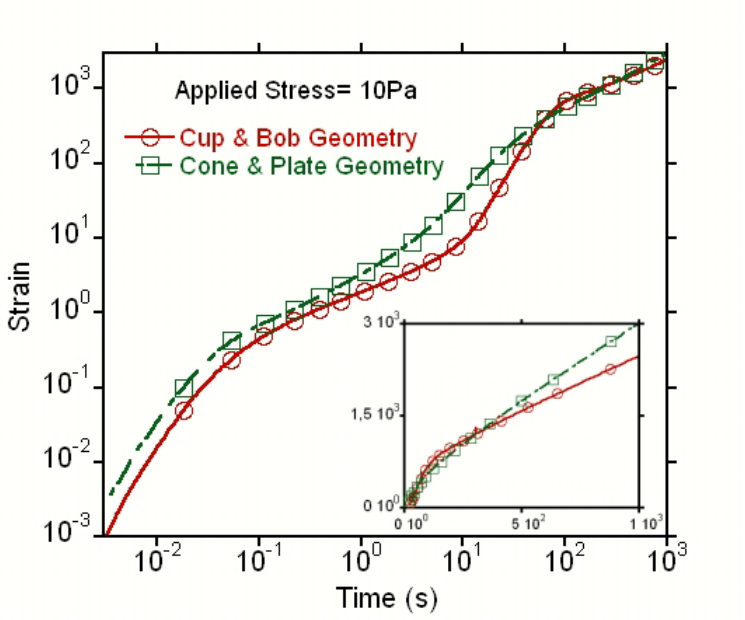

Figure 5.8: evolution of strain as a function of time upon applying a constant stress of $10Pa$ obtained by using two different geometries, T = 25^oC. The data are plotted with a linear scale on the inset to emphasize the difference between the two curves once a steady state is reached

We report in Fig.5.8 the results of two creep tests performed with the Cone&Plate and a Cup&Bob fixtures for an apparent applied stress of $10Pa$. As explained previously, the flow curves are characterized by a complex transient flow ending up in an apparent steady state flow. However, the succession of the

primary creep and the fluidification in the transient regime is less pronounced for the Cone&Plate than for the Cup&Bob geometry. Whereas higher apparent shear rates are reached for the cup&bob geometry than for the cone&plate one during the fluidification, the inverse is surprisingly found once the apparent steady state is considered. Indeed as shown in the inset of Fig.5.8, the slope of the strain versus time curves is lower for the cup&bob geometry than for the cone&plate geometry ($1.79s^{-1}$ and $2.53s^{-1}$ respectively).

In spite of numerous studies concerning the rheological properties of lyotropic lamellar phases [17–26, 31, 44], such a geometry dependence of the apparent transient and steady state flow properties has hardly ever been mentioned. Nonetheless, Salmon*et al.* [44, 45] and more recently Lutti and Callaghan [46] have given evidences concerning the existence of a slippage phenomena at the shear cell walls. If the wall slip phenomena is indeed a plausible explanation of the difference observed between both used geometries, its origins remain under discussion.

For a more complete description of the studied system we show in Fig.5.9 two photographs of the sample when observed through a plate-plate device ($gap = 2mm$) under circularly polarized light send in the velocity gradient direction. In Fig.5.9(a) the photograph is taken just after having loaded the sample in the plate-plate shear cell. It clearly shows non homogeneous domains oriented in the direction the sample has been spread on the surface. As shown in Fig.5.9(b), upon shear the domains self-align in the direction of the flow. Indeed, the domains are distributed annularly with different degrees of orientation which give the color variations in the birefringence pattern. Moreover, the domains are separated by annular black thread coming from the presence of macroscopic topological defects. What is remarkable here is their size: approximately $250\mu m$.

Although the effects of such topological defects are not well understood, they seem to play an important role on either the transient or steady rheological properties of lamellar phases [28–31]. Now, considering the size of the used shear

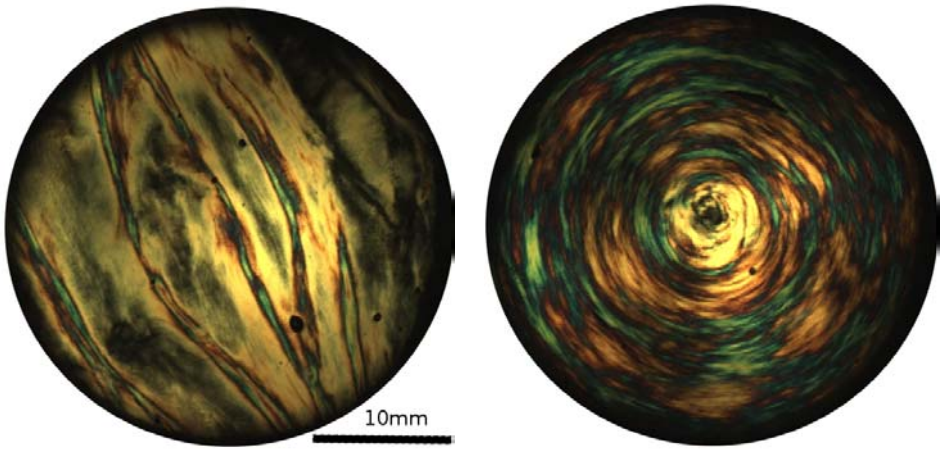

(a) (b)

Figure 5.9: birefringence image captions of the ternary mixture AOT ($28.5wt\%$)/Water ($66.5wt\%$)/Iso-octane ($5wt\%$). The sample is loaded in a transparent parallel plate experimental setup which is placed under cross polarizers and quarter-wave plate at 45° to the optic axis. The illumination is obtained by a quasi parallel white light beam. On the image (a) the sample is seen after loading whereas on the image (b) the sample is seen under shear after approximately 60s at a maximum shear rate of $15s^{-1}$.

cells of which the actual gap is evolving from $29\mu m$ to approximately $500\mu m$ for the cone&plate and is $1mm$ for the cup&bob geometry, it is clear that the confinement of the sample between shear cells walls might lead to the annihilation or at least to the rearrangement of this macroscopic topological defects. Thus, although this effect of the confinement on the topological defects formed in the studied lyotropic lamellar phase certainly deserve further investigations, it should possibly account for the origins of the apparent slippage and the difference of measurements between geometries.

5.4.2 Slip and Structures Confinement

As mentioned in the above section, the apparent rheological behaviour of lamellar phases is not only time and shear history dependent but depends also on the shear

cell geometry. This is explicitly shown in Fig.5.8 by a comparison between two creep flow curves, one being obtained with a Cone and plate geometry and the other with a Cup and Bob geometry. Consequently, we have to determined if this shear-cell geometry dependence results either from slip at the cell surfaces or from the possible annihilation of the large scale topological defects resulting from the confinement of the sample within the cone and plate geometry.

A commonly accepted method to detect slip in apparent steady flow consists in measuring the apparent steady shear rate for a given applied stress with the gaps between two parallel plates being changed from one measurement to the other [47–50]. In the eventuality of the development of slip layers at the cell walls as illustrated in Fig.5.10, the measured apparent shear rate, $\dot{\gamma}_{app}$, is related to the actual shear rate, $\dot{\gamma}$ within the sample by Mooney's equation 5.1 [51]. In the latter u_s is the slip velocity and g the gap separating both parallel plates.

$$\dot{\gamma}_{app} = \dot{\gamma} + \frac{2u_s}{g} \tag{5.1}$$

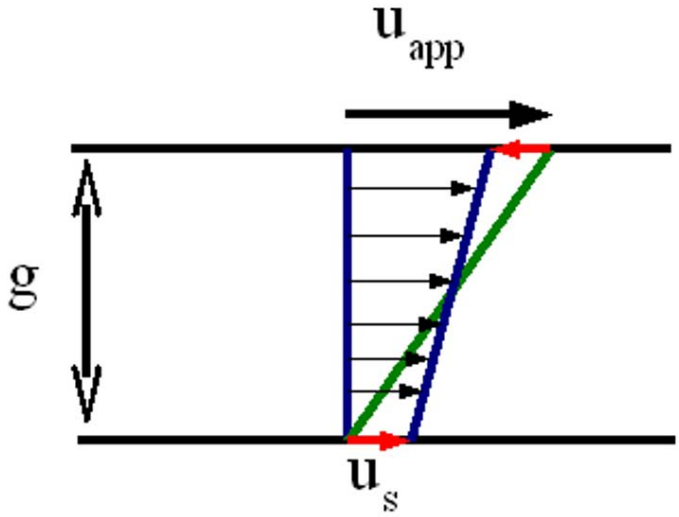

Figure 5.10: Wall slip in shearing flow

The results of such measurements are reported in Fig.5.11 for applied stresses of $20Pa$ and $40Pa$ on the ternary AOT/Iso-octane/Water system considered in the previous sections. Both displayed curves show two regimes as a function of g. Indeed, for $0.5 \leq g^{-1} \leq 1mm^{-1}$, the measured apparent shear rate is found to be constant. On the other hand, for $1mm \leq g^{-1} \leq 2.5mm^{-1}$, the measured apparent shear rate is found to increase linearly with g^{-1}. Whereas constant values of the apparent shear rate as observed for wider gaps corresponds to a no slip condition, the second regime is in agreement with *eq.*5.1. Though it would deserve further investigations, these results tend to confirm our earlier assumption concerning a possible effect of the confinement on the apparent rheological properties of the studied phase.

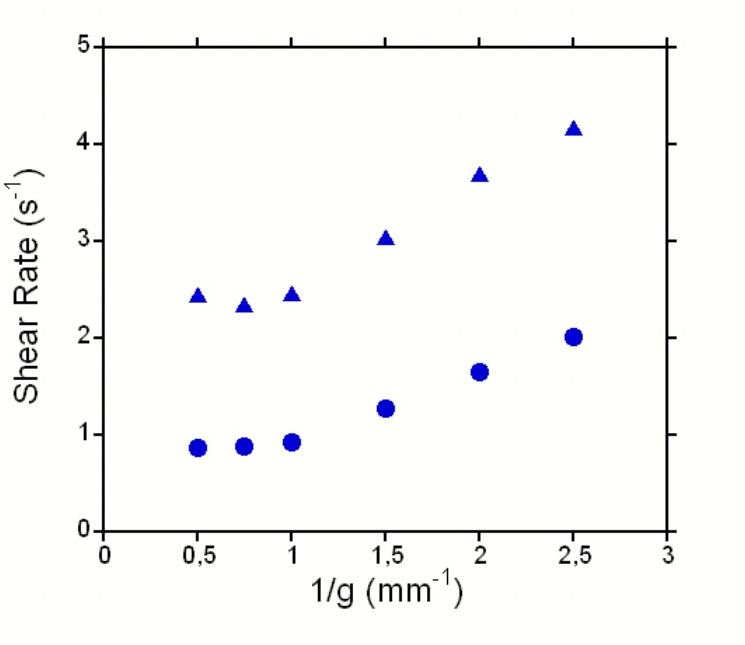

Figure 5.11: Apparent shear rate as a function of g^{-1} with g = 2, 1.33, 1, 0.66, 0.5, 0.4mm. ▲ - σ = 40Pa, ● - σ = 20Pa.

The latter remark prevents us from using cone and plate geometries in the followings. Instead we have chosen to use an especially designed PMMA cup and bob geometry in our subsequent rheometry measurements. Unlike cone and plate

and parallel plate geometries, cup and bob geometries can indeed be designed with relatively large gaps while still allowing a quasi homogeneous shear of the sample. To ascertain the validity of our rheometry measurements, notably the no slip condition at the cell walls, we have compared the results obtained with cup and bob geometries of different surface roughnesses. These were obtained by coating the shear cells with sand paper or 'scratch' paper respectively (see Fig.5.12).

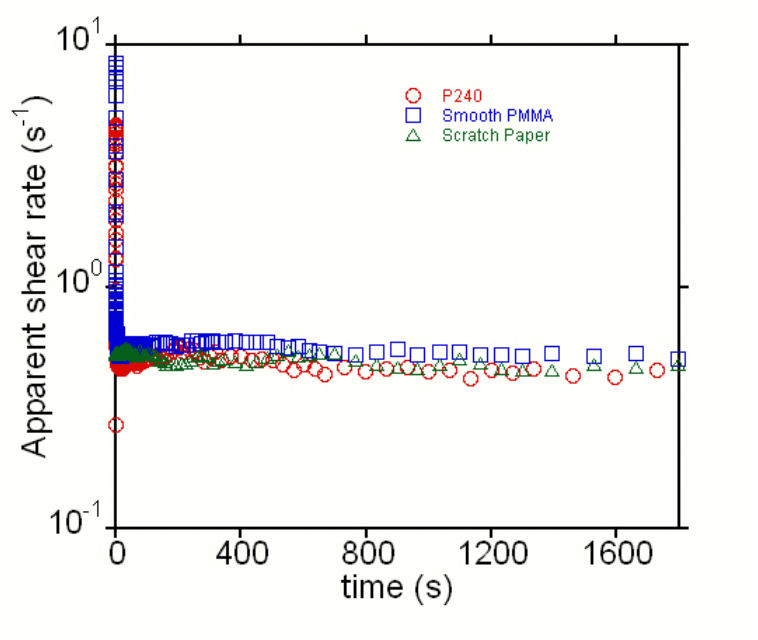

Figure 5.12: Apparent shear rate as a function of time for different surface roughnesses and an applied stress of $10Pa$. ○ - sand paper P240 ($r \approx 100\mu m$), △ - scratch paper ($r \approx 1mm$), □ - smooth PMMA surfaces.

As shown in Fig.5.12, no significant differences can be observed between the three steady state regimes of apparent shear rates obtained either with rough or smooth surfaces. As a consequence, it can be inferred that wall slip, if it does exist at all, have only slight effects on the measured mechanical properties.

5.5 Conclusion

In this chapter, we have reported and discussed the results of extensive strain and stress controlled rheometry measurements performed on a concentrated AOT / Iso-octane / Water ternary system forming interconnected bilayers with a high density of topological defects.

Focusing first on the transient flow regimes obtained by both used methods, either strain or stress controlled, and given that the shear rate remains above a critical value, our results show a strong rheopectic transition interpreted as the macroscopic consequence of a shear induced structural transition. The emergence of this transition is shown to be controlled by the level of strain experienced by the sample in both used methods. This tends to confirm earlier experimental and theoretical results by Courbin and Panizza [18] and Marlow and Olmsted [43] on other lyotropic lamellar phases.

Besides, upon application of low stresses in stress controlled rheometry, the studied system exhibits first a primary creep regime which can last up to hours. Remarkably, either in its slow deformation regime (*ie.* the primary creep) or later in its fluid regime, the sample rheological properties appear to be controlled by the level of strain it experiences.

Then, the apparent steady states which follows the transient regime in both strain and stress controlled measurements are investigated. While intermediate values of applied shear rates and shear stress are fitting to the same power law, a deviation is observed in strain controlled measurements for lower considered shear rates. This difference is shown to result from the different shear history experienced by the sample depending if the stress or the strain is the controlling parameter.

At last geometry dependence of both transient and steady regimes in the stress controlled mode are discussed. Based on flow field birefringence observations and rheometry measurements performed at various gap, this difference

is interpreted as an effect of the sample confinement on the topological defects within the sheared sample. These effects of the sample confinement as well as the effects of the surface roughness on the apparent rheological properties certainly deserve further investigations. Nonetheless, a prerequisite for such a study is the actual existence of an apparent steady flow which has been shown above.

References

[1] J. Israelachvili. *Intermolecular and surface forces*. Academic Press, London, 2nd edition, 1992.

[2] R.G. Larson. *The structure and rheology of complex fluids*. topics in chemical engineering. Oxford University Press, New York, 1999.

[3] M.E. Cates. Nonlinear viscoelasticity of wormlike micelles (and other reversibly breakablepolymers). *Journal of Physical chemistry*, 94:371–375, 1990.

[4] V.K. Jindal, J. Kalus, and H. Pilsl. Dynamic small-angle neutron scattering study of rodlike micelles in a surfactantsolution. *Journal of physical chemistry*, 94:3129–3138, 1990.

[5] Y. Hu and E.F. Matthys. Characterization of micellar structure dynamics for a drag-reducing surfactantsolution under shear: normal stress studies and flow geometry effects. *Rheologica Acta*, 34:450–460, 1995.

[6] C-H. Liu and D.J. Pine. Shear-induced gelation and fracture in micellar solutions. *Physical Review Letters*, 77:2121–2124, 1996.

[7] Y. Hu and E.F. Matthys. Rheological and rheo-optical characterization of shear-induced structureformation in a nonionic drag-reducing surfactant solution. *Journal of Rheology*, 41:151–166, 1997.

[8] Y.T. Hu, P. Boltenhagen, and D.J. Pine. Shear thickening in low-concentration solution of worm-like micelles. i.direct visualization of transient behavior and phase transition. *Journal of Rheology*, 42:1185–1208, 1998.

[9] Y.T. Hu, P. Boltenhagen, E. Mathys, and D.J. Pine. Shear-thickening in low-concentration solutions of worm-like micelles. ii.slip,fracture and stability of the shear-induced phase. *Journal of Rheology*, 42:1209–1226, 1998.

[10] N.W. Tamamushi and N. Watanabe. The formation of molecular aggregation structure in ternary system: Aerosol ot / water / iso-octane. *Colloid and Polymer Science*, 258:174–178, 1980.

[11] S.H. Chen, S.L. Chang, R. Strey, and P. Thiyagarajan. Small angl neutron scattering investigation of structural inversion in athree-component ionic micro-emulsion. *Journal of Physics: Condensed Matter*, 3:91–107, 1991.

[12] M. Kotlarchyk, E.Y. Sheu, and M.Capel. Structural and dynamical transformations between neighboring dense microemulsion phases. *Physical Review A*, 46(2):928–939, 1992.

[13] G.J.M. Koper and W.F.C. Sager. Aggregation in oil-continuous water/ bis(2-ethylhxyl)sulfosuccinate/oilmicroemulsions. *J. Phys. Chem*, 99:13291–13300, 1995.

[14] H.B. Bohidar and M. Behboudnia. Characterization of reverse micelles by dynamic light scattering. *Colloids and Surfaces A: Physicochemical and Engineering Aspects*, 178:313–323, 2001.

[15] T. Kinugasa and A. Kondo. Estimation for size of reverse micelles formed by aot ans sdehp based onviscosity measurement. *Colloids and Surfaces A: Physicochemical and Engineering Aspects*, 204:193–199, 2002.

[16] H. Gochman-Hecht and H. Bianco-Peled. Structure of aot reverse micelles under shear. *Journal of Colloid and Interface Science*, 288:230–237, 2005.

[17] O. Diat, D. Roux, and F. Nallet. Effect of shear on a lyotropic lamellar phase. *Journal de Physique II France*, 3:1427–1452, 1993.

[18] L. Courbin and P. Panizza. Shear-induced formation of vesicles in membrane phases: Kinetics and sizeselection mechanisms, elasticity versus surface tension. *Physical Review E*, 69(2):021504(1) – 021504(12), 2004.

[19] B.D. Simons and M.E. Cates. Vesicles and onion phases in dilute surfactant solutions. *Journal de Physiques II France*, 2:1439–1451, 1992.

[20] O. Diat and D. Roux. Layering effect in a sheared lyotropic lamellar phase. *Physical review E*, 51:3296–3299, 1995.

[21] J. Bergenholtz and N.J. Wagner. Formation of aot/brine multilamellar vesicles. *Langmuir*, 12:3122–3126, 1996.

[22] P. Panizza, A. Colin, C. Coulon, and D. Roux. a dynamic study of onion phases under shear flow: size changes. *European Physics Journal B*, 4:65–74, 1998.

[23] A. Leon, D. Bonn, J. Meunier, A. Al-Kahwaji, and O. Greffier andH. Kellay. Coupling between flow and structure for a lamellar surfactant phase. *Physical Review Letters*, 84:1335–1338, 2000.

[24] L. Courbin, J.P. Delville, J. Rouch, and P. Panizza. Instability of a lamellar phase under shear flow: Formation of multilamellarvesicles. *Physical Review Letters*, 89(14):148305(1) – 148305(4), 2002.

[25] O. Roblez-Vasquez, S. Corona-Galvan, J.F.A Soltero, and J.E. Puig. Rheology of lyotropic liquid crystals of aerosol ot ii.high concentrationsregimes. *Journal of Colloid and Interface Science*, 160:65–71, 1993.

[26] O. Robles-Vasquez, J.F.A Soltero, J.E. Puig, and O. Manero. Rheology of lyotropic liquid crystals of aerosol ot. iii. effect of salt and hydrocarbons. *Journal of Colloid and Interface Science*, 4163:432–436, 1994.

[27] S. Paash, F. Schambil, and M.J. Schwuger. Rheological properties of lamellar liquid crystals. *Langmuir*, 5:1344–1346, 1989.

[28] P. Oswald and Allain M. Rheology of structural defects in a lyotropic lamellar phase. *Journal of Colloid and Interface Science*, 126:45–53, 1988.

[29] C. Blanc. *Etude de l'interface lamellaire-eponge des systèmes lyotropes gonflés: Du facétage volumique et des formes de croissance aux modèles microscopiques*. PhD thesis, Université Paris VI, 2000.

[30] B. Medronho, M.G Miguel, and U. Olsson. Viscoelasticity of a nonionic lamellar phase. *Langmuir*, 23:5270–5274, 2007.

[31] C-Y.D. Lu, P. Chen, Y. Ishii, S. Komura, and T. Kato. Non-linear rheology of lamellar liquid crystals. *European Physical Journal E*, 25:91–101, 2008.

[32] A. Moldonado, R. Ober, T. Gulik-Krzywicki, W. Urbach, and D. Langevin. The sponge phase of a mixed surfactant system. *Journal of Colloid and Interface Science*, 308:485–490, 2007.

[33] S. Hofmann, P. Stern, and J. Myska. Rheological behavior and birefringence investigations on drag-reducing surfactantsolutions of tallow-(tris-hydroxyethyl)-ammonium acetate/sodiumsalicylatemixtures. *Rheologica Acta*, 33:419–430, 1994.

[34] Y. Hu, C.V. Rajaram, S.Q. Wang, and A.M. Jamieson. Shear thickening behavior of a rheopeptic micellar solution: salt effects. *Langmuir*, 10:80–85, 1994.

[35] P. Coussot, H. Tabuteau, X. Chateau, L. Tocquer, and G. Ovarlez. Aging and solid or liquid behavior in pastes. *Journal of Rheology*, 50(6):975–994, 2006.

[36] C. Baravian, G. Benbelkacem, and F. Caton. Unsteady rheometry: can we characterize weak gels with a controlled stress rheometer? *Rheologica Acta*, 46:577–581, 2007.

[37] F. Caton and C. Baravian. Plastic behavior of some yield stress fluids: from creep to long time yield. *Rheologica Acta*, 47:601–607, 2008.

[38] T. Bauer, J. Oberdisse, and L. Ramos. Collective rearrangement at the onset of flow of a polycrystalline hexagonalcolumnar phase. *Physical Review Letters*, 97:258303(1) – 258303(4), 2006.

[39] C. Baravian and D. Quemada. Using instrumental inertia in controlled stress rheometry. *Rheologica Acta*, 37:223–233, 1998.

[40] Y. Auffret, D.C. Roux, N. El Kissi, I Pignot-Paintrand, and D.E. Dunstan. aging and yielding in dense aot / iso-octane / water emulsion. *To be published*, 2008.

[41] A.G. Zilman and Granek R. Undulation instability of lamellar phases under shear: A mechanism for onion formation. *European Physical Journal B*, 11:593–608, 1999.

[42] A.S. Wunenburger, A. Colin, T. Colin, and D. Roux. Undulation instability under shear: A model to explain the different orientations of a lamellar phase under shear. *The european physical journal E*, 2:277–283, 2000.

[43] S.W. Marlow and P.D. Olmsted. The effect of shear flow on the helfrich interaction in lyotropic lamellar systems. *The European Physical Journal E*, 8:485–497, 2002.

[44] J.B. Salmon. *Ecoulement d'une phase lamellaire lyotrope: rhéochaos, systèmes dynamiques et vélocimétrie locale*. PhD thesis, Université Bordeaux 1, 2003.

[45] J.B. Salmon, S. Manneville, and A. Colin. Shear banding in a lyotropic lamellar phase. i. time-averaged velocity profiles. *Physical Review E*, 68:051503(1) – 051503(12), 2003.

[46] A Lutti and P.T. Callaghan. Effect of shear on onion textures. *European Physical Journal E*, 24:129–137, 2007.

[47] T. Aubry, L. Blonce, and M. Moan. effects in a rheometrical flow of a hydrophobically associating polymer solution: apparent slip or material instability. *applied Rheology*, 10:31–36, 2000.

[48] H.J. Walls, S. Brett Caines, A.M. Sanchez, and S.A Khan. Yield stress and wall slip phenomena in colloidal silica gels. *Journal of Rheology*, 47(4):847–868, 2003.

[49] V. Bertola, F. Bertrand, H. Tabuteau, D Bonn, and P. Coussot. Wall slip and yielding in pasty materials. *Journal of Rheology*, 47(5):1211–1226, 2003.

[50] A. Yoshimura and R.K. Prud'homme. Wall slip corrections for couette and parallel disks viscometers. *Journal of Rheology*, 32:53–67, 1988.

[51] M Mooney. Explicit formula for wall slip and fluidity. *Journal of Rheology*, 2:210–222, 1931.

Chapter 6

Shear-Induced Structural Transition

Contents

Résumé du Chapitre 6

Le sixième chapitre de ce manuscript est consacré à l'étude des transitions structurelles induites sous cisaillement dans le phase lamellaire lyotrope d'AOT, d'iso-octane et d'eau considéré au chapitre précédent.

Pour cela nous utilisons dans un premier temps des techniques de visualisation des textures en lumiére polarisée circulaire à l'échelle locale. Nous montrons ainsi une transition de textures de type 'bande' à des textures an grain. Nous montrons alors que cette transition est controlée par le niveau de déformation imposé à l'échantillon. Nous montrons également qu'une fois le régime stationnaire atteint, la taille caractéristique des textures en grain est en bon accord avec la théorie de Frank.

La deuxième partie de ce chapitre se focalise sur une analyse de l'évolution des textures de birefringence observées à l'échelle macroscopique dans une cellule de cisaillement plan-plan. Ces observations nous permettent d'établir la corrélation ntre la transition observée à l'échelle microscopique et la transition rheopectique étudiée au chapitre précédent.

Dans la troisième partie de ce chapitre nous présentons les résultats d'expériences de diffusion de rayons x sous cisaillement. Sur la base des diagrammes d'interference, nous montrons une transition structurelles à l'échelle nanoscopique. Cette transition de structure lamellaires anisotropes à des structures lamellaires isotropes indique la formation de vesicules lamellaires sous cisaillement. Ces résultats sont confirmés par des observations directes d'empreintes de cryofracture en microscopie électronique en transmission.

6.1 Introduction

In the previous chapter we have investigated the rheological behaviour of a L_3 lamellar phase. Our primary measurements in strain as in stress controlled modes have shown that the rheological properties of such material are strongly dependent on the shear time and controlled by the level of strain experienced by the sample. Notably, in both modes, a rheopectic transition is shown to occur after a strain controlled induction times evolving from seconds at high shear to hours at low shear. Considering previous works on lyotropic L_α and L_3 lamellar phases [1–12] we have assumed that this rheopectic transition is the macroscopic signature of a structural transition from interconnected bilayers to lamellar vesicles. Nonetheless, we have let this structural matter aside until now to focus on the investigation of the macroscopic rheological behavior of such systems. This has allowed us to characterize different shear regimes for which either a steady state flow can be reach or not. At last, considerations on the sample confinement within shear cells have shown the importance it might have on the apparent behaviour of such phases.

Let us now come back on the shear induced structural transition matter. As suggested by the complex rheological behaviour of the sample studied in the previous chapter, its structural properties are equally complex. Indeed at such concentration regimes AOT molecules in water and iso-octane form interconnected bilayers at rest. This is explicitly shown by the cryo-TEM micrographs in Fig.5.1 . The interconnected bilayer structures is confirmed at the mesoscopic scales by the large scale birefringence 'wispy' textures [13–15] shown in Fig.5.9(a).

Whereas cryo-TEM and freeze fracture TEM are excellent techniques to probe the sample structures at 'equilibrium', they do not allow to probe a sample in an out of equilibrium state. We notice here that the notion of 'equilibrium' is to take carefully. Indeed, the studied material is never strictly at equilibrium since topological defects allowing to accommodate for local stresses exist.

In this chapter, we will investigate this shear induced structural transition by means of two non invasive techniques. In a first section, we will focus on the mesoscopic scales with in flow birefringence textures analysis. Then, in a second section, we will focus on the microscopic structures and their evolution once sheared by means of WAXS patterns analysis. This characterization will be completed by freeze fracture observation of samples either left at rest or sheared long enough for a steady state to be reached.

Caring for clarity, we will consider a sole lyotropic lamellar phase. As in the previous chapter, the chosen ternary self-assembling system is compounded of 28.5wt% of AOT, 66.5wt% of water and 5wt% of iso-octane.

6.2 Texture Analysis

6.2.1 Definitions

Lyotropic liquid crystal such as the lamellar phases considered in this piece of work are textured materials. That is, they are optically anisotropic media compounded by domains of favored structural orientation and separated by topological defects. These topological defects, dislocation or disclination lines, allow for the orientation heterogeneities between domains. They can be visualized by polarimetry techniques such as those introduced in the third chapter of this manuscript.

In sheared textured materials one can distinguish two types of local stresses. The viscous flow energy $\sigma_\eta = \eta\dot{\gamma}$ and the elastic energy $\sigma_{el} = K/a^2$ where a is the characteristic size of the textures and K the local elastic constant [16]. As shown by Marucci [17], the condition for the textures to evolve when sheared is verified if the viscous stress is of the same magnitude or larger than the elastic stress:

$$\sigma_\eta = \eta\dot{\gamma} \;\geq\; \sigma_{el} = \frac{K}{a^2} \tag{6.1}$$

From *Eq.*6.1, one can define a texture based Ericksen adimensional number $E_{tex} \equiv \eta\dot{\gamma}a^2/K$ characteristic of the texture evolution possibility. That is the texture size only evolve when $E_{tex} \geq 1$.

Thence, the typical size of textures once a steady flow is reached reflects an equilibrium between both viscous and elastic energy [16]. Thereby upon flow start-up the characteristic length scale of textures should shrink according to equation 6.2.

$$\frac{d}{dt}\left(\frac{1}{a^2}\right) = \alpha\eta\dot{\gamma}\left(\frac{1}{a^2}\right) - \beta\frac{K}{\eta}\left(\frac{1}{a^2}\right)^2 \tag{6.2}$$

Thence, once the steady state reached, the typical size of the textures should vary according to Eq.6.3 [16, 18].

$$a \propto \frac{1}{\sqrt{\dot{\gamma}}} \tag{6.3}$$

6.2.2 Experimental Results

The experimental setup used to visualize textures in this piece of research is described in the third chapter of this manuscript. The sample is loaded in an optically isotropic and transparent parallel plate shear cell. The local shear rate is therefore given as a function of the radius by *eq.*6.4 with ω the angular velocity of the moving plate and g the distance separating both plates. It is therefore possible to control the range of probed $\dot{\gamma}_{loc}$ either by changing the applied angular velocity, ω, or the distance separating both plates, g.

$$\dot{\gamma}_{loc} = \frac{r\omega}{g} \tag{6.4}$$

The textures are then visualized by placing the shear cell between two crossed linear polarizers and quarter wave plates as shown in Fig.3.4. Micrographs of the textured patterns are recorded and analysed. It can be noticed here that no significant changes of the textures if any at all can be observed upon interruption of shear for time long enough to take several pictures along a radius

of the parallel plates. This allows us to investigate both the transient regime during which textures evolve and the steady regime for which textures have reached a constant size depending on the local shear rate. Let us first consider the textures evolution during the transient regime as a function of the local shear rate.

Transient Regime

In Fig.6.1, we display four micrographs obtained after different shear times upon application of a local shear rate of $12s^{-1}$. To minimize the possible effect of radial variation of the local shear rate in the shear cell, the angular velocity was chosen relatively slow, $\omega = 1.76rad/s$ while the gap was fixed to $g = 2mm$.

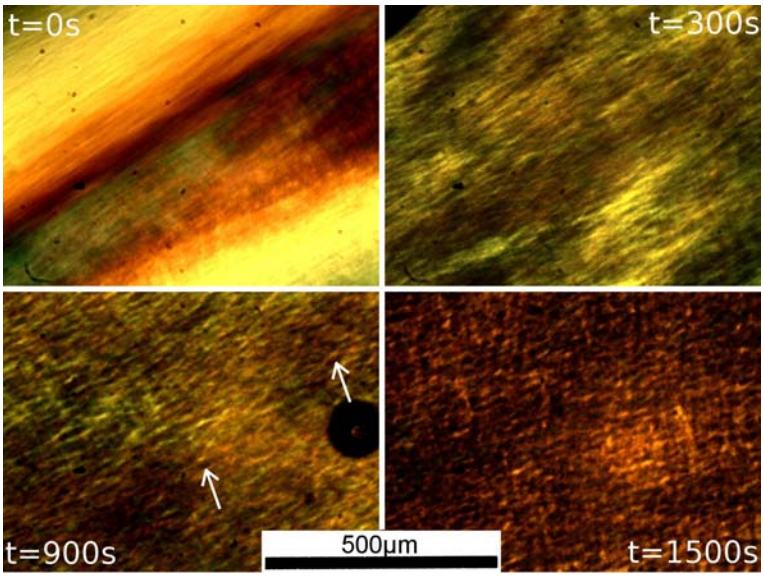

Figure 6.1: evolution of the textures with the shearing time upon application of a constant local shear rate, $\dot{\gamma}_{loc} = 12s^{-1}$

At rest, $t = 0s$, the texture pattern shows large stripes ($\approx 400\mu m$ wide) of different colors corresponding to large domains of favored orientation of the bilayers also shown at the macroscopic scale in Fig.5.9(a). Besides, thinner 'sheetlike' textures ($\approx 25\mu m$ wide) can be distinguished within the macroscopic pattern. Similar texture patterns have been observed in previous studies of lamellar biogels [13–15]. According to these studies, these thin stripes would result from the

alignment of numerous edge-dislocation lines at long range distances. Our previous observation in transmission electron microscopy of a sample with the same composition (see Fig.5.1) is indeed coherent with such an interpretation since it showed a dense number of these defects between bilayers.

Upon flow start-up the large colored bands disappear so that at shearing time $t = 300s$ the textured pattern displayed in Fig.6.1 presents only slight color variations. This latter observation indicates that the lamellar domains of heterogeneous initial orientation tend to align on the local velocity direction.

As for thinner textures, they conserve their initial 'sheetlike' aspect while appearing a bit coarser than at rest. As mentioned in the previous section these dislocation lines are prone to remain still and aligned so that shear might result in their coarser appearance and subsequent evolution [13, 15].

Upon increasing shear time, $t = 900s$, the disappearance of the colored macroscopic patterns is almost complete. As expected from *eq.*6.2, the 'sheetlike' patterns appear thinner than at shorter shear times. Furthermore the texture patterns at such shear time is clearly rougher than it was initially and one can notice the first appearance of spheroidal domains as pointed out by the arrows in Fig.6.1.

Once in the steady regime, the textures pattern does not evolve anymore and is radically different than the one observed at rest or during the transient regime. This is explicitly shown in Fig.6.1 for $t = 1500s$. The color variation of the background observed in the transient regime have completely disappeared. Instead a plain brown background is observed which indicates an homogeneisation of the material. As for the defect textures, they clearly show different patterns when compared to those observed at rest and during the transient regime. Indeed the grainy spheroidal domains mentioned above have spread over the whole observation window.

These observations confirm our earlier assumptions concerning the structural transition undergone by the investigated sample when sheared. Indeed the

transition from 'sheetlike' to 'grainy' textures observed in Fig.6.1 has been shown to correspond to the shear induced formation of lamellar vesicles [9, 10].

We have shown in the previous chapter that the macroscopic rheological properties of the studied phase were controlled by the level of strain it experienced. In an attempt to relate this macroscopic rheopectic transition to the texture evolution shown above, we can compare the micrographs of Fig.6.1 to those of Fig.6.2. In the latter the local shear rate is fixed to half of the one considered above, $\dot{\gamma}_{loc} = 6s^{-1}$.

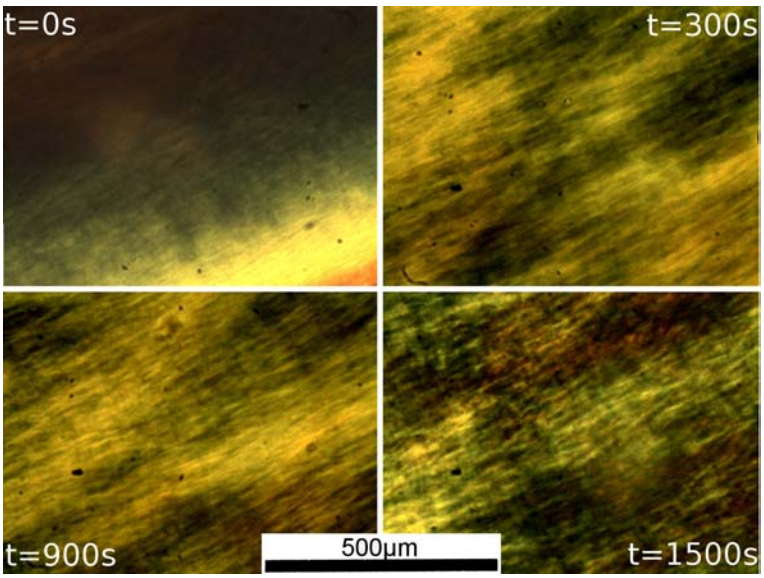

Figure 6.2: evolution of the textures with the shearing time upon application of a constant local shear rate, $\dot{\gamma}_{loc} = 6s^{-1}$

As expected, the micrographs of Fig.6.2 show similar texture patterns as those discussed above. Nonetheless the evolution process at $\dot{\gamma}_{loc} = 6s^{-1}$ appears to be slower than at $\dot{\gamma}_{loc} = 12s^{-1}$. Indeed the textures at $t = 300s$ and $t = 900s$ appears to conserve their smooth 'sheetlike' aspect. It is only after shear times up to $t = 1500s$ that rougher texture aspect can be observed. This tends to confirm the strain controlled nature of the structural transition process at the microscopic scale.

Steady State Regime

In the above section, we have shown that a texture transition occurred within the studied sample upon shear. This transition leads to the formation of grainy spheroidal domains once the steady state is reached. Let us now consider this steady regime and the effect of the applied local shear rate magnitude on the final texture of the sample observed in cross polarized light. Fig.6.3 show different texture patterns corresponding to different local shear rates once in the steady state.

As expected from *eq.*6.3, the micrographs of Fig.6.3 show that the grainy spheroidal textures shrink with increasing values of the local shear rate. The characteristic sizes a of the textures shown in Fig.6.3 can be roughly determined by counting the number of peaks on a profile of the light intensity along a straight line of known length. The values of a obtained that way are reported in Fig.6.4. They fit pretty well with *eq.*6.3 given above so that Frank's theory might be relevant to describe the steady structural properties of the investigated samples [16, 17].

The following remark can be added thereafter concerning the organization of the grainy domains within the flow. Indeed at lower considered apparent local shear rate, $\dot{\gamma}_{loc}$ = $30s^{-1}$ the grains tend to align one behind the other according to the velocity direction (see white line in the bottom right corner of each micrograph in Fig.6.3). This alignment of the domains along the velocity direction persist at higher apparent shear rates but a second direction of alignment emerges. This second direction of alignment appears to be perpendicular to the first direction. This can be best seen on the micrographs taken for $\dot{\gamma}_{loc}$ = 65 and $83s^{-1}$. If an alignment of the domains according to the velocity direction could be expected [16], the emergence of a second alignment direction is rather unexpected. Although it has been mentioned in earlier works on nematic liquid crystals [16, 19], the origin of this secondary favored alignment direction within the flow remains an open question at this stage.

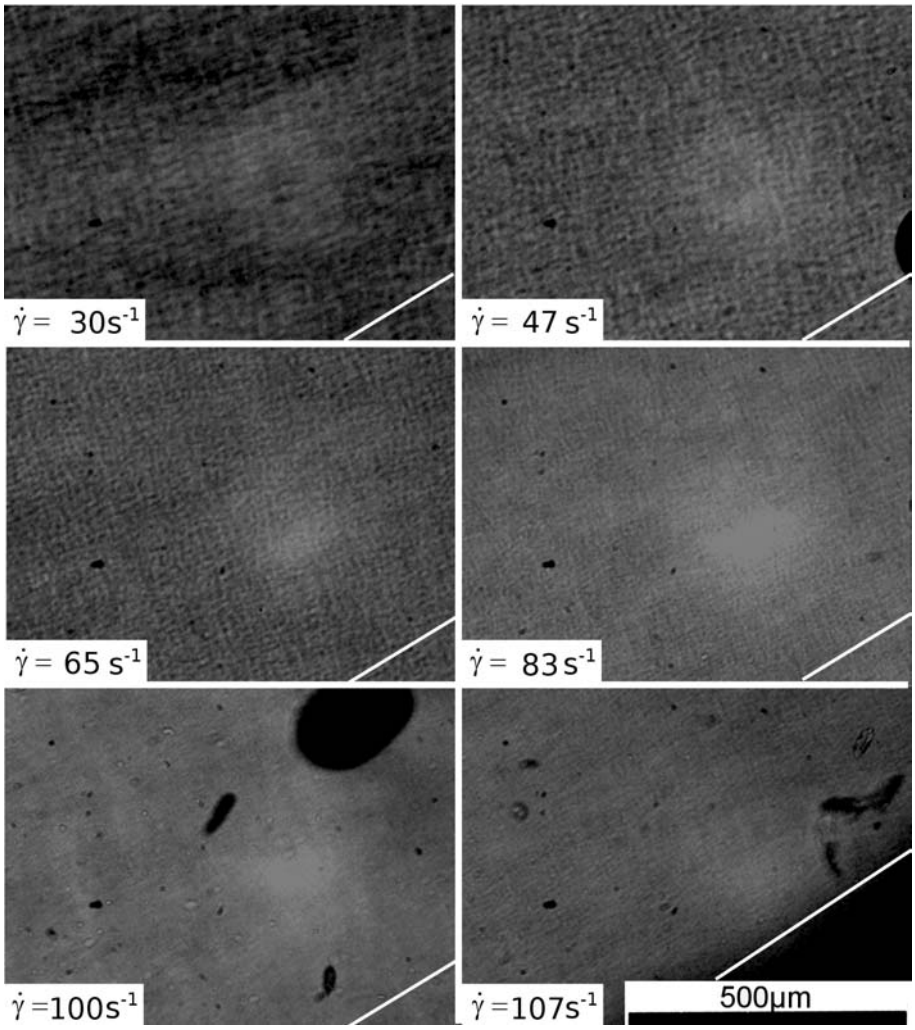

Figure 6.3: Micrographs of the investigated sample as a function of $\dot{\gamma}_{loc}$ once in the steady state. The length scale given for $\dot{\gamma}_{loc}$ is the same for all micrographs. The white line at the bottom right corner of each pictures corresponds to the local velocity direction

A last remark can be added on what concerns the steady state properties of the textured domains shown in Fig.6.3. Indeed, the rheological measurements discussed in the previous chapter lead to sample fracture for shear rates below those considered here. Such sample fractures are not observed with this particular geometry configuration. In order to observe significant domains size difference along the radius we have indeed chosen to set the gap between both plates to its

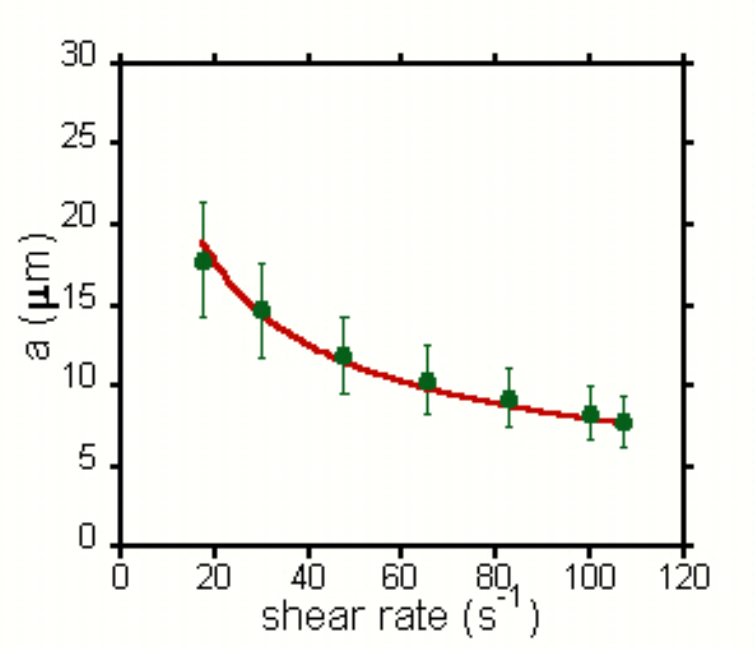

Figure 6.4: Evolution of the size, a, of the textured domains as a function of the apparent local shear rate. The plain line is a fit of *eq.*6.3 on the experimental data: $a \approx \frac{82.2}{\sqrt{\dot{\gamma}_{loc}}}$

shortest available value, g = 250μm, while keeping the angular velocity at the same value as the one applied in the previous section, ω = 1.76rad/s. Besides, unlike the cone and plate shear cell used in the previous chapter, the parallel plate shear cell used for our texture observations is fully closed. That is, the sample is confined in a closed space. Consequently, although such a confinement might have uncontrolled effects on the local apparent shear rates, especially at the outer edge of the plate, this might also prevent the sample from fracturing.

6.2.3 Conclusion

In such conditions, one has to consider the previous observations cautiously. Notably, we emphasize the use of the term *apparent* local shear rate in the above sections. Although this could be a serious limitation, these observations also clearly show a shear-induced structural transition at the microscopic scale. Notably, The

shear induced formation of such small grainy textured domains accredit our previous assumptions concerning the origin of the rheopectic transition discussed in chapter 4.

Although our observations at the microscopic scale are coherent with the previously investigated rheological properties of the sample, they do not provide yet a clear relation between both the transition at the microscopic level and the transition at the macroscopic level. Let us now relate both microscopic and macroscopic phenomena.

6.3 Textures and Rheological properties

An important asset of the experimental device used in this piece of research to visualize the texture patterns within sheared samples is that the camera can be fitted either with a long focal lens or with a wide angle lens. Indeed this allows us either to probe the microscopic evolution of the textured domains or to follow their evolution at the macroscopic scale in the whole shear cell.

In the following paragraphs, we will first describe and comment the shear induced structural transition within the studied material on the basis of such macroscopic observations. In a second section this structural transition at the microscopic scale will be related to our previous rheological measurements by means of simple considerations.

6.3.1 Experimental Observations

We show in Fig.6.5 the macroscopic shear induced evolution of the textures within the studied lyotropic lamellar phase. The sample is initially loaded in the same parallel plate shear cell as the one used previously. The shear conditions are the same as in the investigation of the transient regime at the microscopic scale, $\omega = 1.76 rad.s^{-1}$ and $g = 2mm$. Therefore, The local apparent shear rates along a radius linearly from $\dot{\gamma}_{loc} = 0s^{-1}$ at the cell centre, $r = 0$ to $\dot{\gamma}_{loc} \approx 13s^{-1}$ at the outer

radius, $r = 15mm$.

The birefringent patterns at rest, $t = 0s$, show large domains of favored orientation (colored bands) corresponding to those observed at the microscopic scale in the previous section. The apparent orientation of these domains within the whole shear cell bulk results from the way the shear cell is loaded. Indeed the sample is first spread on one of the plate with a syringe with a back-and-forth movement. The shear cell is then closed with the second plate. Sample overload is circumvented by two small apertures at the edge of the observation window which can be closed once both plates are in the desired positions.

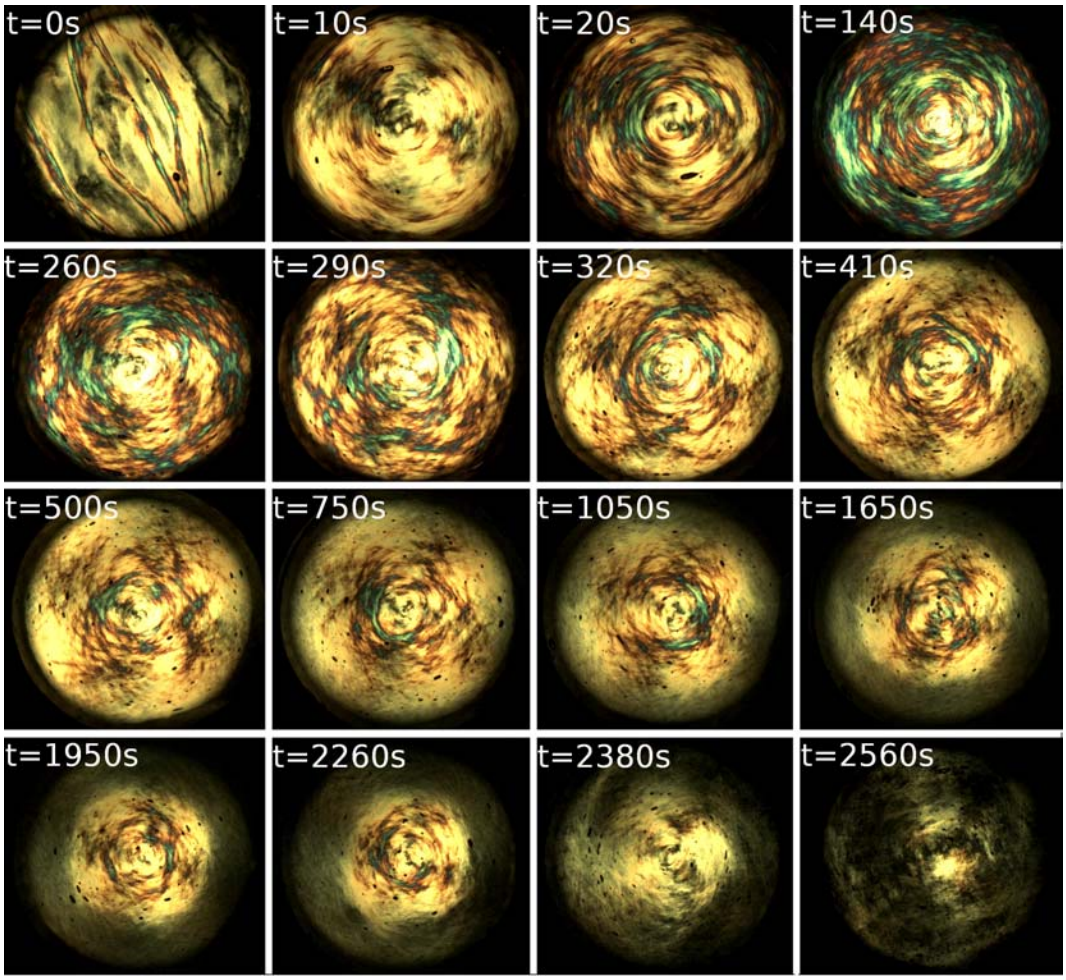

Figure 6.5: Macroscopic birefringent patterns as a function of the shear time within a parallel plate shear cell. $\omega = 1.76 rad.s^{-1}$, $g = 2mm$.

Upon shear start-up, $0 < t < 140s$, the initial birefringent domains quickly disappear to be replaced by macroscopic ring shaped domains of favored orientation corresponding to the blue and red domains shown in Fig.6.5 at $t = 140s$.

Upon increasing shear time, $140 < t < 410$, the blue and red heterogeneous domains observed at shorter time start to shrink at the edge of the observation window. They are replaced by brighter regions with few remaining defects region forming annular dark threads in the global patterns. The time at which this transition occurs appears to be controlled by the level of local shear rate experienced by the sample. Indeed, these bright regions appear first at the edge of the observation window and develop towards the plate centre with increasing shear times. It can be added here that this transition does not occur for smaller values of local shear rates since large scale textures remain at the cell centre for much longer time than those considered here.

As for a comparison with the observations performed at the microscopic scale, the time corresponding to the development of this bright region at a given radius corresponds to texture pattern showing a smooth 'sheetlike' aspects.

Following the appearance of the almost uniform bright region at the edge of the observation window, $410 < t < 2260s$, a second transition is observed with the development of a dark region at the edge of the observation window. As for the development of the bright region, the dark region appears to develop toward the shear cell centre according to the shear time.

The apparition of this developing dark ring at the macroscopic scale is coherent with our previous observations at the microscopic scale. Indeed we have shown in the previous section the development of grainy spheroidal domains at shear time similar to those considered here (see Fig.6.1). Given the typical size of these grainy textures, $a \approx 25\mu m$ according to the fitting equation in Fig.6.4, and their spherical aspect, it could indeed be expected that they appear almost isotropic (dark) when observed at the macroscopic scale.

Finally, for $2260 < t < 2560s$, the central region of the shear cell in which

large colored domains remained until then is transformed. Nevertheless, unlike for high shear region, this apparent transformation corresponds to the development of an instability of the central part of the sample. Indeed, at $t \approx 2300s$ the initially untransformed region appears to 'oscillate' around its initial position before to be either transformed or mixed with outer region.

The start-up of this instability appears to correspond to the time at which the fully transformed region (dark region) attains the radius below which no transformation has been previously observed (heterogeneous colored domains). Although its origin remains to be identified, such an instability could be at the origin of the sample fracture we observed in our previous rheological measurements using 'open' shear cells (see chapter 4). That is, shear cells for which the sample can be ejected at the edge of the geometry.

Except for the emergence of the instability after long shear times, the shear induced evolution of the birefringent pattern shown in Fig.6.5 is fully coherent with our previous observation at the microscopic scale. Let us now relate these results with the results of our rheological measurements.

6.3.2 Analysis and Discussion

The results of the strain controlled measurements presented in the previous chapter indicates that the rheological properties of the investigated phase depend on the level of strain it experiences. As shown in Fig.6.6 for shear rates similar to those considered in the previous section, after a transient regime the measured stress reaches a plateau value through a rheopectic transition. As previously shown, the time at which the transition occurs is inversely proportional to the applied shear rates according to *eq.*6.5.

$$t_s = \frac{\gamma_s}{\dot{\gamma}} \approx \frac{2500}{\dot{\gamma}} \tag{6.5}$$

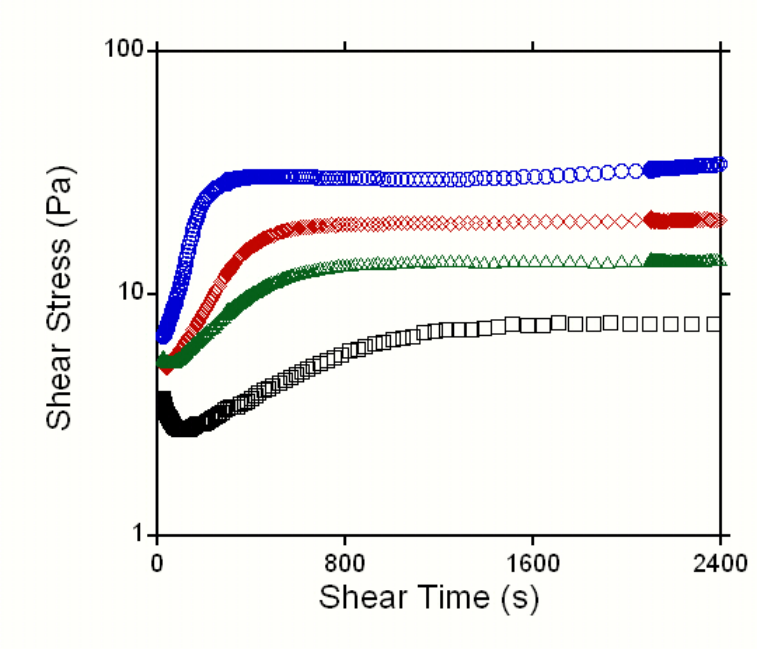

Figure 6.6: Temporal evolution of the stress upon application of constant shear rates: ○ - $\dot{\gamma} = 10s^{-1}$, ◇ - $\dot{\gamma} = 5s^{-1}$, △ - $\dot{\gamma} = 3.5s^{-1}$, □ - $\dot{\gamma} = 2.5s^{-1}$.

Let us then assume that the transition from 'sheetlike' textures to 'grainy' textures shown in Fig.6.5 is also controlled by the level of strain experienced by the sheared sample. In other term, we assume that the appearance of the dark ring in Fig.6.5 and its further development toward the cell center occurs at a given constant critical strain, γ_c. Besides, we note t_0 the time at which the dark ring is first detected at the edge of the observation window. The relation between γ_c and the local shear rate $\dot{\gamma}_{loc}$ is then given by *eq.*6.6.

$$\gamma_c = \int_{t_0}^{t} \dot{\gamma}_{loc}.dt' \tag{6.6}$$

Using *eq.*6.4, *eq.*6.6 becomes:

$$\gamma_c = \frac{r_t \omega}{g}(t - t_0) \tag{6.7}$$

In *eq.*6.7, r_t corresponds to the position of the transition front between bright and dark birefringence rings in the shear cell. The experimental values of r_t as a function of the shear time are deduced from Fig.6.5 and reported in Fig.6.7.

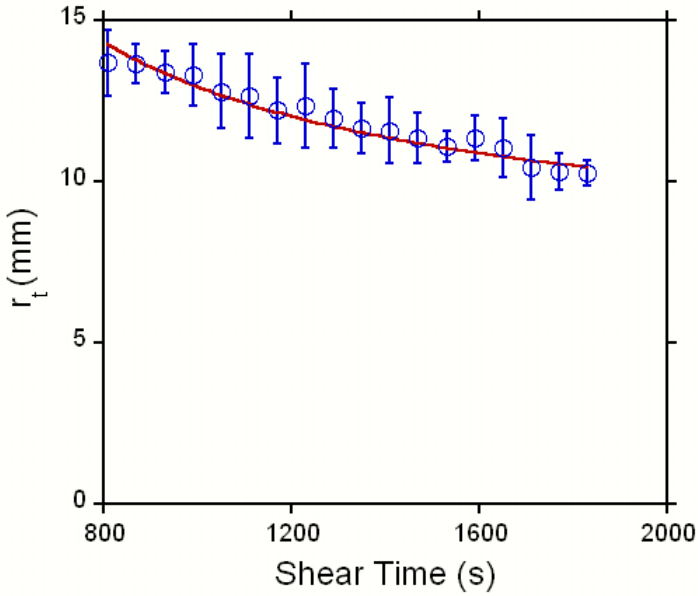

Figure 6.7: Position of the transition front in Fig.6.5 as a function of applied shear time. The plain line is a fit of the data according to *eq.*6.8 with $\omega = 1.76 rad.s^{-1}$ and $g = 2mm$.

The value of the critical strain necessary for the anisotropic to isotropic transition to occur can then be deduced by fitting *eq.*6.8 to the experimental data of Fig.6.7.

$$r_t(t) = \frac{g\gamma_c}{\omega\,(t - t_0)} \tag{6.8}$$

It gives:

$$\gamma_c \approx 4800 \pm 700 \tag{6.9}$$

This value of γ_c determined from our observations of the birefringent patterns within a parallel plate shear cell, is to be compared to the one obtained from rheological measurements with cone and plate geometries, $\gamma_s \approx 2500$, corresponding to the attainment of the stress plateau in Fig.6.6. Although both

values are in the same range of magnitude, they differ by a factor 2. Nonetheless such a difference is not unexpected. Indeed as shown in the previous chapter in Fig.5.2 and Fig.5.3, the criterion chosen to define t_s and therefore γ_s might lead to underestimation of the strain actually necessary to reach the stress plateau.

Indeed, if the start-up of the steady plateau in Fig.6.6 corresponds to the start-up of the transition from 'sheetlike' texture to 'grainy' textures as it seems to be from local birefringence observations, the emergence of the dark ring in the global birefringence pattern might rather correspond to the complete transformation of the local textures. As a consequence, the difference observed between γ_c and γ_s could be expected. It would then corresponds to the strain necessary to reach a true out-of-equilibrium steady state.

6.3.3 conclusion

As a conclusion, the above analysis of birefringence texture confirms that the rheopectic transition uncovered in the previous chapter originates from microscopic phenomena, notably a shear induced reorganization of the topological defects within defect rich lamellar phases. Having relate the macroscopic rheological properties of these systems to the organization of the defects within the sample, one has left to identify the origin of such a microscopic transition. Let us now investigate the shear induced structural properties of the considered system at the nanoscopic scale.

6.4 Nanoscopic Structural Transition

In this section we will investigate the temporal evolution of the structures formed by AOT in the ternary system considered until now upon application of a constant shear rates. To do so, we have recently performed Wide Angle X-ray Scattering experiments on the D2AM beam line of the European Synchrotron Radiation

Facility. A detailed description of the device we have used in these experiments is given in the third chapter of this manuscript.

The complete analysis of these recent results remains to be performed at this stage of the study. However, a qualitative interpretation of the results can be made on the basis of the scattering patterns. This will bring significant insights concerning the material evolution during the shearing process. Besides these qualitative results can be confronted to the results obtained in Freeze Fracture Transmission Electron Microscopy.

As mentioned in the third chapter of this manuscript, the sample is loaded between two parallel plates. The shear cell position is controlled so that it goes back and forth between two positions along the radius of the plate corresponding to apparent local shear rates, $\dot{\gamma}_{loc} = 13s^{-1}$ and $\dot{\gamma}_{loc} = 3s^{-1}$ respectively. Fixing the the integration time to $10s$ and given the time necessary for the shear cell to move from one position to the other, the elapsed time between each measurements at a given $\dot{\gamma}_{loc}$ is given by $\Delta t_m \approx 90s$. Considering the time scale of the transition processes shown at the microscopic and macroscopic scales, such a time resolution appears to be sufficient in order to probe the sample structural evolution at the nanoscopic scale.

6.4.1 Wide Angle X-ray Scattering

The temporal evolution of the scattering patterns upon application of a constant local shear rate, $\dot{\gamma}_{loc} = 13s^{-1}$, is shown in Fig.6.8.

The scattering pattern shown in Fig.6.8 for $t = 0s$ confirms the anisotropic and lamellar structure of the investigated phase at rest. It shows Bragg peaks positioned along a favored scattering direction at scattering length, $q_1 = 0.0927A^{-1}$, $q_2 = 2q_1$ and $q_3 = 3q_1$. Such a disposition of the Bragg peaks is indeed characteristic of periodically stacked lamellar structures oriented perpendicularly to the favored scattering direction [11, 13, 15].

Upon shear start-up the lamellar nature of the structures is conserved

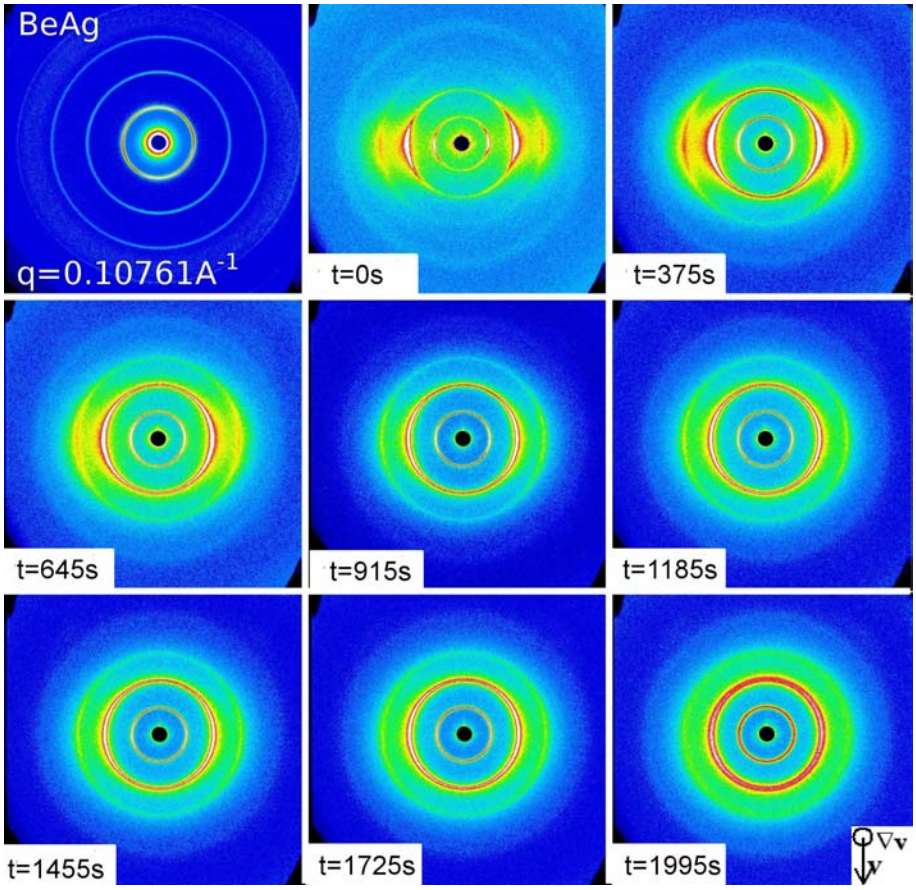

Figure 6.8: WAXS patterns temporal evolution upon application of a constant shear, $\dot{\gamma}_{loc}$ = $13s^{-1}$. In the upper left corner is the scattering patterns given by a BeAg sample taken as reference.

with characteristic scattering length identical to those shown at rest. Nonetheless an anisotropic to isotropic structures occurs. This transition corresponds to the gradual appearance of scattering rings rather than peaks shown in Fig.6.8 at t = $375s$ and t = $645s$. Upon further shear, the initial favored orientation of the lamellar structures characterized by higher scattering intensities at diametrically opposite positions of the scattering rings slowly vanish (see Fig.6.8 for t = $645s$ to t = $1185s$). Once the anisotropic to isotropic transition completed, the scattering patterns does not evolve anymore (see Fig.6.8 for t = $1455s$ to t = $1995s$) so that it can be inferred that the new structural organization remains stable in flow.

Let us now consider the scattering patterns of Fig.6.9 where the apparent local shear rate is fixed to a lower value, $\dot{\gamma}_{loc} \approx 3s^{-1}$. As expected, the scattering pattern obtained at rest ($t = 0s$), does not show significant difference with the one discussed in the previous paragraph. It even presents the same favored orientation of the initially plane lamellar structures.

Although unexpected, this initial orientation of the structures along a favored direction might result from the slight preshear experienced by the sample when loaded in the shear cell. Indeed, not only the initial orientation is the same along the probed radius, but it also corresponds to the favored orientation observed before the shear-induced transition discussed above (for example see Fig.6.8 for $t = 375s$).

As for higher apparent shear rates, the lamellar structures observed initially is conserved over the whole length time of the experiments. The characteristic scattering lengths corresponding to the different Bragg Peaks in Fig.6.9 are also the same as for $\dot{\gamma}_{loc} = 13s^{-1}$.

As for higher shear rates, a transition from anisotropic plane lamellar structures to isotropic lamellar ones is observed. However, as could be expected from our previous texture observations under cross polarized light, the transition process appears to be much slower than for higher shear rates. Indeed, whereas the first appearance of complete intense scattering rings occurred after shear times of $375s$ for $\dot{\gamma}_{loc} = 13s^{-1}$, a similar feature in the scattering patterns appears only after a shear time of $1680s$ for $\dot{\gamma}_{loc} = 3s^{-1}$.

It is noticeable here that both of the above scattering patterns, $t = 375s$ for $\dot{\gamma}_{loc} = 13s^{-1}$ (see Fig.6.8) and $t = 1680s$ for $\dot{\gamma}_{loc} = 3s^{-1}$ (see.Fig.6.9) almost correspond to the same applied apparent local strain, $\gamma = \dot{\gamma}_{loc}.t \approx 5000$.

These values of apparent local strain are consistent with those deduced from our previous birefringence texture observations. As a consequence, these results confirms that the transition observed at the microscopic scale result from

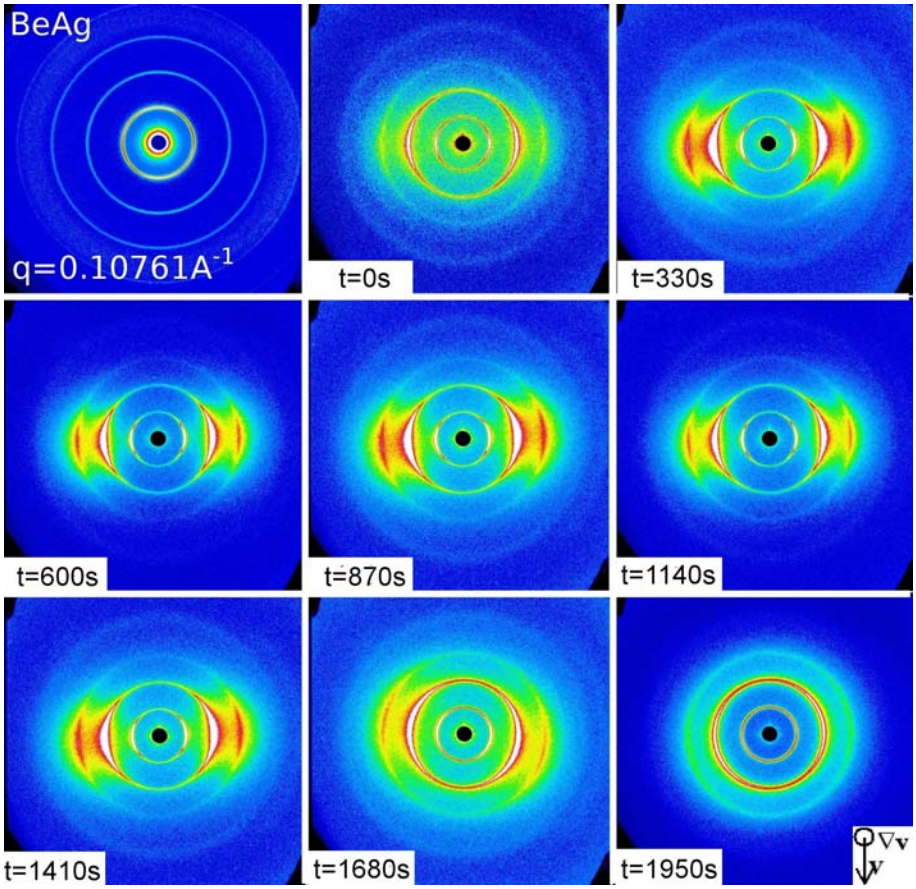

Figure 6.9: WAXS patterns temporal evolution upon application of a constant shear, $\dot{\gamma}_{loc} = 3s^{-1}$. In the upper left corner is the scattering patterns given by a BeAg sample taken as reference.

the shear induced formation of isotropic lamellar structures. Considering the anisotropic to isotropic transition and the lamellar nature of the structures formed either at rest or once a steady flow regime is reached, a transition from interconnected lamellar phase to lamellar vesicles is expected [1, 11, 14, 15]. Such lamellar vesicles are explicitly shown by freeze fracture transmission electron microscopy in Fig.6.10.

In spite of these important findings,a last question remains. the last point we have not yet considered concerns the stability of these shear-induced lamellar vesicles once the shear is stopped. Since no physical bondings other than those resulting from the amphiphilic properties of the AOT molecules are involved in

their formation, one could expect the material to recover its initial structures. Let us now discuss this point on the basis of freeze fracture transmission electron micrographs and birefringence textures observations.

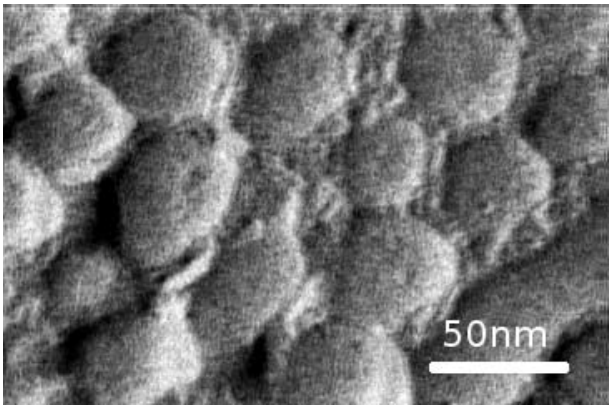

Figure 6.10: Freeze fracture electron micrograph of the shear-induced lamellar vesicles. The sample has been previously sheared for $30mins$ at an apparent shear rate of $10s{-}1$ prior to the preparation of the freeze fracture replica.

6.4.2 Stability of the Shear-Induced Structures

We have shown in the above sections that the lyotropic lamellar phase investigated in this piece of work undergoes a anisotropic to isotropic structural transition when sheared. The formation of lamellar vesicles is shown to be controlled by the level of strain experienced by the sample and to correspond to the appearance of grainy birefringence textures at the microscopic scale. When observed at a macroscopic scale, these texture appear isotropic (see Fig.6.5). One of the remaining question concerning these shear induced structures was either or not they remain stable once the shear is stopped.

We show in Fig.6.11 the evolution of the textures obtained at the end of the transition process (see Fig.6.5 for t = 2560s) once left at rest. The four pictures displayed in Fig.6.11 are taken after a waiting period t_w = 0, 20, 40 and 64 hours respectively.

The recovering process upon shear cessation is shown to be extremely slow. Indeed a comparison between the photograph taken just after shear cessation ($t_w = 0s$) and the one taken after 20 hours at rest does not show significant differences. After 40 hours spent at rest one can observed the development of brighter domains at the outer edge of the observation window. These domains slowly develop further as shown for t_w = 64hours. Nonetheless the major part of the observation window remains dark even after such long period spent at rest. This seems to indicates a relative stability of the shear induced lamellar vesicles.

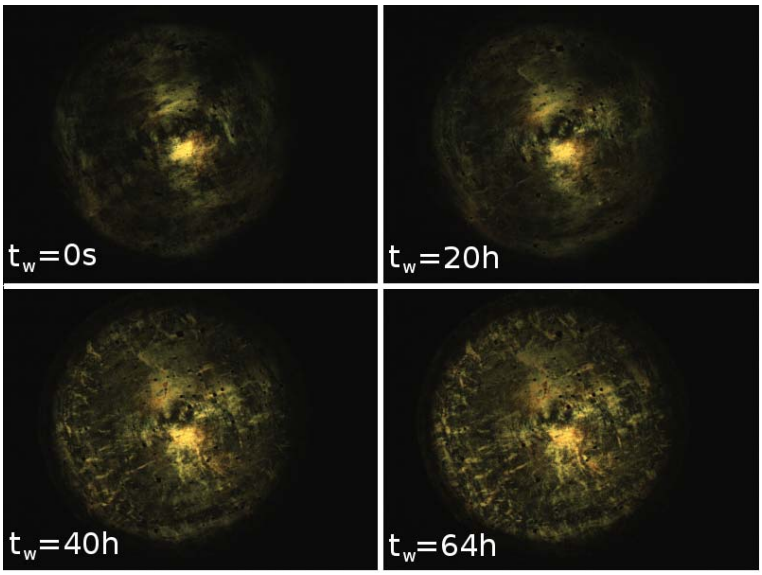

Figure 6.11: Photograph of the shear-induced phase observed under cross-polarized light after different waiting times after cessation of shear.

This relative stability of the shear induced structures is confirmed by freeze fracture electron microscopy performed on a previously sheared sample left at rest for nine hours. The corresponding micrograph in fig.6.12 indicates that the spheroidal shape of the structures is conserved at the nanoscopic scale while their size increases. Given the time scale of this recovering process, we haven't been able to investigate it further at this stage of the study.

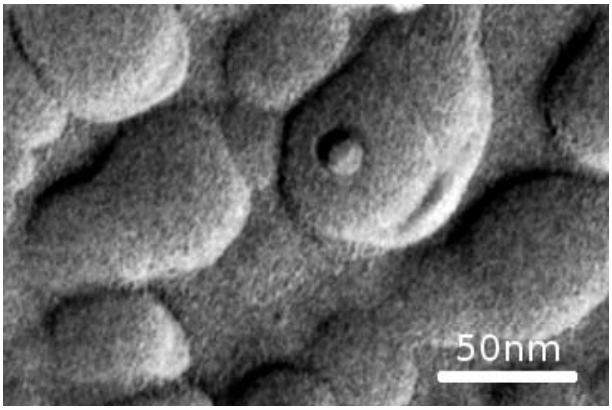

Figure 6.12: Freeze fracture electron micrograph of a previously sheared sample left at rest for 9 hours after flow cessation.

6.5 Conclusion

In this chapter we have focused on the structural properties of the investigated lamellar phases and the effects of shear at nanoscopic and microscopic scales. This has been done after three different experimental techniques.

At first, the microscopic effects of shear have been probed by means of flow birefringence texture analysis at the local scale. Monitoring the evolution of the textures as a function of shear time for different apparent local shear rates we show that the initially 'sheetlike' topological defects undergo a spacial reorganization leading to the formation of 'grainy' textured domains. The transition process from one type of textures to the other appears to be controlled by the level of strain experienced by the material while the final characteristic size of the grainy textures is in agreement with Frank's theory.

In a second section, we have focused on the global birefringence patterns within the parallel plate shear cell. This has allowed us to correlate the rheopectic transition investigated in the previous chapter with the shear induced microscopic reorganization of the topological defects within the studied material.

In the final section of this chapter, wide angle x-ray scattering results and freeze fracture electron micrograph are discussed. They show that the strain con-

trolled evolution of the topological defects within the sheared material originates from the formation of lamellar vesicles at the nanoscopic scales. At last the stability of these lamellar vesicles upon shear cessation is discussed.

The different experimental results shown and discussed in this chapter confirm earlier assumptions concerning the shear induced formation of lamellar vesicles in initially plane interconnected bilayers phases [9, 10, 12]. They also provide with the first explicit evidence of the effect of such a structural transition on the rheological properties of such defect rich lyotropic lamellar phase.

The above results together with those of the previous chapter have brought us important insights concerning the shear induced structural properties of defect rich lamellar phases and their consequences on their transient rheological properties. The rheological properties of the shear-induced phase are complex. They indeed strongly depend on the past shear history of a given sample as well as the time it is left to recover. Besides, depending on the level of stress they experience, the shear induced lamellar vesicles phases exhibit either 'solid-like' or 'liquid-like' behaviour [2, 20–22]. Let us now concentrate on the characterization of these shear-induced viscoelastic properties.

References

[1] H. Hoffmann, C. Thunig, U. Munkert, H.W. Meyer, and W. Richter. From vesicles to the l_3 (sponge) phase in alkyldeimethylamine oxide/heptanol systems. *Langmuir*, 8:2629–2638, 1992.

[2] B.D. Simons and M.E. Cates. Vesicles and onion phases in dilute surfactant solutions. *Journal de Physiques II France*, 2:1439–1451, 1992.

[3] O. Diat, D. Roux, and F. Nallet. Effect of shear on a lyotropic lamellar phase. *Journal de Physique II France*, 3:1427–1452, 1993.

[4] O. Diat and D. Roux. Layering effect in a sheared lyotropic lamellar phase. *Physical review E*, 51:3296–3299, 1995.

[5] J. Bergenholtz and N.J. Wagner. Formation of aot/brine multilamellar vesicles. *Langmuir*, 12:3122–3126, 1996.

[6] P. Panizza, A. Colin, C. Coulon, and D. Roux. a dynamic study of onion phases under shear flow: size changes. *European Physics Journal B*, 4:65–74, 1998.

[7] A. Leon, D. Bonn, J. Meunier, A. Al-Kahwaji, and O. Greffier andH. Kellay. Coupling between flow and structure for a lamellar surfactant phase. *Physical Review Letters*, 84:1335–1338, 2000.

[8] A.S. Wunenburger, A. Colin, T. Colin, and D. Roux. Undulation instability under shear: A model to explain the different orientations of a lamellar phase under shear. *The european physical journal E*, 2:277–283, 2000.

[9] L. Courbin, J.P. Delville, J. Rouch, and P. Panizza. Instability of a lamellar phase under shear flow: Formation of multilamellarvesicles. *Physical Review Letters*, 89(14):148305(1) – 148305(4), 2002.

[10] L. Courbin and P. Panizza. Shear-induced formation of vesicles in membrane phases: Kinetics and sizeselection mechanisms, elasticity versus surface tension. *Physical Review E*, 69(2):021504(1) – 021504(12), 2004.

[11] B.A. Coldren, H.E. Warriner, R. Van zanten, J.A. Zasadzinski, and E.B Sirota. Lamellar gels and spontaneous vesicles in catanionic surfactant mixtures. *Langmuir*, 22:2465–2473, 2006.

[12] A. Moldonado, R. Ober, T. Gulik-Krzywicki, W. Urbach, and D. Langevin. The sponge phase of a mixed surfactant system. *Journal of Colloid and Interface Science*, 308:485–490, 2007.

[13] H. Warriner, H.J. Idziak, N.L Slack, P. Davidson, and C.R. Safinya. Lamellar biogels: Fluid-membrane-based hydrogels containing polymer lipids. *Science*, 271:969 – 973, 1996.

[14] S.L. Keller, H.E. Warriner, C.R. Safinya, and J.A. Zasadzinski. Direct observation of a defect-mediated viscoelastic transition in a hydrogelof lipid membranes and polymer lipids. *Physical Review Letters*, 78:25, 1997.

[15] H. Warriner, P. Davidson, N.L Slack, M. schellhorn, P. Eiselt, H.J. Idziak, H.W Scmidt, and C.R. Safinya. Lamellar biogels comprising fluid membranes with a newly synthesized class of polyethylene glycol-surfactant. *Journal of Chemical Physics*, 107(9):3707–3722, 1997.

[16] R.G. Larson and D.W. Mead. Development of orientation and texture during shearing of liquid-crystalline polymers. *Liquid crystals*, 12(5):751–768, 1992.

[17] G Marrucci. Rheology of liquid crystalline polymers. *Pure and Applied Chemistry*, 11:1545 – 1552, 1985.

[18] R.G. Larson. *The structure and rheology of complex fluids*. topics in chemical engineering. Oxford University Press, New York, 1999.

[19] G. Kiss and R.S. Porter. Rheo-optical studies of liquid-crystalline solutions of helycal polypeptides. *Molecular Crystals and Liquid Crystals*, 60:267, 1980.

[20] O. Roblez-Vasquez, S. Corona-Galvan, J.F.A Soltero, and J.E. Puig. Rheology of lyotropic liquid crystals of aerosol ot ii.high concentrationsregimes. *Journal of Colloid and Interface Science*, 160:65–71, 1993.

[21] O. Robles-Vasquez, J.F.A Soltero, J.E. Puig, and O. Manero. Rheology of lyotropic liquid crystals of aerosol ot. iii. effect of salt and hydrocarbons. *Journal of Colloid and Interface Science*, 4163:432–436, 1994.

[22] P. Panizza, D. Roux, V. Vuillaume, C.Y.D Lu, and M.E. Cates. Viscoelasticity of the onion phase. *Langmuir*, 12:248–252, 1996.

Chapter 7

Aging and Yielding in Sheared Lamellar Phases

Contents

Résumé du Chapitre 7

Dans ce dernier chapitre nous étudions les propriétés viscoélastiques d'une phase de vesicules lamellaires induite sous cisaiilement.

Pour ce faire, nous utilisons une procédure basée sur des mesures successives en rhéométrie à contrainte imposée. Notre méthode présente un double avantage. Elle permet d'une part de maîtriser totalement l'histoire en cisaillement de l'échantillon et donc d'assurer la reproductibilité des résultats. Et d'autre part, l'analyse des oscillations de la déformation résultant du couplage inertio-elastique au début de chaque saut de contrainte nous permet de déterminer les paramètres viscoélastiques instantanés du matériau à l'aide du modèle de Maxwell-Jeffrey.

Une fois notre procédure validée par l'obtention d'un état stable de référence, nous étudions l'effet de différents paramètres tels que le temps passé au repos et le comportement en fonction de la contrainte appliquée.

Ces résultats montrent que contrairement à la plupart des matériaux dits 'vieillissants' la viscosité et l'élasticité des phases de vésicules lamellaires tendent à diminuer avec le temps passé au repos. Ce résultat s'explique à l'aide d'observation des structures formées au sein de l'échantillon dans le régime permanent d'ecoule-ment puis de leur évolution lors de la relaxation du matériau.

Enfin dans une dernière partie nous nous focalisons sur le phénomène de fluage au sein des phase de vesicules lamellaires. Nous montrons que celui-ci est controllé par le niveau de la contrainte de précisaillement, du temps de relaxation et du niveau de contrainte auquel est soumis l'échantillon.

7.1 Introduction

Materials of industrial importance such as suspensions, physical gels, foams, wet granular materials or emulsions form networks of interacting elements in given conditions. Despite their extremely diverse microscopic structures, all these materials present quite similar flow properties. Indeed, they can display liquid-like or solid-like behaviours according to the shear stress they experience. Roughly, when the applied stress is small enough, they behave like elastic solids, while they flow like liquids when the applied stress is sufficiently high. Those everyday life materials: paints, foods, cosmetics.., are therefore called "yield stress fluids".

From this binary description, simple models can be built around the yield stress concept, such as the Bingham or Herschel Bulkley models. However, those models are conceptually challenging as even the simple existence of a yield stress has been at the center of a long-lived controversy, as can be seen in reviews and articles [1–5]. However, it was shown recently that the heart of the controversy seems to lie in the definition of what is a steady state flow and its strong dependence of the experiment duration [6]. In consequence, the aim of the present paper is to investigate experimentally, as thoroughly and rigorously as possible, the influence of time and shear history on the viscoelastic properties of a single, well characterized soft material.

As Barnes et al. have mentioned [1, 2], measurements of the viscoelastic properties of a materials exhibiting yielding is far from being straightforward. Worse, as mentioned in the recent article of Yao et al. [7] the standard methods such as large amplitude oscillatory measurements used to determine the non linear viscoelasticity of such materials, are *de facto* simple extensions of linear methods, and therefore strongly questionable.

Besides, because they are also steady state methods, the stress/deformation history of a given thixotropic material and its slow evolution strongly affect the measurements [8–12]. In other words, two samples of identical chemical composi-

tion can exhibit different behaviors depending on the time they have spent at rest or the way they have been loaded in the shear cell. Luckily an original method, coined as "inertio-elastic oscillations" which uses the coupling between the inertia of controlled stress rheometers and viscoelasticity has recently been devised that allows to perform such measurements without the above drawbacks [7, 13, 14].

This method is used on a complex soft material made of docusate sodium salt (AOT), Iso-Octane and water. The ambivalent hydrophilic and hydrophobic properties of the surfactant molecule (AOT) confer them the ability to self assemble in presence of a polar solvant (water) and an apolar solvant (isooctane). Aerosol OT (AOT) is an anionic surfactant which is well known to formed reversed micelles in isooctane [15]. The hydrophilic and hydrophobic balance of AOT lends to solubilize it either in water or isooctane [16]. Previous studies [15, 16] have shown at low apolar solvant concentration, on a water line dilution, a structure evolution from a hexagonal to a lamellar liquids crystallines phases.

When sheared the lamellar liquid Crystal phase can form lamellar vesicles with a size controlled by the applied shear rate [17, 18]. More recently the dynamic of the shear creation have been studied using polarized light microscopy and viscosity measurements. The slow emergence of vesicles during the shearing process have been correlated to a strong increase in the viscosity [19–21]. To explain this unexpected rheopectic behaviour hydrodynamic instabilities of lamellar membranes are invoked with often the coupling of topological defects [22–24].

In this study we investigate aging, relaxation and solid to fluid transition in an AOT / Iso-octane / Water ternary lyotropic system forming interconnected bilayers at rest and lamellar vesicles when sheared [20, 21, 25, 26]. Using a reliable creep flow procedure we show that a steady and reproducible state can be reached after an adequate and also reproducible transient regime. A detailed description of this procedure is given in the following sections of this manuscript. Then, using the inertial coupling between the investigated sample and the rotating head of the rheometer [8, 13, 27–29] allows us to determine the effects of aging and

rejuvenation on the viscoelastic properties of the investigated sample. Here, the term 'aging' refers to the slow evolution undergone by the studied sample under a given range of applied stresses. The term 'rejuvenation' refers to the capacity of the investigated material to 'forget' its past stress/strain history through the application of a given reference stress and that way to recover a steady state of reference.

7.2 Experimental Setup

To prevent any scattering of our experimental data due to the use of different batches, a large amount of sample is prepared as follows. 99% and 99.9% respectively pure AOT and Iso-octane are supplied by Sigma-aldrich and used without further purification. The desired amount of active matter and apolar solvent are weighted and mixed with the desired amount of double-distilled and deionized water ($18M\Omega.cm$) using a magnetic stirrer for one day. Once an homogeneous mixture is obtained it is centrifugated for $45mins$ at $2500rpm$ to remove any remaining air bubbles. The solution is then kept in a tightly closed container to prevent any possible evaporation.

Creep measurements are performed on an ARG2 stress controlled rheometer (TA Instruments) using especially designed PMMA Cup and Bob geometries. The dimensions of the inner and outer cylinder were as follows: R_{inner} = $22mm$, R_{outer} = $24mm$ and H = $90mm$. All measurements are performed with a solvent trap so that no measurable effects of evaporation can be detected over the measurement time. Coating another cup and bob geometry with sand paper of different roughnesses and using a smooth PMMA shear cell, we have checked that no significant differences if any at all could be observed on our data set. It can therefore be inferred that the sample does not slip on our PMMA geometry surfaces whereas it does on titanium geometry surfaces. Such precautions make it possible to define a reliable experimental procedure allowing to check the re-

producibility of the experimental results.

The micrographs of Fig.7.1(a), Fig.7.1(c) and Fig.7.12 are obtained with a Transmission Electron Microscope CM200 CRYO Phillips after two different techniques. In Fig.7.1(a), the sample forms a stretched film within the holes of a lacey carbon film 300 mesh grid. It is then frozen in liquid ethane and kept in a refrigerated sample holder while observed in CRYO-TEM at 120KV. The freeze fractures micrograph shown in Fig.7.1(c) and Fig.7.12 are prepared as follows. The sample is loaded between two semi-hollow cups forming a sandwich. At first this sandwich, is plunged in pasty nitrogen ($T \approx -200\ C$). It is then loaded in a Reichert Jung cryofract in which it is opened. Both faces of the fractures are then shaded with platinum at 45 before a carbon layer is deposited at normal incidence. The replicas are recovered at room temperature by specimen dissolution in iso-octane and in water, then collected onto a 600HH mesh grid prior to be observed in TEM at 120KV.

Finally, small angle X-ray scattering under shear experiments have been performed recently at the European Synchrotron Radiation Facility (ESRF) on the 'D2AM' french beamline. To do so, the sample is loaded in an especially designed polycarbonate parallel plates shear cell (gap $h = 2mm$) of which the angular velocity, ω, is controlled. The position of the shear cell is precisely controlled so that the X-ray beam passes through the sheared sample in the direction perpendicular to the plates at a controlled distance, r, from the cell centre. The results shown in what follows are therefore obtained for a controlled local shear rate, $\dot{\gamma}_{loc} = r\omega/h = 3s^{-1}$. Fixing the integration time to $10s$, the resulting scattering spectrum are then recorded by a CCD camera.

7.3 Material Structural Properties

Surfactant molecules such as docusate sodium salt (AOT) have the ability to form structures when mixed with a polar solvent such as water and an apolar one such

as 2-2-4 trimethylpentane (Iso-octane). Depending on the concentration of each components the resulting nano-aggregate is constituted by cylindrical, plane or spherical preferential forms. In certain conditions of concentration, these different favored structures order themselves to form lyotropic liquid crystal phases.

The concentrations in AOT (28.5%), water (66.5%) and iso-octane (5%) considered in this piece of research lead to the formation of interconnected anisotropic bilayers at rest as it is shown after cryo-TEM technique in Fig.7.1(a). Indeed, the latter shows interconnected white threads compounded by stacked bilayers of approximately $5.9nm$ explicitly shown in the inset of Fig.7.1(a).

The anisotropic lamellar nature of the sample when left at rest for significant period of time is confirmed by WAXS measurements. Indeed as expected from bilayer forming phases [30] the scattering pattern in Fig.7.1(b) prior to shear ($t = 0s$) shows three Bragg peaks at scattering lengths $q_0 \approx 0.11\dot{A}^{-1}$, $2.q_0$ and $3.q_0$. These values of q_0 correspond to bilayers spacing of approximately $5.7nm$ in good agreement with the value determined after transmission electron microscopy.

Previous studies on similar lyotropic lamellar phases either at lower surfactant concentration or with addition of counter-ions [20, 21, 25] have shown that such phases have a propensity to undergo structural evolution when sheared with the formation of lamellar vesicles. In a recent study of the transient flow regimes of the system investigated here [26] we have shown that a permanent flow regime is reached after a rheopectic transition (*ie.* an increase of the viscosity upon application of constant shear) similar to those observed during the formation of lamellar vesicles in other lyotropic lamellar phases [20, 21].

The shear induced formation of such lamellar vesicles in this system is confirmed either by WAXS experiments under shear or freeze fracture electron microscopy. As shown in Fig.7.1(b) the anisotropic interference patterns observed at rest in WAXS experiments evolves toward an isotropic pattern when the sample is sheared for $1950s$ at $\dot{\gamma}_{loc} = 3s^{-1}$. That is, the initial peaks shown for $t = 0s$ are replaced by scattering rings at the same characteristic scattering lengths. This

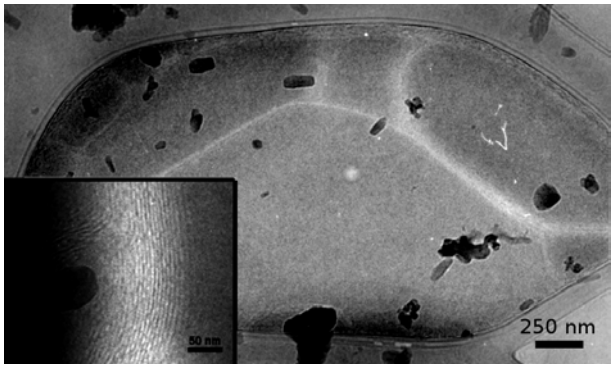

(a)

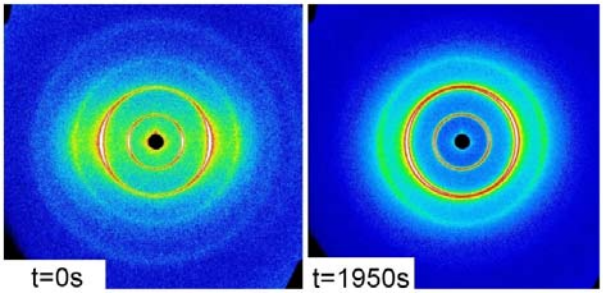

(b)

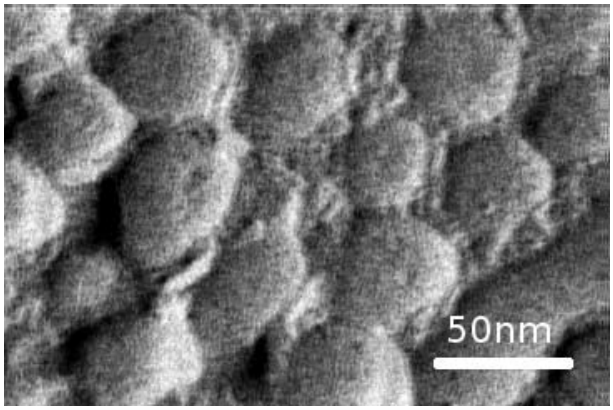

(c)

Figure 7.1: (a) Cryo-TEM micrographs of the investigated material at rest. The inset is a close-up view of the interconnected structures in the main pictures showing stacked lamellar structures. (b) WAXS patterns prior (t = 0s) and after (t = 1950s) application of a local shear rates of $3s^{-1}$ for 1950s. (c) Freeze fracture transmission electron micrograph of a recently sheared sample

is indeed expected in material in which lamellar vesicles are formed as explicitly shown after freeze fracture TEM in Fig.7.1(c).

The formation of lamellar vesicles in sheared lyotropic lamellar phases is a reversible process [25]. Nonetheless, such structures are found to remain relatively stable in the mixture for hours or even days [21, 25]. The initial organization of the bilayers is indeed only regained after an extremely slow relaxation process [25]. In the following, we define an experimental measurement procedure allowing to obtain reproducible measurements concerning the yielding and aging rheological properties of such complex structured phases.

7.4 Creep Measurements Procedure

7.4.1 Steady State of Reference and Reproducibility

Since the studied material is strain/stress history dependent [26], a reliable method allowing to control the different parameters affecting its rheological properties has to be chosen. To do so, creep flow measurements (*ie.* measuring the sample deformation induced by a constant applied shear stress) have been performed following the procedure displayed in Fig.7.2.

During a first step referred here as 'sample initialization', the sample is 'rejuvenated' through the application of a constant stress $\sigma_{init} = 10Pa$, long enough for a macroscopic steady state to be reached. The determination of this initialization time ($T_{init} = 2700s$ here) is discussed later in this paper. Each pre-shear is followed by a recovery time ($T_w = 900s$ here) and both are repeated three times. The experimental results of the three first initialization steps and their following recovery tests are displayed in Fig.7.3(a) and Fig.7.3(b) respectively.

In both Fig.7.3(a) and Fig.7.3(b), the sample pre-shear and recovery deformations of initialization step 1 differ from initializations steps 2 and 3 while

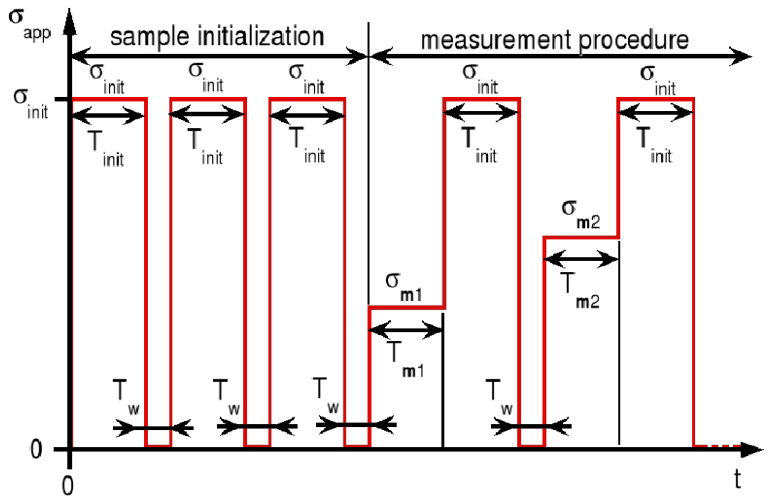

Figure 7.2: Applied creep flow procedure, σ_{init} and T_{init} are respectively the applied pre-shear stress and the time during which it is applied, T_w is the time during which the sample is left at rest after being pre-sheared and σ_{mi} and T_{mi} are respectively the applied stress and the duration of the measurement step i.

the later two are perfectly identical. This difference is easily explained if one considers the sample previous history at the start-up of each step. Indeed, at the start-up of the first pre-shear step, the sample shear history is a priori unknown since it has spent some time at rest and just has been loaded in the shear cell. As a consequence its shear history dependent internal structure is in an unknown state between interconnected bilayers or lamellar vesicles. Nonetheless, as shown in the inset of Fig.7.3(a) an apparent steady viscosity corresponding to a linear increasing of the strain with the time of shear is eventually reached after a complex transient regime during which lamellar vesicles are formed. On the other hand, given that T_{init} has been chosen adequately (*ie.* long enough for the sample to reach its macroscopic and microscopic steady states [26]), the sample is in the same controlled reference state at the start-up of initialization steps 2 and 3. As a consequence, no significant differences if any at all can be observed on the corresponding curves of Fig.7.3(a) and Fig.7.3(b).

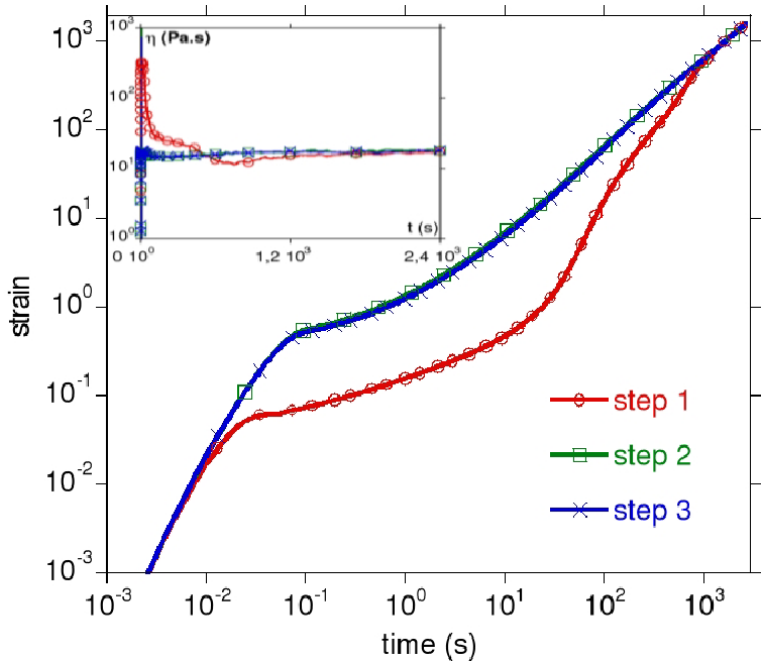

(a) Initialization preshear steps

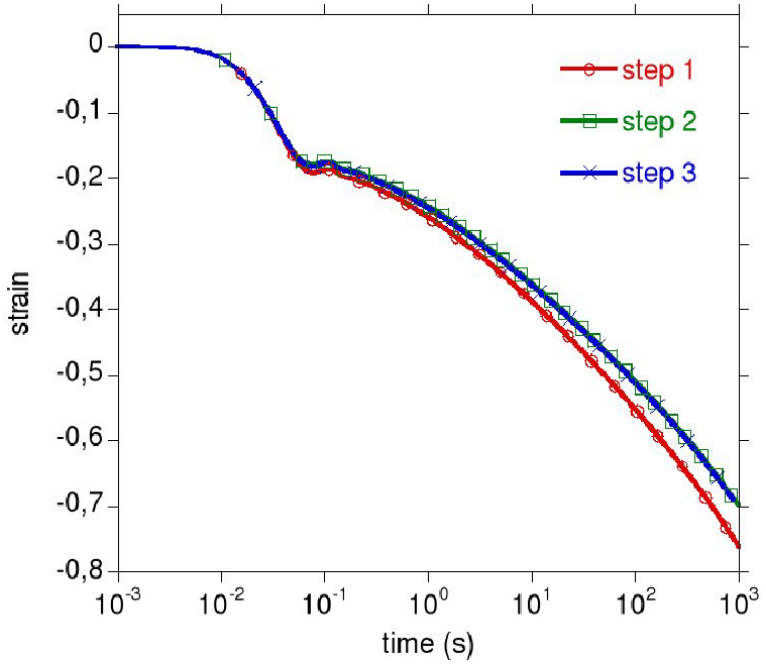

(b) Initialization recovery steps

Figure 7.3: Strain as a function of time during the sample initialization, the inset in Fig.7.3(a) shows the evolution of the sample viscosity on a lin-log scale.

Although time consuming when compared to the usual pre-shear procedure [8, 11, 31], this modified version of the procedure used by Cloitre *et al.* [12] present four important assets. (i) it ensures that the sample which is probed in the second phase of the experiments (see 'measurement procedure' in Fig.7.2) is in a controlled and reproducible steady state taken as a reference. (ii) Both aging and rejuvenation process are probed as functions of the previous stress history. (iii) The reproducibility of the data is checked throughout the whole measurements procedure. (iv) The effects of each parameter σ_{init}, T_{init}, T_w and σ_m on the material viscoelastic properties can be probed independently of the others.

7.4.2 Determination of the Initialization Time, T_{init}

As mentioned above, the determination of an adequate value of T_{init} is fundamental if one wants to ensure the reproducibility of its experimental results. In order to determine the pre-shear time T_{init} necessary to obtain a controlled and reproducible reference state of the studied sample, a procedure similar to the 'measurement procedure' described in Fig.7.2 is used. The difference being that all parameters but T_{init} are kept constant : $\sigma_{init} = 10Pa$, $T_w = 900s$, $\sigma_m = 0.2Pa$ and $T_m = 900s$. The strain curves obtained during recovery and measurements steps for various values of T_{init} are respectively displayed in Fig.7.4(a) and Fig.7.4(b).

As shown in these figures, changing the length of the preshear from $600s$ to $1200s$ and then to $2700s$ gives significantly different strain curves either during recovery or creep flow at low constant stress. These differences indicate that although an apparent steady state resulting from the sample transformation seems to be reached after a $600s$ pre-shear (see inset of Fig.7.3(a)) values of T_{init} lower than $2700s$ cannot be considered sufficient to induce a controlled reference state, the sample transformation being not completed at all scales. Nonetheless, upon further increasings of T_{init} from 2700 to $7200s$, all the curves obtained during

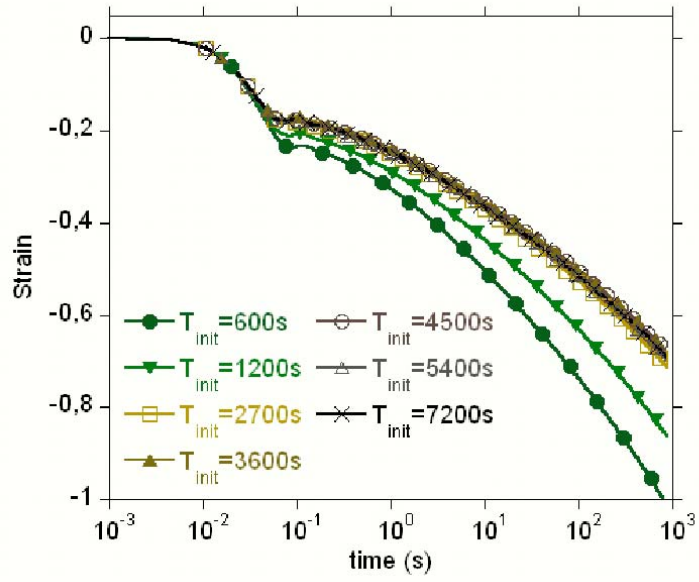

(a)

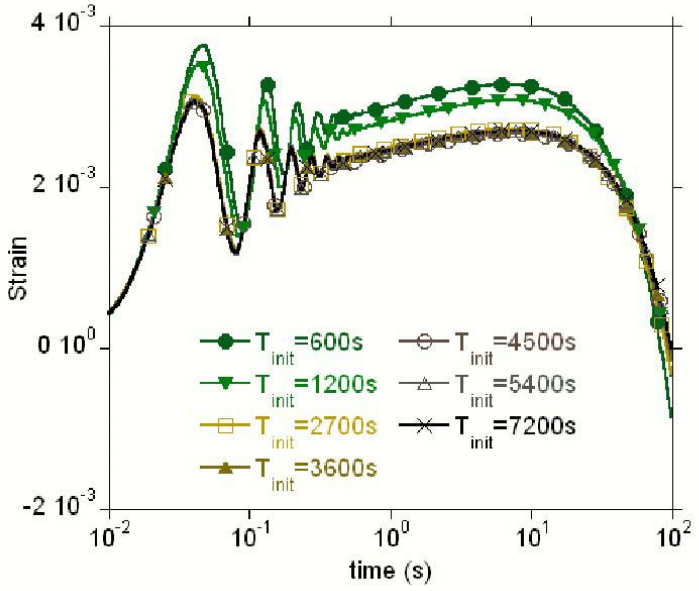

(b)

Figure 7.4: Strain evolution as a function of time during recovery steps [Fig.7.4(a)] and subsequent application of a constant stress σ_m = $0.2Pa$ [Fig.7.4(b)] obtained after initialization steps of different durations.

recovery and measurement steps appears to be superimposed. These qualitative observation indicates that pre-shear time of at least $2700s$ have to be considered if one wants to ensure that the sample reaches a steady and reproducible state of reference. Since the analysis of any of the experimental data shown in this study would not be meaningful unless the obtainment of such a reference state was verified and controlled, all subsequent measurements have been performed after having pre-sheared the sample at $10Pa$ for $2700s$.

Until now, only reproducibility and obtainment of an out-of-equilibrium steady state during the initializations steps have been considered. However the strain curves displayed in Fig.7.4(b) deserve several additional comments. All the displayed curves are obtained with an applied stress σ_m = $0.2Pa$ below the apparent yield stress. One observes free damped oscillations at the start-up of the measurements. These free damped oscillations are a consequence of inertial coupling between the viscoelastic sample and the moving part of the shear cell [8, 13, 27–29]. As explained later in this paper, fitting these free damped oscillations with theoretical models makes it possible to determine viscoelastic parameters accounting for the studied sample rheological behavior. Following these oscillations, a slow increasing of the strain is observed. Then, it eventually reaches a maximum and starts to decrease toward negative values so that at long-time the deformation is apparently in the opposite direction of the applied stress. Similar experimental observations are mentioned by Coussot *et al.* [8] and Cloitre *et al.* [12] on other soft-jammed systems. In these publications, this long time decreasing of the strain is attributed to the slow relaxation of internal stresses stored during the pre-shear.

7.4.3 Inertial Coupling in Creep Flow Measurements

As mentioned above, the free damped oscillations one can observe in Fig.7.4(b) but also at a lesser degree in Fig.7.4(a) at the start-up of each step are a conse-

quence of the inertial coupling between the studied viscoelastic sample and the moving part of the shear cell. Based on previous studies [13, 27–29] these free damped oscillations can be used to determine the viscoelastic properties of the investigated material provided that they can be accounted for by a model. The complete and detailed resolution of the coupling equation governing the motion of the mobile part of the apparatus for different model materials can be found in the previously mentioned publications. As an instance, Baravian and Quemada [13] give *eq.* (7.1) of the strain induced by the application of a shear stress step σ_0 on a Maxwell-Jeffrey viscoelastic material (see Fig.7.5 and *eq.* (7.2) for its governing equation).

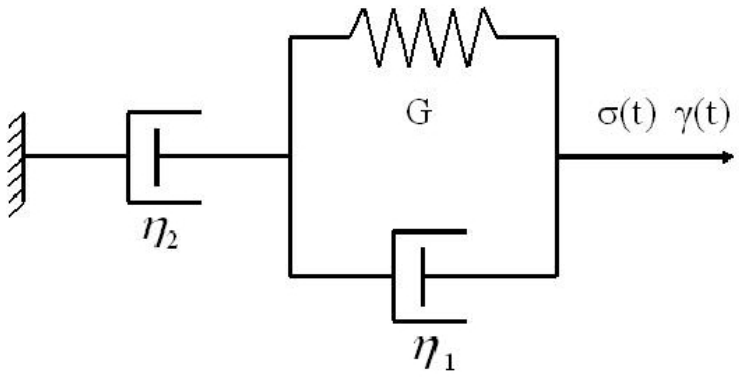

Figure 7.5: Schematic view of a Maxwell-Jeffrey viscoelastic material. The relation between $\sigma(t)$ and $\gamma(t)$ is given in *eq.* 7.2.

$$\begin{aligned}\gamma(t) = \quad & \sigma_0 \left[\frac{t}{\eta_2} - B + e^{-At} \left[B cos\left(\omega t\right) \right.\right. \\ & \left.\left. + \frac{A}{\omega} \left(B - \frac{1}{A\eta_2} \right) sin\left(\omega t\right) \right] \right]\end{aligned} \tag{7.1}$$

$$\left(\eta_1 + \eta_2\right) \dot{\sigma} + G\sigma = \eta_2 G \dot{\gamma} + \eta_1 \eta_2 \ddot{\gamma} \tag{7.2}$$

In *eq.* (7.1), A, B and ω are defined as functions of the Maxwell-Jeffrey model parameters, G, η_1 and η_2 as given in *eq.* (7.3). In the later, α is a factor accounting for the inertia of the moving part of the shear cell as well as for the proportionality relations between the shear rate and the measured angular

velocity on one hand and the shear stress and the applied torque on the other hand.

$$\begin{aligned} A &= \frac{\alpha G+\eta_1\eta_2}{2\alpha(\eta_1+\eta_2)} \\ B &= \frac{\alpha(\eta 1+\eta_2)}{\eta_2 G}\left(\frac{2A}{\eta_2}+\frac{1}{\alpha}\right) \\ \omega &= \sqrt{\frac{\eta_2 G}{\alpha(\eta_1+\eta_2)}-A^2} \end{aligned} \tag{7.3}$$

As shown in the inset of Fig.7.6, the Maxwell-Jeffrey model fit very well with the experimental data at the start-up of each measurements steps. However, the model and experimental curves appears to differ once the time-window used to determine the Maxwell-Jeffrey parameters exceeds $150ms$. Nonetheless, it is observed that for all the data set presented in this study, the fitted solvent viscosity of the Maxwell-Jeffrey model, η_2, is at least one order of magnitude greater than the polymeric viscosity η_1. Under this condition, the expression of A and ω given in *eq.* (7.3) can be reduced to *eq.* (7.4) [13].

$$\begin{aligned} A &\approx \frac{1}{2}\left(\frac{G}{\eta_2}+\frac{\eta_1}{\alpha}\right) \\ \omega &\approx \sqrt{\frac{G}{\alpha}-A^2} \end{aligned} \tag{7.4}$$

The later two expressions makes it possible to obtain good approximations of the elastic modulus by analysis of the frequency of the oscillations especially if, as it is the case on the system studied here, the condition $\frac{G}{\alpha} >> A^2$ is verified. Besides, given the excellent agreement between the fitted theoretical model and the experimental data on the considered time-window, it can be assumed that the obtained values of η_1 and η_2 qualitatively account for the studied sample rheological properties.

To exemplify the usefulness of the model presented above, it is applied to the strain curves (see Fig.7.4(b)) presented above. The fitted values of the apparent elastic modulus corresponding to various pre-shear times are displayed in Fig.7.6. This allows to quantitatively confirm the observations made in the previous section concerning the pre-shear time. Indeed, whereas the elastic modulus

is found to depend on T_{init} for values lower than $2700s$, it remains constant as soon as T_{init} becomes long enough for the sample to reach its macroscopic steady state. Besides no significant differences are observed depending if one takes into account or not the simplifications $\eta_2 >> \eta_1$ and $\frac{G}{\alpha} >> A^2$. As a consequence, it can be assumed that the later hypothesis are verified in this study.

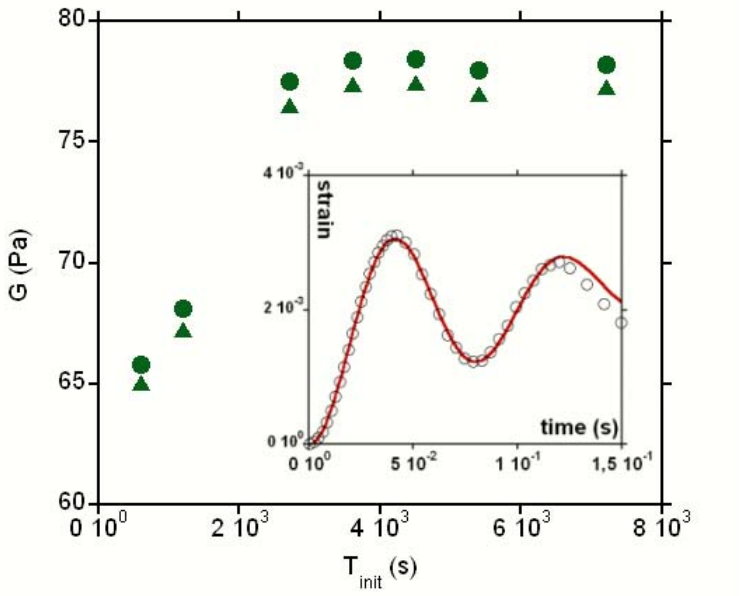

Figure 7.6: Fitted values of G as a function of T_{init} with (triangles) and without (circles) the hypothesis $\eta_2 >> \eta_1$ and $\frac{G}{\alpha} >> A^2$. σ_{init} = $10Pa$, T_w = $900s$ and σ_m = $0.2Pa$. In the inset, the straight lines corresponds to the Maxwell-Jeffrey model (eq.7.1) fitted to the experimental data obtained for T_{init} = $2700s$

7.5 Results

The procedure described in the previous section enable us to control the sample macroscopically. It ultimately results in the definition of a reference state, one can simply obtain by pre-shearing the sample for $2700s$ at $10Pa$. Once the sample is in a reference state, it may be submitted to a recovery or a creep experiment. In

the following sections we first investigate the rheological properties as a function of the time of rest T_w. Then, in a second section, the time of rest following the pre-shear is fixed and the effect of the applied stress magnitude σ_m on the short and long time rheological behavior of the probed material is analysed.

7.5.1 Effect of the Resting Time: T_w

In order to characterize the effect of T_w on the sample rheological properties, the procedure defined above (see Fig.7.2) is used. In these creep measurements, T_w is the variable parameter and $\sigma_m = 0.2Pa$ is chosen below the apparent yield stress (*ie.* σ_m is chosen small enough to observe strain saturation for all tested T_w). The different tested T_w corresponding to different level of strain recovery after pre-shear are displayed in Fig.7.7. The inset in the later shows that, even after 24 hours spent at rest, the relaxation of the internal stresses stored during the pre-shear is not completed. In term of experimental time, this makes it almost impossible to investigate a sample at thermodynamic equilibrium.

Following recovery steps of various time lengths evolving from $60s$ to $10800s$ (see Fig.7.7), creep steps are performed. The corresponding strain curves are shown in Fig.7.8. As shown in Fig.7.7, after cessation of the pre-shear, the sample first undergoes a fast recovery 'regime' followed by a slower one. The transition from one regime to another is not well defined. Nonetheless, the strain rate is several order of magnitude lower for $T_w = 1200s$ than for $T_w = 1s$ while it only decreases of one order of magnitude afterward. Thence, it can be assumed that the recovery process is in its slow regime for T_w values above $1200s$. In Fig.7.8, the start-up of each strain curves shows free damped oscillations with an amplitude and a frequency depending on T_w. These oscillations are followed by a slow increasing of which the duration depend on T_w. Then, it eventually saturates and starts to decrease toward negative values. Such negative values of strain are disconcerting at first sight. Nonetheless, one has to keep in mind that

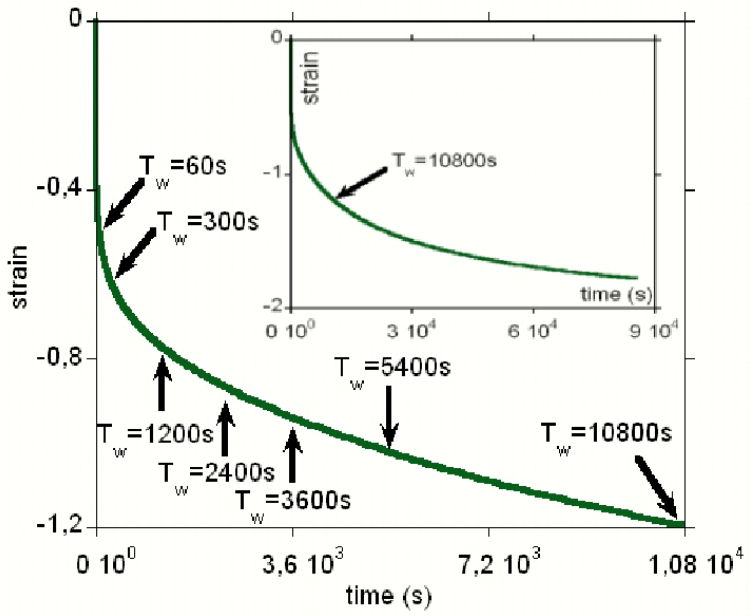

Figure 7.7: Strain recovery after a pre-shear at $10Pa$ for $2700s$. Arrows indicate the different T_w considered in this section. The inset shows that no finite strain is attained after $24hours$.

the measured strain is set to zero at the start-up of each step of the procedure and that the sample relaxation is not completed when the measurement steps begins. Besides, the applied stress is chosen below the apparent yield stress so that the initial structures at the start-up of the measurement step does not break. Consequently the sample only undergoes a finite deformation. Finally, it can be noticed that the level of deformation in Fig.7.8 is two order of magnitude lower in absolute values than in Fig.7.7. Thence, application of stresses as low as the one applied here can be considered as a perturbation of the relaxation process on the considered time-scale. At last, since the relaxation process slows down with the time of rest T_w (see Fig.7.7), it can be expected that the time at which the strain starts to decrease increases with the time of rest as shown in Fig.7.8.

Like for the determination of adequate values of T_{init}, the first $150ms$ of the curves shown in Fig.7.8 can be fitted with the Maxwell-Jeffrey model described above. The evolution of the apparent elastic modulus with the time T_w for given

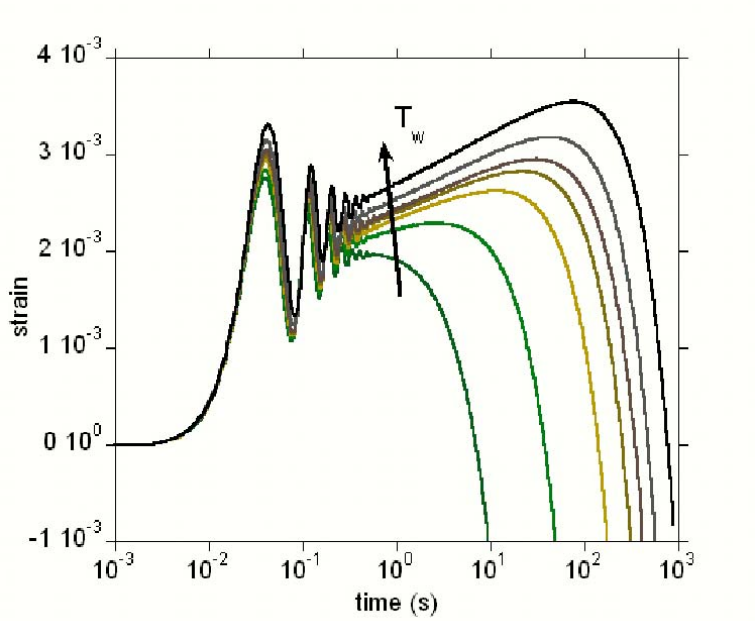

Figure 7.8: Evolution of the strain under application of a constant stress, σ_m = $0.2Pa$, following recovery steps of various time lengths. T_w = $60, 300, 1200, 2400, 3600, 5400$ and $10800s$ from bottom to top respectively.

pre-shear conditions can therefore be probed.

7.5.2 Aging and Solid to Liquid Transition

As shown in the previous sections by Fig.7.3(a) and Fig.7.8 respectively, the AOT/Water/Iso-octane mixture investigated in this study behave either as a liquid or a solid depending on the applied level of stress. The transition from one behavior to the other can be followed using the creep procedure described in Fig.7.2. To do so, all the controlling parameters are fixed to adequate values: σ_{init} = $10Pa$,T_{init} = $2700s$,T_w = $900s$, while σ_m is varied between the reference stress σ_{init} and the lower technically accessible stress σ_m = $0.2Pa$ here. The strain curves corresponding to the application of such different stresses after a

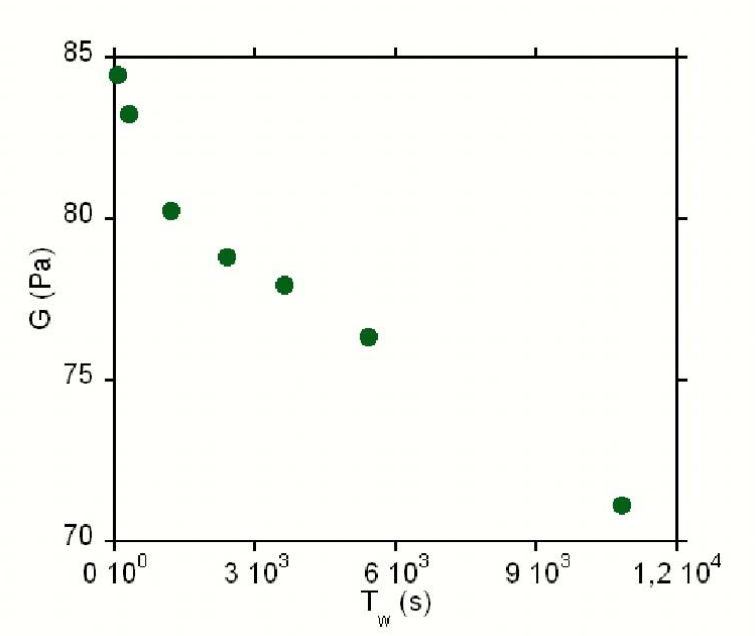

Figure 7.9: Fitted values of G as a function of T_w after a pre-shear at $10Pa$ for $2700s$.

pre-shear of $10Pa$ for $2700s$ and a recovering period of $900s$ are shown in Fig.7.10.

Considering first the 'long-time' behavior of the investigated material , the strain curves in Fig.7.10 show different trends corresponding to a transition from a 'solid-like' to a 'liquid-like' behavior with increasing σ_m. For lower stresses ($\sigma_m \leq 1Pa$), the strain eventually saturates after a slow increase and starts to decrease toward negative values. As shown in the previous section, such a behavior might be due to the slow relaxation of local stresses stored during the preshear. In other terms, such levels of applied stresses might not be sufficient to overcome the effects of the prior stress history experienced by the sample. For intermediate stresses ($1.5Pa \leq \sigma_m \leq 6Pa$), these delayed effects of the preshear mentioned above disappear. Instead, the slow increase of the strain following the start-up lasts until a transition from a 'solid-like' to a 'fluid-like' behavior occurs. Such a slow strain evolution is the hallmark of the aging phenomena. Depending on the level of stress experienced by the sample , the aging process can last from

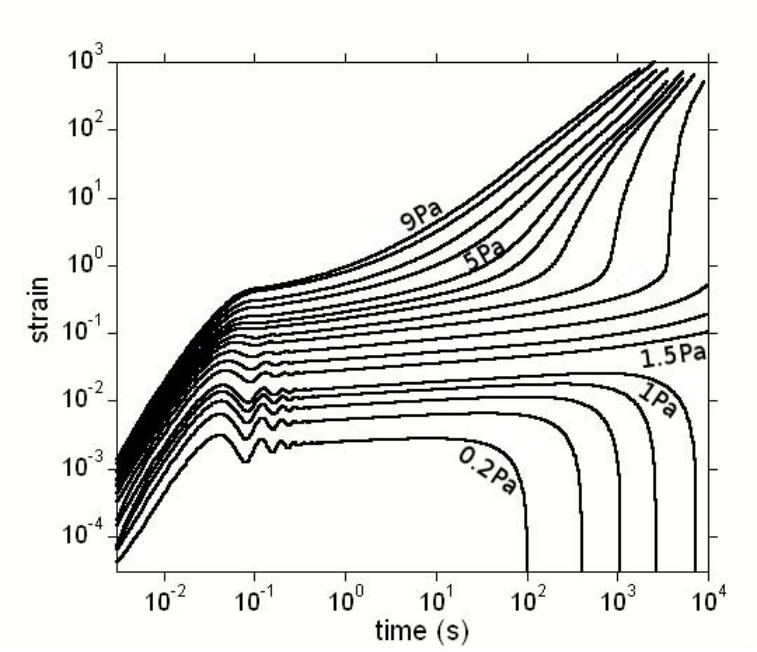

Figure 7.10: Strain as a function of time for different measurement stress, σ_m = 0.2, 0.4, 0.6, 0.8, 1, 1.5, 2, 2.5, 3, 3.5, 4, 4.5, 5, 6, 7, 8 and $9Pa$ from bottom to top respectively.

few dozen of seconds to hours for σ_m = $6Pa$ and σ_m = $1.5Pa$ respectively. At last, for higher considered stresses ($\sigma_m \geq 6Pa$), the curves shown in Fig.7.10 show that the time necessary for the sample to reach its fluid-like regime is reduced to seconds.

As in above sections the start-up of each measurement steps shown in Fig.7.10 is governed by the inertial coupling between the studied sample and the moving part of the rheometer. The magnitude and frequency of the resulting free damped oscillations of the strain are found to depend on the magnitude of the applied stress step. Using the same Maxwell-Jeffrey model as described above, the first $150ms$ of each curves can be fitted as shown for σ_m = 0.2, 1.5, 5 and $9Pa$ in the inset of Fig.7.11(a). The resulting values of G, η_1 and η_2 (the three Maxwell-Jeffrey model parameters) are shown in Fig.7.11(a), Fig.7.11(b) and Fig.7.11(c) respectively.

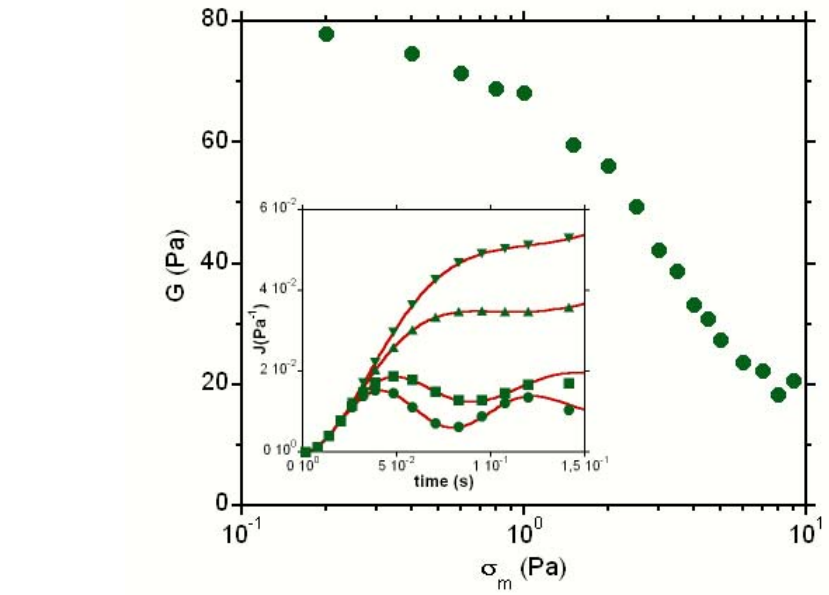

(a)

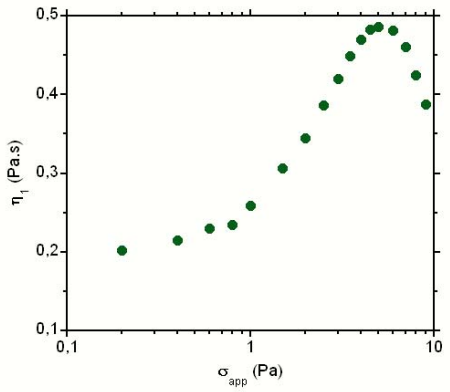

(b)

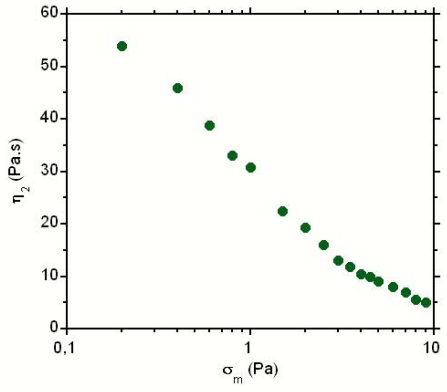

(c)

Figure 7.11: Fitted values of G (Fig.7.11(a)), η_1 (Fig.7.11(b)) and η_2 (Fig.7.11(c)) as a function of σ_m. In the inset in Fig.7.11(a), the plain lines corresponds to the Maxwell-Jeffrey model *eq.*7.1 fitted to the experimental data for σ_m = 0.2, 1.5,5 and $9Pa$ from bottom to top respectively.

7.6 Discussion

Unlike other materials as those studied by Coussot and co-workers and Derec *et al.* [8, 32], G is found to decrease with T_w (see Fig.7.9). Nonetheless, this decreasing is expected since a rough observation indicates that the sample seems more 'solid' after than before the preshear. Besides, comparing TEM micrographs of cryofractures obtained on a recently sheared sample (see Fig.7.12a) and another one left to recover for several hours after an identical shear history (see Fig.7.12d) provides with a plausible explanation concerning the elasticity decrease shown in Fig.7.9. Indeed as shown in Fig.7.12a, closely packed domains are formed under shear. Their interfaces form a dense network enlightened in grey in Fig.7.12b. While left at rest, these closely packed domains might coalesce to form larger domains as shown in Fig.7.12c with the result that the network separating them might become less rigid. This possible evolution of the sample internal structure during recovery is supported by the TEM micrograph of a cryofracture obtained on a sample left at rest for several hours (see Fig.7.12d) which shows larger and less packed domains.

Another specificity of the investigated material when compared to other soft jammed systems [8], is that the elasticity G is found to decrease from $G \approx 80Pa$ to $G \approx 20Pa$ with increasing stresses. It can be noticed here that a curvature reversal occurs for $\sigma_m \approx 3Pa$. As shown in Fig.7.10, this latter value corresponds to the one necessary to induce a transition from 'solid-like' to 'fluid-like' behavior in the studied material. As for G, the polymeric viscosity η_1 is found to evolve with σ_m. After a smooth increase, η_1 reaches a maximum for $\sigma_m \approx 5Pa$. Here again, the applied stress for which the curvature reverses itself is found to correspond to the transition from 'solid-like' to 'fluid-like' behavior at long time. Finally, the third fitted parameter, η_2, is found to continuously decrease with increasing σ_m. However a clear break in the slope of the curves occurs for the same apparently critical applied stress: $\sigma_m \approx 3Pa$. These later results, if confirmed in term of

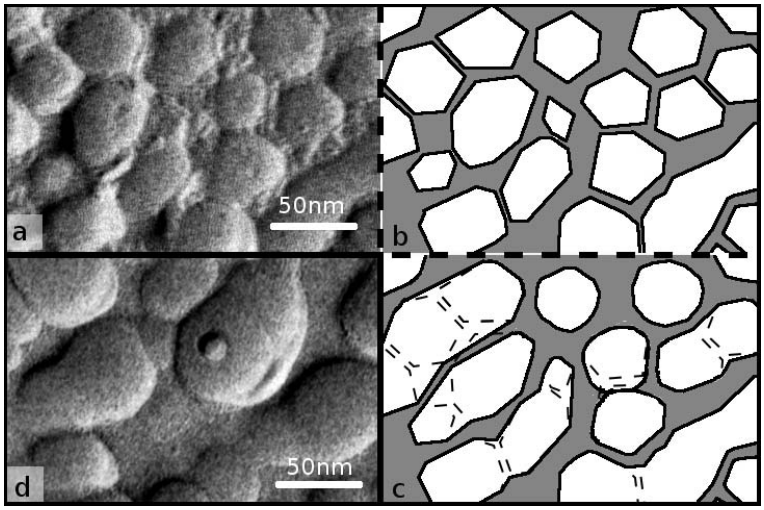

Figure 7.12: (a) cryofracture TEM micrograph of a recently sheared sample, (b) sketch enlightning the dense network formed by the domains displayed in (a), (c) sketch showing the possible coalescence of the domains shown in (c) (dashed lines), (d) cryofracture TEM micrograph of a sample left at rest for several hours after shearing.

structural evolution of the sample, might indicate that a careful analysis of the free damped oscillations resulting from inertial coupling in creep flow measurements might allow to predict aging and yielding in such materials.

The physical interpretation of aging, shown on Fig.7.10, in such a structured material (*ie.* stacked interconnected bilayers) is rather complex. Nonetheless, considering the freeze fracture micrographs of Fig.7.12 obtained during the relaxation of the sample, one might interpret the above results in term of stress induced structural rearrangement. Indeed, multilamellar vesicles [25] are formed during the preshear with a given defects density. Whereas higher values of stresses might bring a sufficient amount of energy to overcome the effects of these defects so that the material rapidly evolves towards a fluid-like regime, lower amount of energy would not. Instead these defects would disappear through a slow diffusion process of which the macroscopic consequence would be aging.

7.7 Conclusion

The different results shown in this work indicate that a given AOT/Iso-octane/water system has strong similarities with soft-jammed fluids [8, 9, 33]. However this phase made of interconnected bilayers is very different from others fluids. On a freshly loaded sample, the first macroscopic rheological response is strongly dependent on the capacity of the system to form lamellar vesicles under shear. Upon a sufficiently high shear stress, for example $\sigma = 10Pa$, lamellar membranes transform themselves into lamellar vesicles. These vesicles keep the same membrane thickness of $5.9nm$. The signature of this change is given in WAXS by the transformation from an anisotropic to an isotropic lamellar pattern without change of the correlation peaks positions. The vesicular shape is clearly identified after Freeze Fracture TEM micrographs showing quasi spherical objects of $50nm$. At a macroscopic scale, this structural transition comes along with a complex temporal evolution of the strain. The transition is achieved when the strain increase linearly with the time. The latter is ensured by the almost perfect superimposition of the different recovery curves following the preshear.

The application of a reproducible measurement procedure and the analysis of the inertio-elastic response allow us to follow the evolution of the elastic modulus G as a function of the preshear time T_{init}. For $T_{init} \geq 2700s$ the elastic modulus G saturates at a constant value. This corresponds to the shear induced formation of lamellar vesicles in an "out of equilibrium" thermodynamic steady state. When the shear stress is removed the strain-time recovery evolution decreases indefinitely. This recovery is strongly correlated to a decrease of the elastic modulus G and to the coalescence of closely packed lamellar vesicles.

It can be noticed that the increase of the lamellar vesicles size is in qualitative agreement with a decrease of the elastic modulus, G. As shown on other liquids by Liu and Courbin [21, 34], the structure changes are reversible at a macroscopic scale.

Starting from a steady state of reference, strain-time curves show three regimes depending on the applied stress. (i) At high imposed shear stress, a fluid-like liquid is obtained through a ternary creep. During this creep the shear induces lamellar vesicles domains. (ii) At intermediate shear stress, the strain-time curves show a solid to fluid transition. This transition is characterized by a secondary creep regime attained after a strain plateau. (iii) Finally, the strain-time curve shows a solid regime with a primary creep followed by a delayed viscoelastic effect.

The analysis of the time inertio-elastic oscillations at different shear stresses (i.e. energies densities) lead to trends different from other soft jammed liquids [8]. For the lamellar AOT, Iso-Octane and water system studied, the elastic modulus decreases with the shear stress. The decrease of the nanometric structures size is in good agreement with an increase of the density energy (i.e. σ).

Moreover, if we push further the analysis, it is possible to determine the limit between the solid-like and the liquid-like behaviour by looking at the changes of slope on the elastic modulus G and viscous modulus η_1 and η_2.

References

[1] H.A. Barnes. Thixotropy - a review. *Journal of Non-Newtonian Fluid Mechanic*, 70:1–33, 1997.

[2] H.A Barnes. The yiels stress - a review or " -everything flows? *Journal of Non-Newtonian Fluid Mechanic*, 81:133–178, 1999.

[3] G. Roberts and H.A Barnes. Nes measurements of the flow curves for carbopol dispersions without slip artefacts. *Rheologica Acta*, 40:499, 2001.

[4] G. Roberts, H.A Barnes, and P. Carew. Modeling the flow behaviour of very shear thinning liquids. *Chemical Engineering Science*, 56:5617, 2001.

[5] J.M. Piau. Carbopol gels: Elastoviscoplastic and slippery glasses made of individual swollen sponges meso- and macroscopic properties, constitutive equations and scaling laws. *Journal of Non-Newtonian Fluid Mechanic*, 144:1, 2007.

[6] F. Caton and C. Baravian. Plastic behavior of some yield stress fluids: from creep to long time yield. *Rheologica Acta*, 47:601–607, 2008.

[7] N.Y. Yao, R.J Larsen, and D.A. Weitz. Probing non linear rheology with inertio-elastic oscillations. *Journal of Rheology*, 52:1013, 2008.

[8] P. Coussot, H. Tabuteau, X. Chateau, L. Tocquer, and G. Ovarlez. Aging and solid or liquid behavior in pastes. *Journal of Rheology*, 50(6):975–994, 2006.

[9] T. Bauer, J. Oberdisse, and L. Ramos. Collective rearrangement at the onset of flow of a polycrystalline hexagonalcolumnar phase. *Physical Review Letters*, 97:258303(1) – 258303(4), 2006.

[10] P. Coussot, J.S. Raynaud, F. Bertrand, P. Moucheront, and J.P. Guilbaudand H.T. Huynh. Coexistence of liquid and solid phases in flowing soft-glassy materials. *Physical Review Letters*, 88(21), 2002.

[11] F. DaCruz, F. Chevoir, D. Bonn, and P. Coussot. Viscosity bifurcation in granular materials, foams, and emulsion. *Physical Review E*, 66(5), 2002.

[12] M. Cloitre, R. Borrega, and L. Leibler. Rheological aging and rejuvenation in microgel pastes. *Physical Review Letters*, 85(22):4819–4822, 2000.

[13] C. Baravian and D. Quemada. Using instrumental inertia in controlled stress rheometry. *Rheologica Acta*, 37:223–233, 1998.

[14] C. Baravian, G. Benbelkacem, and F. Caton. Unsteady rheometry: can we characterize weak gels with a controlled stress rheometer? *Rheologica Acta*, 46:577–581, 2007.

[15] N.W. Tamamushi and N. Watanabe. The formation of molecular aggregation structure in ternary system: Aerosol ot / water / iso-octane. *Colloid and Polymer Science*, 258:174–178, 1980.

[16] H. Kunieda and K Shinoda. Solution behavior of aerosol ot/water/oil system. *Journal of Colloid and Interface Science*, 70:577 –583, 1979.

[17] O. Diat, D. Roux, and F. Nallet. Effect of shear on a lyotropic lamellar phase. *Journal de Physique II France*, 3:1427–1452, 1993.

[18] O. Diat and D. Roux. Layering effect in a sheared lyotropic lamellar phase. *Physical review E*, 51:3296–3299, 1995.

[19] J. Bergenholtz and N.J. Wagner. Formation of aot/brine multilamellar vesicles. *Langmuir*, 12:3122–3126, 1996.

[20] L. Courbin, J.P. Delville, J. Rouch, and P. Panizza. Instability of a lamellar phase under shear flow: Formation of multilamellarvesicles. *Physical Review Letters*, 89(14):148305(1) – 148305(4), 2002.

[21] L. Courbin and P. Panizza. Shear-induced formation of vesicles in membrane phases: Kinetics and sizeselection mechanisms, elasticity versus surface tension. *Physical Review E*, 69(2):021504(1) – 021504(12), 2004.

[22] A.S. Wunenburger, A. Colin, T. Colin, and D. Roux. Undulation instability under shear: A model to explain the different orientations of a lamellar phase under shear. *The european physical journal E*, 2:277–283, 2000.

[23] A.G. Zilman and Granek R. Undulation instability of lamellar phases under shear: A mechanism for onion formation. *European Physical Journal B*, 11:593–608, 1999.

[24] S.W. Marlow and P.D. Olmsted. The effect of shear flow on the helfrich interaction in lyotropic lamellar systems. *The European Physical Journal E*, 8:485–497, 2002.

[25] P. Panizza, D. Roux, V. Vuillaume, C.Y.D Lu, and M.E. Cates. Viscoelasticity of the onion phase. *Langmuir*, 12:248–252, 1996.

[26] Y. Auffret, D.C. Roux, N. El Kissi, I Pignot-Paintrand, and D.E. Dunstan. aging and yielding in dense aot / iso-octane / water emulsion. *To be published*, 2008.

[27] U. Zölzer and H-F. Eicke. Free oscillatory shear measurements- an intersting applicationof constant tstress rheometers in the creep mode. *Rheologica Acta*, 32(1):105–107, 1993.

[28] R. Roscoe. Free damped oscillations in viscoelastic materials. *Britanical Journal of Applied Physics (J. Phys. D)*, 2(2):1261 – 1266, 1969.

[29] L.C.E Struik. Free damped vibrations of linear viscoelastic materials. *Rheologica acta*, 2(6):119–129, 1967.

[30] B.A. Coldren, H.E. Warriner, R. Van zanten, J.A. Zasadzinski, and E.B Sirota. Lamellar gels and spontaneous vesicles in catanionic surfactant mixtures. *Langmuir*, 22:2465–2473, 2006.

[31] P. Coussot, Q.D. Nguyen, H.T. Huynh, and D. Bonn. Viscosity bifurcation in thixotropic, yielding fluids. *Journal of Rheology*, 46(3):573–589, 2002.

[32] C. Derec, G. Ducouret, A.Adjari, and F. Lequeux. Aging and nonlinear rheology in suspensions of polyethylene oxyde-protectedsilica particles. *Physical Review E*, 67, 2003.

[33] L. Cipelletti, S. Manley, R.C. Ball, and D.A. Weitz. Universal aging features in the restructuring of fractal colloidal gels. *Physical review Letters*, 84(10):2275 – 2278, 2000.

[34] C-H. Liu and D.J. Pine. Shear-induced gelation and fracture in micellar solutions. *Physical Review Letters*, 77:2121–2124, 1996.

General Conclusion

In this piece of research we have investigated the shear induced formation of isotropic lamellar vesicles in initially anisotropic lamellar phases of interconnected and charged bilayers. These are formed by AOT, iso-octane and water on a relatively wide range of concentration. Unlike previously studied lamellar mesophases, in the concentration range considered in this study permanent topological defects remain permanently in the quiescent phases. This confers the studied samples with spontaneous structural organizations at various length scales ranging from nanoscopic to mesoscopic.

The self-assembling phenomena involved in such lyotropic systems and some relevant theoretical results have been described in the first part of this manuscript together with the different experimental techniques used in this piece of work, namely shear rheometry, flow birefringence texture analysis, wide angle x-ray scattering and freeze fracture electron microscopy. These techniques have allowed us to probe the structural transition process and its consequences at all involved length scales.

In a preliminary study, we have investigated the transient rheological behaviour of these systems in either strain or stress controlled rheometry.

The results discussed in the corresponding chapter show an unusual succession of behaviours upon application of constant shear rate or stress. Indeed, the apparent viscosity shows an overshoot, followed by a decrease and finally reaches a steady plateau after a rheopectic transition. Repeating the measurements for different level of shear rates or stresses, we have shown that the whole evolution

process of the sample viscous properties is controlled by the level of strain it experiences. we have then focused on the possible effects of the sample confinement on its apparent rheological properties. At last but not least these results have allowed us to define a range of stresses and shear rates for which steady states were actually reached.

The second part of our study have concerned the nanoscopic and microscopic structures of the investigated material and their evolution upon application of various level of shear rates.

In the corresponding chapter we have explicitly shown an anisotropic to isotropic structural transition at both nanoscopic and microscopic levels by means of wide angle x-ray scattering experiments and in flow birefringence texture analysis. Focusing first on the textures evolution we have shown that initially 'sheet-like' birefringent domains evolved toward 'grainy' domains corresponding to a new organization of the topological defects at the microscopic scale. The characteristic size of the grainy texture is shown to be controlled by the level of shear rates applied and in good agreement with Frank's theory. The transition from one type of textures to the other is shown to correspond in term of applied strain to the formation of lamellar vesicles at the nanoscopic scale. The latter is shown after wide angle x-ray scattering experiments and freeze fracture electron microscopy. Besides, our observations of the evolution of the birefringent patterns from a macroscopic point of view have explicitly shown that these two simultaneous transitions are at the origin of the rheopectic transition previously observed. At last concerning these structural transition phenomena, we show that the shear-induced mesophase, namely lamellar vesicles remains stable for significant length of time upon shear cessation.

The final part of our study aimed to characterize the rheological properties of the shear induced phases. This has been done after stress-controlled shear rheometry and freeze fracture transmission electron microscopy.

Our preliminary studies of the transient rheological regime as well as the

structural transition which are at stake in such structured and textured material have allowed us to define an *out-of-equilibrium steady state of reference* on which relied the measurement procedure followed to probe the time and shear history dependent viscoelastic properties of the shear-induced lamellar vesicle phases. In these controlled and reproducible conditions, We have shown that these mesophases behave as soft jammed system with aging and yielding properties. These properties can be predicted from an analysis of the inertial coupling phenomena at the start-up of creep measurements. Finally, the different parameters involved are identified and controlled so that the material structural and viscoelastic properties are almost perfectly controlled.

Conclusion Générale

Au cours de ce travail de recherche, nous avons étudié la formation de vésicules lamellaires isotropes induite par l'écoulement de phases lamellaires initiallement anisotropes formées par des bicouches interconnectées et chargées. Celles-ci sont formées par l'AOT, l'Iso-octane et l'Eau sur une plage relativement large de concentrations. A la différence d'autres phases lamellaires lyotropes, des défauts topologiques permanents se forment au repos sur une certaine gamme de concentrations. Ainsi, les échantillons considérés dans cette étude présentent une organisation spontanée à différentes échelles de longueur allant du nanomètre au millimètre.

Les propriétés auto-associatives des molécules tensioactives formant les systèmes lyotropes ainsi que certains résultats théoriques pertinents ont été décrites dans le premier chapitre de ce manuscript. Nous donnons ensuite une description complète des techniques expérimentales utilisées pour caractériser les propriétés rhéologiques et structurelles des différents systèmes étudiés dans le second et le troisième chapitre du manuscript. Ces techniques, diffusion de rayons X aux grands angles, analyse de textures de biréfringence, microscopie electronique en transmission de cryofractures et rhéométrie de cisaillement nous ont permis de caractériser la transition sous cisaillement subit par le matériau et ces conséquences à toutes les échelles impliquées.

Dans la première partie de notre étude, nous nous sommes intéréssés au régime d'écoulement transitoire de ces systèmes en rhéométrie à déformation puis à contrainte imposées.

Nos résultats montrent une succession inhabituelle de comportements suite à l'application d'un gradient ou d'une contrainte de cisaillement constant. En effet dans les deux cas, la viscosité de cisaillement montre un 'overshoot' suivit d'un minimum local puis d'une transition rheopectique avant d'atteindre une valeur plateau. Répétant cette mesure pour différents niveaux de gradients de cisaille-

ment ou de contraintes, nous avons montré que ce processus évolutif était contrôlé par le niveau de déformation subit par l'échantillon. Nous avons alors porté l'étude sur les effets possibles du confinement de l'échantillon sur ses propriétés rhéologiques apparentes. Finallement, ces résultats nous ont permis de définir une plage de gradients de cisaillement et de contraintes pour lesquels un état stable apparent pouvait être atteint.

La seconde partie de notre étude s'est focalisée sur la caractérisation des propriétés structurelles de ces sytèmes aux échelles nanoscopiques et microscopiques et l'évolution de ces propriétés sous l'application de différents gradients de cisaillement.

Dans le chapitre correspondant nous avons explicitement montré une transition structurelle de type anistrope / isotrope aux échelles nano- et microscopique à l'aide de techniques de diffusion de rayon X aux grands angles sous écoulement et d'une analyse de textures en lumière polarisée sous écoulement. En nous concentrant dans un premier temps sur l'évolution des textures, nous avons montré une transition de textures de type 'bandes' à des textures de type 'grains'. La taille caractéristique de ces grains est controlée par le gradient de cisaillement appliqué et est en bon accord avec la théorie de Frank. Nous montrons également que la transition d'un type de texture à l'autre correspont en terme de déformation appliquée à l'échantillon à la formation de vésicules lamellaires à l'échelle nanoscopique. Celle-ci est montré à l'aide de deux techniques complémentaires: la diffusion de rayons X aux grands angles sous cisaillement et la microscopie electronique en-transmission de cryofractures. En outre, nos observations des textures en lumière polarisée circulairement et à l'échelle macroscopique nous ont permis de montrer explicitement que ces deux transitions simultanées aux échelles nanoscopiques et microscopiques sont à l'origine de la transition rhéopectique étudiée précedemment. Enfin, Nous avons montré que la phase vesiculaire induite sous cisaillement reste stable sur des périodes de temps significatives une fois que l'écoulement cesse.

Dans la dernière partie de notre étude nous nous intéressons à la car-

actérisation des propriétés rhéologiques de la phase vésiculaire induite sous cisaillement. Pour ce faire nous établissons une procédure expérimentale basée sur des mesures successives de fluage.

Nos études du régime d'écoulement transitoire et de la transition de structure induite sous cisaillement nous ont permis de définir un état stable de référence hors-équilibre thermodynamique. L'obtention de ce dernier permet l'étude des propriétés viscoélastique de la phases vésiculaire induite sous cisaillement bien que celles-ci dépendent fortement du temps et de l'histoire de l'échantillon étudié. Dans ces conditions controlées et reproductibles, nous avons montré que ces mesophases ont des propriétés d'écoulement complexes. Ceux sont en effet des matériaux à seuil d'écoulement présentant du vieillissement. Notre analyse des oscillations inertio-elastiques résultant d'un saut de contrainte appliquée nous a alors permis d'identifier les différents paramètres contrôlant ce comportement complexe et de caractériser quantitativement les propriétés viscoélastiques de ces matériaux en fonction de leur histoire.